

Spectral analysis of polymer elongation processes

Citation for published version (APA):

Zavinska, O. (2009). *Spectral analysis of polymer elongation processes*. [Phd Thesis 1 (Research TU/e / Graduation TU/e), Mechanical Engineering]. Technische Universiteit Eindhoven.
<https://doi.org/10.6100/IR640008>

DOI:

[10.6100/IR640008](https://doi.org/10.6100/IR640008)

Document status and date:

Published: 01/01/2009

Document Version:

Publisher's PDF, also known as Version of Record (includes final page, issue and volume numbers)

Please check the document version of this publication:

- A submitted manuscript is the version of the article upon submission and before peer-review. There can be important differences between the submitted version and the official published version of record. People interested in the research are advised to contact the author for the final version of the publication, or visit the DOI to the publisher's website.
- The final author version and the galley proof are versions of the publication after peer review.
- The final published version features the final layout of the paper including the volume, issue and page numbers.

[Link to publication](#)

General rights

Copyright and moral rights for the publications made accessible in the public portal are retained by the authors and/or other copyright owners and it is a condition of accessing publications that users recognise and abide by the legal requirements associated with these rights.

- Users may download and print one copy of any publication from the public portal for the purpose of private study or research.
- You may not further distribute the material or use it for any profit-making activity or commercial gain
- You may freely distribute the URL identifying the publication in the public portal.

If the publication is distributed under the terms of Article 25fa of the Dutch Copyright Act, indicated by the "Taverne" license above, please follow below link for the End User Agreement:

www.tue.nl/taverne

Take down policy

If you believe that this document breaches copyright please contact us at:

openaccess@tue.nl

providing details and we will investigate your claim.

**Spectral Analysis
of
Polymer Elongation Processes**

Spectral Analysis of Polymer Elongation Processes / by Olena Zavinska
Technische Universiteit Eindhoven, 2008

A catalogue record is available from the Eindhoven University of Technology Library
ISBN: 978-90-386-1505-9
NUR 919

Keywords: polymer elongation process, spectral analysis, draw resonance, mathematical modeling, stability analysis, traveling wave, model parameter estimation, fiber spinning, film casting

Reproduction: University Press Facilities, Eindhoven, The Netherlands

This research was carried out in close cooperation with and funded by Dow Benelux B.V., Terneuzen, The Netherlands

Spectral Analysis of Polymer Elongation Processes

PROEFSCHRIFT

ter verkrijging van de graad van doctor aan de
Technische Universiteit Eindhoven, op gezag van de
Rector Magnificus, prof.dr.ir. C.J. van Duijn, voor een
commissie aangewezen door het College voor
Promoties in het openbaar te verdedigen
op maandag 12 januari 2009 om 16.00 uur

door

Olena Zavinska

geboren te Chernihiv, Oekraïne

Dit proefschrift is goedgekeurd door de promotoren:

prof.dr.ir. H.E.H. Meijer

en

prof.dr. R.J. Koopmans

Copromotor:

dr.ir. S.J.L. van Eijndhoven

To my brother

Summary

Mathematical models are developed and applied to simulate polymer elongation processes, like film casting and fiber spinning, thus replacing expensive experiments. The goal of the simulations is to find the optimal processing conditions that guarantee efficient production and high quality products. In these models, the polymer's behavior is captured in constitutive relations that involve parameters that are partly related to the visco-elastic nature of polymer fluids and partly to their molecular structure. It is generally difficult to obtain the material parameters needed in these models and only a few experiments are available in practice.

In this thesis a novel procedure is proposed to estimate the parameters in the constitutive models in a fast and accurate way. The procedure is based on controlled filament elongation of the polymer melt using a Rheotens set-up, which is a device that resembles a small scale fiber spinning process. Moreover is the focus of the thesis on process limits as represented by stability issues. It proves that both issues can be combined. In the Rheotens experiment we start to determine the eigenfrequencies of the force that the drawing wheels apply on the filament from experimental data. They are subsequently used to match the eigenfrequencies as they result from the numerical simulations, in dependence of the value of the material parameters. The procedure requires an efficient numerical routine to calculate the true spectrum of a first order system of differential operators endowed with two point boundary conditions. Application of the parameter estimation procedure developed yields an adequate identification of the values of the parameters in the constitutive equations that determine a polymer material and enables end-users to enhance quality - and improve process control. In this context, as an application, draw resonance in the film casting process is considered in this thesis. A non-isothermal model is used to describe this process.

The main contribution of this thesis is the design of the parameter estimation procedure. For that, dedicated numerical routines and associated software were necessary. In particular, we focused on the calculation of eigenfrequencies that demands a (numerical) solution of the steady state of non-linear systems of first order partial differential equations endowed with inhomogeneous boundary conditions and on the computation of the spectrum of the corresponding linearized system. Both computational steps are designed as generic as possible; they can be used for a wide class of problems involving similar stability issues.

The main conclusion is that the procedure developed works accurately and fast, indeed, and can

be used on an operational level. The parameter estimation procedure is demonstrated to work for a number of resins. With respect to the prediction of draw resonance in the film casting process, the tests with the modified Giesekus model for a linear low density polyethylene show a perfect match between experiments and simulations.

Contents

1	General Introduction	1
2	Mathematical Framework	5
2.1	Introduction	5
2.2	Discussion on Stability	7
2.2.1	Auxiliary Statements	7
2.2.2	General Issues	10
2.3	Implementation	14
2.3.1	Stationary Problem	14
2.3.2	Linearized Problem	15
2.4	Illustration and Validation	19
2.4.1	Generalized Wave Equation	19
2.4.2	Fiber Spinning: Simple Model	22
2.5	Conclusions	25
A1	Formal Expression for Spectrum	26
3	Rheotens	29
3.1	Introduction	29
3.1.1	Background	29
3.1.2	Literature Review	30
3.1.3	Objective	31
3.2	Rheotens Experiment	31
3.2.1	Description	31
3.2.2	Materials	36
3.2.3	Influence of Operating Conditions	38
3.2.4	Difference in Materials	44
3.2.5	Influence of the Drawing Length	49
3.2.6	Conclusions from Experiments	52
3.3	Mathematical Modeling	53
3.3.1	Configuration and Assumptions	53
3.3.2	Equations	54

3.3.3	Boundary Conditions	58
3.3.4	Scaling	59
3.3.5	Dimensionless Systems	60
3.3.6	General Formulation	62
3.4	Simulations: Newtonian Model	63
3.4.1	Remarks about Viscosity	63
3.4.2	Influence of Extrudate Swell	64
3.5	Simulations: the Modified Giesekus Model	66
3.5.1	Sensitivity Analysis	68
3.5.2	Parameter Estimation	74
B1	Viscosity Data for LDPE at 150 ⁰ C	79
4	Film Casting	81
4.1	Introduction	81
4.1.1	Description of the Process	81
4.1.2	Literature Review	82
4.1.3	Objective	82
4.2	Modeling	83
4.2.1	Configuration	83
4.2.2	Assumptions	84
4.2.3	The Model Equations	84
4.2.4	Boundary Conditions	89
4.2.5	Scaling	89
4.2.6	Dimensionless System	90
4.2.7	General Formulation	92
4.3	Stability Recognition	93
4.3.1	Model Parameters	93
4.3.2	Numerical Precision	94
4.3.3	Spectrum	95
4.3.4	Stability Solution: Isothermal	98
4.3.5	Stability Solution: Non-isothermal	101
4.3.6	Comparison with the Experimental Data	107
4.4	Conclusions	110
C1	Temperature Analysis	110
C1.1	Coefficients Analysis	111
C1.2	Conclusion	113
C2	An example of the modified Giesekus constitutive model parameters for LDPE material	114
5	Conclusions	115

General Introduction

Film casting, extrusion coating, film blowing and fiber spinning are examples of industrial processes in which extruded polymer material in a viscoelastic state is elongated. Generally this elongation is characterized by the draw ratio and the higher the draw ratio the more elongation is achieved in the process. Most processes require a high draw ratio to generate efficient production. But, at the critical draw ratio, the process is no longer stable and unwanted wavy-like phenomena appear. These phenomena are commonly referred to as draw resonance. In the presence of draw resonance, end products do not satisfy specifications, quality suffers, or even the complete process breaks down and has to be reset, all at the cost of time and money. Therefore, the critical draw ratio at which the system shows resonance behavior is an important characteristic of a polymer elongation process.

Need for Simulation Tools

For decades, the polymer industry has been involved in the development of tools by which the onset of draw resonance and the critical draw ratio can be predicted, given the type of polymer and the type of process. A way to do this is by means of carrying out experiments based on an intelligent design where process conditions and polymer material are the variable factors and drawing force is the predictor. Then the associated statistical analysis may lead to a desired prediction on the best polymer material and the best operating conditions to be used. The complexity of the statistical design due to the many factors to be included make a statical approach less applicable. The alternative is a software tool based on a mathematical model that is assumed to describe the typical features of both the process and the polymer material. Simulation of the process using such a tool should primarily predict the onset of draw resonance in the process but may also reveal other features of the process such as elongation forces and velocity distributions.

What are the Material Parameters?

Mathematical models combine the laws of physics obeyed by the process, e.g. balance of mass, momentum, or energy, and the rheological behavior of the polymer material captured in constitutive relations. The models contain parameters: process parameters and material parameters. The process parameters describe the process conditions and may be assumed known. The material parameters describe the kind of polymer material used, partly based on an assumed molecular constitution, partly on an assumed rheological behavior, and are reflected in the constitutive relations. As yet, the polymer industry does not constitute the polymers based on values of material parameters in a constitutive model. Of course, there are standard experiments carried out in industrial laboratories in which polymers are classified according to their temperature dependent shear viscosity and relaxation spectrum. But as constitutive models were designed for qualitative rather than quantitative purposes, given a polymer, the majority of the parameters in the constitutive models are undetermined and merely well- or badly guessed.

A Parameter Estimation Procedure

In this thesis, we describe a procedure that we designed such that for a given constitutive model the material parameters related to a type of polymer can be determined. We prove applicability of our procedure for a variety of different polymers, such as Linear Low Density Poly-Ethylene, Low Density Poly-Ethylene, Poly-Propylene, and Poly-Styrene, using a modified Giesekus model as the constitutive model. The procedure is based on a well-known experiment, namely, the Rheotens test. The novel idea is that we perform the Rheotens experiment not only in its acceleration mode but also in the constant mode with well specified drawing velocities. We prove that if data from this experiment are matched with data from a dedicated mathematical model, a unique classification of the polymer in terms of the parameters in the constitutive model is obtained. Matching data is achieved by a parameter estimation method based on an optimization routine. Thus, we establish a method, by which the polymer producing industry is enabled to characterize the material parameters of a polymer, and reset these parameters every time a new batch is produced. Our procedure can, therefore, also be used for quality control during production.

Application on an Operational Level

In a polymer application environment, for instance in the environment where typical polymer elongation processes are used, we propose to apply our parameter estimation method every time a new batch of the polymer material arrives, and then to use the estimated parameters in a mathematical model that describes the elongation process in order to establish the best operating conditions of the process. As an example of such an application, we consider in this thesis film casting, where we assume that the process satisfies non-isothermal conditions.

Mathematical Issues

Both the mathematical model that describes the Rheotens experiment and those models that describe other polymer elongation processes consist of a number of first order nonlinear partial differential equations that constitute a hyperbolic system with space and time as independent variables. The system of differential equations is supplemented with nonhomogeneous boundary conditions. Such systems allow for a steady state stability analysis. The steady state describes the stationary mode of the process; stability analysis describes oscillations on top of the stationary mode. If these oscillations are damped, the process is stable. To determine from the model whether the oscillations are damped, usually a linear stability analysis is carried out. The nonlinear system is linearized about the steady state and a spectral analysis is applied to the resulting linear system. This analysis reveals the discrete spectrum of eigenfrequencies together with the corresponding damping factors and, also, the related eigenmodes. In a hyperbolic system these eigenmodes determine traveling waves that move along the elongated material with a specific velocity. In our parameter estimation procedure we make use of the steady state characteristics and the eigenfrequency characteristics, where we operate the Rheotens at a draw velocity for which resonance effects are clearly apparent. If a velocity of the traveling wave is measured (for instance by the Doppler velocimeter), this velocity can also be applied in the parameter estimation procedure.

The Simulation Tool

In order to have an operational software tool to estimate material parameters by searching for the optimal match between simulation and experiment, a fast numerical routine to carry out the spectral analysis is required. For that, dedicated numerical methods have been developed that determine the steady state of the hyperbolic system of nonlinear differential equations, and the main eigenfrequencies and eigenmodes of the related linearized system accurately and fast. This thesis describes and validates both methods, where the first one is based on a fourth order Runge-Kutta scheme in combination with a shooting algorithm, and the second one on a Galerkin kind of approach using local basis functions and a novel way to incorporate the homogeneous boundary conditions. In contrast to other methods to determine eigenfrequencies of this type of hyperbolic systems, the numerically calculated spectrum does not show spurious modes. Moreover, the calculation time of the complete spectrum on an ordinary PC with one processor and 256 Mb of operational memory takes only a few seconds. From each eigenmode we determine the amplitude and the phase. The phase, combined with the corresponding eigenfrequency, determines the wave velocity of the oscillation, fixed by the eigenmode and eigenfrequency. In polymer elongation processes, the phase is decreasing, which means that the waves travel from the die exit towards the point of take up. This results from the simulations are (of course) affirmed by experiments.

Structure of the Thesis

This thesis is divided into three chapters. In Chapter two, we present the mathematical frame underlying the mathematical models of the elongation processes. Tools from numerical mathematics

and mathematical theory are the essential ingredients to tackle the problem of draw resonance. Thus, we focus on the mathematics and at least suggest the hidden complications involved in the kind of mathematical analyses we carry out. The steady state follows from a first order inhomogeneous boundary value problem; mathematics would demand a proof of unicity and existence of the steady state solution. The stability of the steady state is determined by the spectrum of a first order differential operator. This operator is approximated by a finite rank operator, a matrix, and the spectrum by the eigenvalues of the matrix, a finite set of points. In Chapter two we validate our approach on basis of a benchmark problem that has the same aspects as the mathematical models representing the elongation processes.

In Chapter three, we describe the suggested measurement design to estimate parameters in a constitutive model. We regard this design as the main part of this thesis. It is a novel contribution to the complex field of parameters estimation in constitutive models. In our design we use the Rheotens device that we operate at fixed velocities of the drawing wheels specified such that at these velocities draw resonance is induced in the drawn polymer filament. The recorded time series of the force applied to the filament is analyzed for its characteristic frequencies by means of the Discrete Fourier Transform. In Chapter three we propose a mathematical model of this experimental process, from which we determine the eigenfrequencies, given the material parameters. We carry out a sensitivity analysis and demonstrate the dependence of eigenfrequencies on model parameters.

In Chapter four, we study the process of film casting, an important polymer extension operation that produces films. Knowledge of the dynamics and stability of this process enhances the productivity and the uniformity of the film produced. We model the process non-isothermally, but temperature is assumed to be quasi-static and not contained in the stability considerations, i.e., temperature oscillations are disregarded. We study film casting assuming several types of constitutive models such as the upper convected Maxwell (UCM), the Phan-Thien and Tanner (PTT), and the modified Giesekus model. In literature, results of draw resonance investigations are presented only for isothermal models. Validation of our results with respect to those available from the literature show perfect agreement. As also observed experimentally, the model shows that the influence on the stability of the process of a nonuniform temperature, due to cooling along the stretching part between the flat die and the chill roll, is significant. We validate the model using available experimental data taken from a laboratory set up where an LLDPE resin was casted. The validation proved that our non-isothermal model, with modified Giesekus constitutive relations, give a very accurate prediction of the draw resonance, while the material parameters are estimated by the procedure described in Chapter three.

Mathematical Framework

2.1 Introduction

In this chapter, we present in a condensed way the mathematical framework on which we base the further discussion of the stability of polymer elongation processes, in particular fiber spinning and film casting. In these processes, after having been extruded through a circular die or a flat die, the polymer fluid experiences elongation over a certain distance due to the pulling motion of a take-up device (wheels in fiber spinning, rolls in film casting.) At some draw rates, fluctuations in the dimensions of the polymer filament or polymer film are observed. This unwanted instability occurring in such polymer elongation processes is called draw resonance. Since the first observation of this phenomenon in 1962 by *Christensen* [1] and *Miller* [2], the issue of draw resonance has been frequently addressed in literature and mathematical models to describe the instability have been developed. To start we mention *Petrie and Denn* [3], *Ishihara and Kase* [4], *Denn* [5], who presented a large amount of experimental results on draw resonance. *Kase et al.* [6], *Pearson and Matovich* [7] were the first to perform a linear stability analysis describing draw resonance for a Newtonian fluid. They were followed by *Fisher and Denn* [8], *Ishihara and Kase* [9] with the first non-linear analysis, also for the Newtonian fluids, and *Fisher and Denn* [10] with the first stability analysis for a viscoelastic fluid. Investigations of draw resonance phenomena in elongational processes, for Newtonian as well as viscoelastic fluids, were pursued further by *Hyun* [11; 12], *Kase and Araki* [13], *Beris and Liu* [14; 15], *Bechel et al.* [16], *Kim et al.* [17], *Jung and Hyun* [79], *Doufas et al.* [19–21], to mention just a few. *Hagen and Renardy* [22–24] are considering the problem of draw resonance from a more global mathematical prospective, involving serious theory. A good description of the dynamics of film and fiber formation can be found in the book of *Agassant et al.* [25]. Finally, there is a complete discussion of the mechanics of fiber spinning process in the most recent book of *Denn* [26]. Most of the references mentioned are related to fiber spinning. A more comprehensive review on draw resonance investigations in film casting is presented in Chapter 4 of this thesis.

Most developed models describing film or fiber formation, from a generic mathematical prospective, satisfy the basis formulation given by a quasi linear system of partial differential equations, which are first order in time and place,

$$\mathcal{C}(\mathbf{y}; \mathbf{p}) \frac{\partial \mathbf{y}}{\partial t} = \mathcal{A}(\mathbf{y}; \mathbf{p}) \frac{\partial \mathbf{y}}{\partial x} + \mathbf{b}(\mathbf{y}; \mathbf{p}), \quad 0 < x < 1, \quad t > 0. \quad (2.1)$$

Here x and t are the independent variables, where x represents the normalized length and t - the normalized time; $\mathbf{p} \in \mathbb{R}^m$ is an array containing the process and material parameters, which guide the elongation process. The state $\mathbf{y} = \mathbf{y}(x, t; \mathbf{p})$ is an n -dimensional vector representing the physical quantities involved in the process such as velocity, radius, and stress. The symbols \mathcal{A} and \mathcal{C} denote $n \times n$ real valued matrix functions, and the symbol \mathbf{b} denotes a real valued vector function; they all depend on the state \mathbf{y} and the parameters \mathbf{p} . The matrix \mathcal{A} is invertible, matrix \mathcal{C} is not necessarily invertible. To the equation we add two-point boundary conditions, at $x = 0$ and at $x = 1$, which can be written as

$$\mathcal{P}[\mathbf{y}(0, t; \mathbf{p})] = \xi, \quad \mathcal{Q}[\mathbf{y}(1, t; \mathbf{p})] = \zeta, \quad (2.2)$$

where \mathcal{P} and \mathcal{Q} are projection operators from \mathbb{R}^n to suitable subspaces. To complete the description we should also include an initial condition in order to have a unique solution. In practice, an initial condition is not always evident to choose, however, we can always assume we have one,

$$\mathbf{y}(x, 0; \mathbf{p}) = \mathbf{y}^0(x, \mathbf{p}). \quad (2.3)$$

Generally, systems of the form (2.1) might be hyperbolic or elliptic, depending on the properties of the matrices $\mathcal{A}(\mathbf{y})$ and $\mathcal{C}(\mathbf{y})$, see *Courant and Hilbert* [27], *Taylor* [28]. More specifically, the nature of the system is determined by the characteristic determinant Λ of the system defined as $\Lambda = \det(\mathcal{A} + \tau \mathcal{C})$. If the equation $\Lambda = 0$ does not have real roots τ , then the system is called elliptic. If the equation $\Lambda = 0$ has n real different roots τ , then the system is called totally hyperbolic. A more general definition of hyperbolicity does not exclude multiplicity of the roots of the specified equation. In this work, we consider system (2.1) to be hyperbolic. We consider the problem described by (2.1)-(2.3) strictly in the context of the practical applications, namely, as a general description of the polymer elongation processes such as fiber spinning or film casting. The particular systems describing the processes mentioned are hyperbolic, we refer to *Beris and Liu* [14], *Forest and Wang* [29], *Betchel et al.* [30].

Some work on the existence and uniqueness of the solution of such or similar problems can be found in the literature. In particular, the work of *Hagen* [31] is worth mentioning, where existence, uniqueness, and regularity of solutions for the equations of fiber spinning of viscous (Newtonian) fluids are proven using the semigroup theory in a Hilbert space context. With respect to the existence and uniqueness of the solution of the fiber spinning equations for more complicated viscoelastic flow regimes, such as given by upper convective Maxwell, Phan-Thien and Tanner, and Giesekus constitutive models, an outline of a prove is also presented in [31]. In this chapter, discussing the mathematical framework underlying the mathematical models, we do not go to the very detail of the uniqueness and existence of the solution of the hyperbolic systems under consideration. We take a pragmatic approach and assume, where necessary, that existence and uniqueness of the solution are satisfied, even if we did not check that.

From a practical point of view, several questions are of interest:

- What is the form of the steady state for different values of the model parameters?
- Which process and material parameters guarantee stability of the steady state?
- Which of the process/model parameters is leading the bifurcation?

To answer these questions, however, we cannot rely on an analysis without doing some numerics. Thus, we have to be sure on the efficiency and robustness of the numerical technique adopted for the calculations. In order to guarantee a fast and robust implementation for eventually doing the numerical analyses, we consider a model described in a generic form and we come to an approach that is based on mathematics and not on the physics of the equations. Having said that, we present the discussion on the general mathematics related to the problem of stability in the elongational processes is presented in Section 2.2. Next, in Section 2.3 we give a generic numerical scheme that can be easily adopted for any particularly considered problem. We conclude this chapter with the validation of the numerical implementation developed, see Section 2.4.

In Chapter 3 we apply the mathematical model and related numerical scheme as discussed in this chapter to the Rheotens experiment. This experiment basically is a small scale fiber spinning process; it allows for observations of draw resonance. By applying the mathematical-numerical technique developed, we are able to make use of draw resonance characteristics, measured in an experiment, for the estimation of the parameters in the constitutive model. In Chapter 4 we address the problem of draw resonance in the process of film casting.

2.2 Discussion on Stability

2.2.1 Auxiliary Statements

Let V be a finite dimensional vector space, with dimension $\dim V = n$. Then V is a Banach space for any vector norm, $|\cdot|_V$. Its dual consists of all linear functionals on V and is denoted by V^* . For a subset $W \subset V^*$, we denote by W^0 the set of all elements of V that are annihilated by the elements of W , i.e.,

$$\mathbf{v} \in W^0 \Leftrightarrow \forall w \in W \quad \langle w, \mathbf{v} \rangle = 0. \quad (2.4)$$

By $C([0, 1], V)$, we denote the vector space of all continuous vector functions \mathbf{y} on $[0, 1]$ with values in V . Also the space $C([0, 1], V)$ is a Banach space when endowed with the uniform norm

$$\|\mathbf{y}\|_{C([0,1],V)} = \sup_{x \in [0,1]} |\mathbf{y}(x)|_V \quad (2.5)$$

For each $\mathbf{f} \in C([0, 1], V)$, we consider the following linear non-homogeneous system of first order differential equations

$$\frac{d\mathbf{y}}{dx} + \mathcal{H}(x)\mathbf{y} = \mathbf{f}, \quad x \in (0, 1), \quad (2.6)$$

together with the two-point boundary conditions

$$\langle p_i, \mathbf{y}(0) \rangle = \mathbf{0}, \quad i = \overline{1, n-k}; \quad (2.7)$$

$$\langle q_j, \mathbf{y}(1) \rangle = \mathbf{0}, \quad j = \overline{1, k}. \quad (2.8)$$

Here the sets $\{p_i\}_{i=1}^{n-k}$ and $\{q_j\}_{j=1}^k$ consist of linear functionals on V , and thus they are subsets of V^* . In the terminology introduced above, the boundary conditions can also be written as

$$\mathbf{y}(0) \in \{p_i\}^0, \quad i = \overline{1, n-k}; \quad (2.9)$$

$$\mathbf{y}(1) \in \{q_j\}^0, \quad j = \overline{1, k}. \quad (2.10)$$

Existence and uniqueness of the solution of the boundary value problem (2.6)-(2.8) is an essential condition for the stability of the steady state of hyperbolic systems. Stability issues are considered further in the next section; here we discuss the conditions that guarantee the existence and uniqueness of the solution for the problem formulated above. We understand the solution in a classical sense,

\mathbf{y} is a classical solution of (2.6)-(2.8) if \mathbf{y} is continuously differentiable function on the open interval $(0, 1)$ that satisfies (2.6) point-wise, and also the conditions (2.7)-(2.8).

Let $P(x)$ be the fundamental solution of the evolution equation

$$\frac{d\mathbf{y}}{dx} + \mathcal{H}(x)\mathbf{y} = \mathbf{0}, \quad z > 0, \quad (2.11)$$

that by definition satisfies the following relations: $P(0) = I$ and $\frac{dP}{dx} = -\mathcal{H}(x)P$. The fundamental solution can be obtained from Picard iterations resulting into an iterative sequence

$$P_0(x) = I, \quad (2.12)$$

$$\frac{dP_n}{dx} = -\mathcal{H}(x)P_{n-1}, \quad (2.13)$$

$$P(x) = \sum_{n=0}^{\infty} P_n(x). \quad (2.14)$$

The matrix function $P(x)$ is continuously invertible, where $x \mapsto P(x)^{-1}$ satisfies the evolution equation

$$\frac{dP^{-1}}{dx} = P^{-1}\mathcal{H}(x). \quad (2.15)$$

Statement 1. *Let P be the fundamental solution of (2.11). Then, for given functions \mathbf{f} and \mathcal{H} on $[0, 1]$, functionals $\{p_i\}_{i=1}^{n-k}$ and $\{q_j\}_{j=1}^k$ on V , such that $\mathbf{f} \in C([0, 1], V)$, $\mathcal{H}(x)$ is non-singular for all x , $\{p_i\}_{i=1}^{n-k}$ and $\{q_j\}_{j=1}^k$ are linear independent in V^* , and*

$$P(1)(\{p_i\}^0) \cap (\{q_j\}^0) = \{\mathbf{0}\}, \quad (2.16)$$

the two-point boundary value problem (2.6)-(2.8) has a unique solution in a classical sense.

Proof. We prove the statement by actually constructing the solution of (2.6)-(2.8). Formally, a solution of (2.6), in terms of the fundamental solution $P(x)$, for $x \in [0, 1]$ is unique and reads

$$\mathbf{y}(x) = P(x)\mathbf{y}(0) + \int_0^x P(x)P(\sigma)^{-1}\mathbf{f}(\sigma)d\sigma. \quad (2.17)$$

Function \mathbf{y} should satisfy $\langle p_i, \mathbf{y}(0) \rangle = 0, i = 1, \dots, n-k$. Since $\{p_i\}_{i=1}^{n-k}$ is independent in V^* , there is a linear independent collection $\{\mathbf{c}_1, \dots, \mathbf{c}_k\} \in V$ such that

$$\mathbf{y}(0) = \sum_{j=1}^k \phi_j \mathbf{c}_j. \quad (2.18)$$

In turn, the condition $\langle q_i, \mathbf{y}(1) \rangle = 0$ for $i = 1, \dots, k$ results in the algebraic equation

$$\Phi \boldsymbol{\phi} = \Psi \mathbf{f}, \quad (2.19)$$

where $\boldsymbol{\phi} = \{\phi_1, \dots, \phi_k\}$ is a vector consisting of the expansion coefficients ϕ_j ; Φ is the $(k \times k)$ -matrix defined by the elements

$$\Phi_{ij} \doteq \langle q_i, P(1)\mathbf{c}_j \rangle, \quad (2.20)$$

and Ψ is a bounded operator from the Banach space $C([0, 1], V)$ to \mathbb{R}^k defined by

$$\Psi \mathbf{f} \doteq - \langle q_i, \int_0^1 P(1)P(\sigma)^{-1}\mathbf{f}(\sigma)d\sigma \rangle. \quad (2.21)$$

Now the question on the existence and uniqueness of the classical solution of the system (2.6)-(2.8) comes down to invertibility of the matrix Φ . The matrix Φ is invertible because the condition (2.16) implies that the subspaces $(\{p_i\}^o)$ and $(\{q_j\}^o)$ are complementary, and thus the columns of Φ are independent. Hence, we explicitly constructed the solution that reads

$$\mathbf{y}(x) = \sum_{j=1}^k (\Phi^{-1}(\Psi)\mathbf{f})_j P(x)\mathbf{c}_j + \int_0^x P(x)P(\sigma)^{-1}\mathbf{f}(\sigma)d\sigma. \quad (2.22)$$

Uniqueness is a consequence of the way we constructed the solution, i.e. taking $\mathbf{y}(0)$ such that the boundary conditions are satisfied. \blacktriangle

Let us now consider a space \mathcal{W} that contains all functions in $C([0, 1], V)$ that satisfy the boundary conditions (2.7) and (2.8),

$$\mathcal{W} = \{\mathbf{v} \in C^1([0, 1], V) \mid \mathbf{v}(0) \in \{p_i\}^o, \mathbf{v}(1) \in \{q_j\}^o, i = \overline{1, k}; j = \overline{1, n-k}\}. \quad (2.23)$$

The space \mathcal{W} is a dense linear subspace in $C([0, 1], V)$. On \mathcal{W} we define the differential operator \mathcal{D} ,

$$(\mathcal{D}\mathbf{v})(x) \doteq \frac{d\mathbf{v}}{dx} + \mathcal{H}(x)\mathbf{v}(x), \quad \mathbf{v} \in \mathcal{W}. \quad (2.24)$$

Statement 2. *If the Condition (2.16) is satisfied, the differential operator $\mathcal{D} : \mathcal{W} \mapsto C([0, 1], \mathbb{V})$ given by (2.24) has a compact inverse $\mathcal{K} : C([0, 1], \mathbb{V}) \mapsto \mathcal{W}$.*

Proof. From Statement 1 we conclude that the equation

$$\mathcal{D}\mathbf{v} = \mathbf{f} \quad (2.25)$$

for $\mathbf{f} \in C([0, 1], \mathbb{V})$ has a unique solution \mathbf{v} in \mathcal{W} , which is presented by Formula (2.22). From this formula we read that the operator $\mathcal{K} = \mathcal{D}^{-1}$ on $C([0, 1], \mathbb{V})$ is given by the following expression

$$(\mathcal{K}\mathbf{f})(x) = \sum_{j=1}^k (\Phi^{-1}(\Psi)\mathbf{f})_j P(x)\mathbf{c}_j + \int_0^x P(x)P(\sigma)^{-1}\mathbf{f}(\sigma)d\sigma. \quad (2.26)$$

Considering the right hand side of this expression we see that the operator \mathcal{K} is composed of two parts, namely, \mathcal{K}_0 and \mathcal{K}_1 . The operator \mathcal{K}_0 defined by $\mathcal{K}_0 \doteq \sum_{j=1}^k (\Phi^{-1}(\Psi)\mathbf{f})_j P(x)\mathbf{c}_j$ is a finite rank operator because its range is spanned by the finite set $\{P(x)\mathbf{c}_1, \dots, P(x)\mathbf{c}_k\}$. The other part, the operator \mathcal{K}_1 defined by $\mathcal{K}_1 \doteq \int_0^x P(x)P(\sigma)^{-1}\mathbf{f}(\sigma)d\sigma$ is a Volterra integral operator with a continuous kernel $P(x)P(\sigma)^{-1}$, and thus compact. Thus, we conclude that \mathcal{K} is compact. \blacktriangle

The result presented in Statement 2 is used in the next section, where we address stability of the linearized systems.

2.2.2 General Issues

We consider the following first order quasi linear hyperbolic system of partial differential equations

$$\mathcal{C}(\mathbf{y})\frac{\partial \mathbf{y}}{\partial t} = \mathcal{A}(\mathbf{y})\frac{\partial \mathbf{y}}{\partial x} + \mathbf{b}(\mathbf{y}), \quad (x, t) \in S, \quad (2.27)$$

with two-point boundary conditions

$$\langle p_i, \mathbf{y}(0, t) \rangle = \xi_i, \quad i = \overline{1, n-k}; \quad (2.28)$$

$$\langle q_j, \mathbf{y}(1, t) \rangle = \zeta_j, \quad j = \overline{1, k}, \quad (2.29)$$

and initial condition

$$\mathbf{y}(x, 0) = \mathbf{y}_0(x). \quad (2.30)$$

In this problem, S is a strip in \mathbb{R}^2 described by $S = [0, 1] \times [0, \infty)$. As in (2.7)-(2.7), sets $\{p_i\}_{i=1}^{n-k}$ and $\{q_j\}_{j=1}^k$ consist of linear functionals on \mathbb{V} , where \mathbb{V} is n -dimensional vector space. Also in (2.27), $\mathcal{A}(\mathbf{y})$ and $\mathcal{C}(\mathbf{y})$ are matrix valued functions, and $\mathbf{b} = \mathbf{b}(\mathbf{y})$ is a vector function. We assume that for every \mathbf{y} the matrix $\mathcal{A}(\mathbf{y})$ is invertible. The matrix $\mathcal{C}(\mathbf{y})$ does not need to be invertible.

The steady state of the system is determined by the equation

$$\mathcal{A}(\mathbf{y})\frac{d\mathbf{y}}{dx} + \mathbf{b}(\mathbf{y}) = 0 \quad x \in [0, 1], \quad (2.31)$$

together with the two-point boundary conditions

$$\langle p_i, \mathbf{y}(0) \rangle = \xi_i, \quad i = \overline{1, n-k}; \quad (2.32)$$

$$\langle q_j, \mathbf{y}(1) \rangle = \zeta_j, \quad j = \overline{1, k}, \quad (2.33)$$

We look for a classical solution of this problem. Since \mathcal{A} is invertible, (2.34) can be written as an ordinary non-linear differential equation in a standard form,

$$\frac{d\mathbf{y}}{dx} = \mathcal{A}(\mathbf{y})^{-1} \mathbf{b}(\mathbf{y}). \quad (2.34)$$

If the right hand side of (2.34) is continuously differentiable with respect to \mathbf{y} , then, given an initial condition $\mathbf{y}(0) = \psi$, there is a unique solution. However, the problem at hand is not an initial value Cauchy problem but a two-point boundary value problem, thus the uniqueness of the solution cannot be obtained from this classical theorem. Questions of existence and uniqueness for the solutions of boundary value problems are much more difficult than for initial value problems, for there is no general theory. There is, however, a vast literature on individual cases, for instance *Bernfeld and Lakshmikantham* [32] present a variety of techniques that may be used. We outline here some necessary conditions for solvability. In order to have a unique solution, the boundary conditions should at least define n independent equations, i.e. both sets $\{p_i\}_{i=1}^{n-k}$ and $\{q_j\}_{j=1}^k$ have to be linearly independent in the dual V^* . Existence of the solution can be proved by applying a fixed point argument based on a suitable fixed point theorem, such as the one of Schauder. We note that a fixed point argument does not guarantee the unicity of the solution. In what follows, we assume that the solution of the (2.34), (2.32), (2.33) exists and is unique.

Suppose we have determined the steady state solution \mathbf{y}_{state} . The next question is to determine whether this state is stable. For this we apply the linear stability theory, which means that we linearize (2.27) about the steady state and consider the stability of the linearized system. Thus, we write $\mathbf{y}(x, t) = \mathbf{y}_{state}(x) + \mathbf{v}(x, t)$. Then the linearization yields $\mathcal{C}(\mathbf{y})$, $\mathcal{A}(\mathbf{y})$, and $\mathbf{b}(\mathbf{y})$ are to be replaced by

$$\mathcal{C}(\mathbf{y}) \doteq \mathcal{C}(\mathbf{y}_{state}) + \partial_{\mathbf{y}} \mathcal{C}(\mathbf{y}_{state}) \mathbf{v}, \quad (2.35)$$

$$\mathcal{A}(\mathbf{y}) \doteq \mathcal{A}(\mathbf{y}_{state}) + \partial_{\mathbf{y}} \mathcal{A}(\mathbf{y}_{state}) \mathbf{v}, \quad (2.36)$$

$$\mathbf{b}(\mathbf{y}) \doteq \mathbf{b}(\mathbf{y}_{state}) + \partial_{\mathbf{y}} \mathbf{b}(\mathbf{y}_{state}) \mathbf{v}, \quad (2.37)$$

where $\partial_{\mathbf{y}} \mathcal{C}$ and $\partial_{\mathbf{y}} \mathcal{A}$ are 3-tensors and $\partial_{\mathbf{y}} \mathbf{b}$ is a 2-tensor. Substituting (2.35)-(2.37) into (2.27) and keeping only the linear terms with respect to \mathbf{v} , we end up with the linearized system

$$C(x) \frac{\partial \mathbf{v}}{\partial t} = A(x) \frac{\partial \mathbf{v}}{\partial x} + B(x) \mathbf{v}, \quad (x, t) \in S, \quad (2.38)$$

with two-point homogeneous boundary conditions

$$\langle p_i, \mathbf{v}(0, t) \rangle = \mathbf{0}, \quad i = \overline{1, n-k}; \quad (2.39)$$

$$\langle q_j, \mathbf{v}(1, t) \rangle = \mathbf{0}, \quad j = \overline{1, k}. \quad (2.40)$$

In the linearized system (2.38), the linear operators A , B , and C are given by the following relations

$$C(x) = \mathcal{C}(\mathbf{y}_{state})(x), \quad (2.41)$$

$$A(x) = \mathcal{A}(\mathbf{y}_{state})(x), \quad (2.42)$$

$$B(x)\mathbf{v} = \partial_{\mathbf{y}}\mathbf{b}(\mathbf{y}_{state})\mathbf{v} + [\partial_{\mathbf{y}}\mathcal{A}(\mathbf{y}_{state})\mathbf{v}] \frac{d\mathbf{y}_{state}}{dx}. \quad (2.43)$$

We recall that the matrix valued function \mathcal{A} is invertible, thus $A(x)$ is an invertible linear mapping on V for all x . Hence, we may write the system (2.38) as

$$A(x)^{-1}C(x) \frac{\partial \mathbf{v}}{\partial t} = \frac{\partial \mathbf{v}}{\partial x} + A(x)^{-1}B(x)\mathbf{v}, \quad (x, t) \in S. \quad (2.44)$$

Since the function $x \mapsto A(x)^{-1}C(x)$ is continuous, the linear operator $\mathcal{G} : C([0, 1], V) \mapsto C([0, 1], V)$ defined by

$$(\mathcal{G}\mathbf{v})(x) = A(x)^{-1}C(x)\mathbf{v}(x), \quad (2.45)$$

is bounded. On \mathcal{W} , the dense linear subspace in the Banach space $C([0, 1], V)$, defined by (2.23),

$$\mathcal{W} = \{\mathbf{v} \in C^1([0, 1], V) \mid \mathbf{v}(0) \in \{p_i\}^0, \mathbf{v}(1) \in \{q_j\}^0, i = \overline{1, k}; j = \overline{1, n-k}\}$$

we introduce the first order differential linear operator \mathcal{D} as follows

$$(\mathcal{D}\mathbf{v})(x) \doteq \frac{d\mathbf{v}}{dx} + H(x)\mathbf{v}(x), \quad \mathbf{v} \in \mathcal{W} \quad (2.46)$$

$$\text{where } H(x) = A(x)^{-1}B(x) \quad (2.47)$$

With these linear operators \mathcal{G} and \mathcal{D} , the problem (2.38)-(2.40) can be presented as

$$\mathcal{G} \frac{d\mathbf{v}}{dt} = \mathcal{D}\mathbf{v}, \quad \mathbf{v} \in \mathcal{W}. \quad (2.48)$$

The operator \mathcal{G} is not necessarily invertible, thus the semigroup theory is not applicable. The densely defined operator \mathcal{D} has a compact inverse \mathcal{K} , see Statement 2, Section 2.2.1. Having said that, we can rewrite (2.48) as

$$\mathcal{K}\mathcal{G} \frac{d\mathbf{v}}{dt} = \mathbf{v}. \quad (2.49)$$

Since the operator \mathcal{G} is bounded, the operator $\mathcal{K}\mathcal{G}$ is compact as a multiplication of a compact and bounded operator. Applying the Laplace transformation to both sides of (2.49) we deduce that

$$(\mathcal{I} - s\mathcal{K}\mathcal{G})\hat{\mathbf{v}} = -\mathcal{K}\mathcal{G}\mathbf{v}_0. \quad (2.50)$$

where $\hat{\mathbf{v}}$ is the Laplace transform of \mathbf{v} , and \mathbf{v}_0 represents the initial condition $\mathbf{v}_0 = \mathbf{v}(0, x)$. Thus, everything comes down to the invertibility of $(\mathcal{I} - s\mathcal{K}\mathcal{G})$, which is essentially equivalent to the spectral problem for the operator $\mathcal{K}\mathcal{G}$. Since $\mathcal{K}\mathcal{G}$ is compact, there are two possibilities:

- $\mathcal{K}\mathcal{G}$ is not a purely spectral operator. That yields that $\mathcal{K}\mathcal{G}$ has a quasi-nilpotent component, i.e. $\mathcal{K}\mathcal{G}$ decomposes into two commutative operators with one of them being quasi-nilpotent, [33]. In this case the spectrum of $\mathcal{K}\mathcal{G}$ does not reveal any conclusion on the stability of the steady state.

- \mathcal{KG} is a purely spectral operator. The spectrum of \mathcal{KG} is discrete, $\{\mu_r | r \in \mathbb{N}\}$, each eigenvalue μ_r has a finite multiplicity and $\mu_r \rightarrow 0$ as $r \rightarrow \infty$. The sum of the eigenspaces is dense in $C([0, 1], V)$, corresponding eigenprojections sum up to the identity. Thus, the resolvent $s \mapsto (I - s\mathcal{KG})^{-1}$ has poles at $\gamma_r = \frac{1}{\mu_r}$, which means that $(\mathcal{I} - s\mathcal{KG})^{-1}$ exists for all s except for a countable number of poles γ_r with finite multiplicity. With that we take the inverse of the Laplace transform of (2.50), deriving the formal solution of the problem (2.38)-(2.40).

$$\mathbf{v}(z, t) = -\frac{1}{2\pi i} \int_{\sigma-i\infty}^{\sigma+i\infty} \hat{\mathbf{v}} e^{st} ds = -\frac{1}{2\pi i} \int_{\sigma-i\infty}^{\sigma+i\infty} (I - s\mathcal{KG})^{-1} \mathcal{KG} \mathbf{v}_0 e^{st} ds. \quad (2.51)$$

If the set of poles γ_r is contained in a sector of the negative real half plane, $|\text{Im}\gamma_r - \pi| < \alpha < \pi/2$, the integral (2.51) is convergent for $t > 0$ and tends to zero as time tends to infinity. That, according to the definition, means asymptotic stability of the solution. Suppose, there is at least one γ_r with $\text{Re}(\gamma_r) > 0$. Then the function $\mathbf{v}(x, t) = \mathbf{v}_r(x) \exp(s_r t)$, where \mathbf{v}_r is an eigenfunction corresponding to γ_r , satisfies Equation (2.49) and is unbounded. This implies that the steady state solution of (2.27)-(2.29) is not stable.

If the set γ_r is neither contained in a sector of the left half plain nor there is a γ_r with $\text{Re}(\gamma_r) > 0$, then on the basis of (2.51) we cannot conclude on the stability/instability of the steady state.

Thus, in order to establish the stability/instability of the steady state for given input parameters, we have to find the spectrum of the operator \mathcal{KG} from the eigenvalue problem

$$\mathcal{KG} \mathbf{u} = \mu \mathbf{u}. \quad (2.52)$$

Returning to the initial notations (see the definition of the operators \mathcal{K} and \mathcal{G}), we see that the problem (2.52) is equivalent to the generalized eigenvalue problem given by the ordinary differential equation

$$A(x) \frac{d\mathbf{u}}{dx} + B(x) \mathbf{u} = \gamma C(x) \mathbf{u}, \quad (2.53)$$

endowed with the homogeneous boundary conditions. In this formulation $\gamma = 1/\mu$. Further, the set of characteristics values $\{\gamma\}$ is also referred to as "spectrum". Equation (2.53) can be obtained directly from (2.38), if the solution of (2.38) is assumed to be of the form

$$\mathbf{v}(x, t) = \mathbf{v}(x) \exp(\gamma t). \quad (2.54)$$

To take a perturbation term in the form (2.54) is a usual practice in the literature on stability considerations. Here we have shown that this approach matches the mathematical derivations.

The remaining question is the calculation of the spectrum $\{\gamma\}$. This is a non-trivial task that usually requires a numerical procedure. The numerical method that we use to calculate the spectrum is discussed in Section 2.3. The derivation of a formal expression of the analytic function, whose zeros determine the γ 's, is given in Appendix A1.

Assuming that the spectrum $\{\gamma\}$ is found, we can address the stability problem. If the spectrum is empty, there is no conclusion from the linear stability analysis on the stability of the steady state. If the spectrum is non-empty, then the γ with the largest real part determines stability. In that case, for each eigenvalue γ we can calculate the corresponding eigenfrequencies f_γ and eigenmode \mathbf{u}_γ . Eigenfrequencies are calculated according to

$$f_\gamma = \left| \frac{\text{Im}\gamma}{2\pi} \right|. \quad (2.55)$$

The corresponding eigenmode can be written as

$$\mathbf{u}_\gamma(x) = A_\gamma(x) \exp(jk_\gamma(x)x). \quad (2.56)$$

Here $A_\gamma(x)$ is the amplitude of the eigenmode determined up to a positive constant and $k_\gamma(x)$ is the phase of the eigenmode. From phase and frequency we calculate the wave velocity of the eigenmode

$$c_\gamma(x) = \frac{f_\gamma}{k_\gamma(x)}. \quad (2.57)$$

Of course these wave velocities reflect the hyperbolicity of the initial system.

2.3 Implementation

In this section we introduce a fast and accurate numerical scheme with which the steady state of (2.27) and the spectrum of the corresponding linearized problem (2.38) can be calculated. The algorithm for calculating the steady state is generic if the right hand side of (2.34) is known; the algorithm for the calculation of the spectrum is generic as soon as the functions A , B , and C are known.

2.3.1 Stationary Problem

Generally, the steady state problem, presented as

$$\frac{d\mathbf{y}}{dz} = \mathcal{A}(\mathbf{y})^{-1} \mathbf{b}(\mathbf{y}), \quad z \in (0, 1) \quad (2.58)$$

$$\langle p_i, \mathbf{y}(0) \rangle = \xi_i, \quad i = \overline{1, k}; \quad (2.59)$$

$$\langle q_j, \mathbf{y}(1) \rangle = \zeta_j, \quad j = \overline{1, n-k}, \quad (2.60)$$

requires numerical solving. For the aspects of solving boundary value problems numerically, one can refer, for instance, to *Keller* [34], *Kramer* [35], *Ascher et al.* [36], *Ascher and Petzold* [37], *Quarteroni et al.* [38], *Mattheij and Molenaar* [39]. Herein, we present an outline of an algorithm that we used to solve (2.58) - (2.60). We start with a shooting method. That is, we introduce the parameter $\kappa \in \mathbb{R}^{n-k}$, by which we replace the boundary condition (2.60) specified in $z = 1$ with the conditions specified in $z = 0$

$$\langle q_j, \mathbf{y}(0) \rangle = \kappa_j, \quad j = \overline{1, n-k}. \quad (2.61)$$

Now, for any given κ , the problem (2.58)-(2.60) becomes a classical Cauchy problem (2.58), (2.59), (2.61). To find a solution of this problem, one can use a 4-th order Runge-Kutta method that is known for its accuracy in solving ODE systems. Because we are interested in the specific solution that satisfies the condition in point $x = 1$, we have to find a value of the parameter κ , which leads to that solution. To achieve that we suggest the following algorithm:

- 1 take a random value for κ ;
- 2 solve the System (2.58), (2.59), (2.61);
- 3 check whether the found solution satisfies condition (2.60);
 - 3.1 if the answer is "not", then adapt the κ -value and go to step 2.
 - 3.2 if the answer is "yes", then the solution of (2.58)-(2.60) is found.

2.3.2 Linearized Problem

From the previous section we learn that the equation

$$A(x) \frac{d\mathbf{u}}{dx} + B(x)\mathbf{u} = \gamma C(x)\mathbf{u}, \quad x \in (0, 1) \quad (2.62)$$

has at most a countable number of characteristic values γ with corresponding eigenstates \mathbf{u}_γ . We found a formal expression for the analytic function whose zeros determine γ 's, we presented the formal expression for the eigenmodes, and we found the necessary and sufficient condition such that the system of equations

$$A(x) \frac{d\mathbf{u}}{dx} + B(x)\mathbf{u} = \mathbf{f}(x) \quad (2.63)$$

with associated 2-point boundary conditions has a unique solution. It turned out that the inverse of $(A \frac{d}{dx} + B)$ is compact. Thus we can apply the usual numerical techniques, such as Galerkin, collocation, or projection methods to solve the equations. Here we present a modification of the Galerkin method based on splines. We describe the method in general, and in the end become more specific. We approximate the solution \mathbf{u} by an expansion with the well chosen spline basic functions $\{s_l\}_{l=1}^{N+2}$ related to a collection of equidistant nodes $\{x_l\}_{l=1}^{N+2}$, $x_l = \frac{l-1}{N+1}$, partitioning the interval $[0, 1]$. Thus we write

$$\mathbf{u} = \sum_{l=1}^{N+2} \beta_l s_l, \quad (2.64)$$

where $\beta_l \in \mathbb{R}^n$, are expansion vector coefficients. Introducing \mathbf{u} as given in (2.64) into equation (2.62), we obtain

$$\gamma \sum_{l=1}^{N+2} C(x) \beta_l s_l = \sum_{l=1}^{N+2} B(x) \beta_l s_l + \sum_{l=1}^{N+2} A(x) \beta_l \frac{ds_l}{dx}. \quad (2.65)$$

Equation (2.62) is supposed to be satisfied in a weak sense if for all test functions $\varepsilon_k s_l$, where $k = 1, \dots, D$ and $l = 1, \dots, N + 2$,

$$\gamma(\varepsilon_k s_l, C(x) \mathbf{u}) = (\varepsilon_k s_l, B(x) \mathbf{u}) + \left(\varepsilon_k s_l, A(x) \frac{d\mathbf{u}}{dx} \right). \quad (2.66)$$

Here (\cdot, \cdot) denotes the inner product,

$$(\mathbf{v}, \mathbf{w}) = \int_0^1 (\mathbf{v}(x), \mathbf{w}(x))_{\mathbb{R}^D} dx, \quad (2.67)$$

and $\{\varepsilon_k\}_{k=1}^n$ the standard basis of \mathbb{R}^n . Accordingly, we work out Equation (2.62) and get

$$\begin{aligned} \gamma \sum_{l=1}^{N+2} \int_0^1 (\varepsilon_k, C(x) \boldsymbol{\beta}_l)_{\mathbb{R}^n} s_j(x) s_l(x) dx &= \\ &= \sum_{l=1}^{N+2} \int_0^1 \{(\varepsilon_k, B(x) \boldsymbol{\beta}_l)_{\mathbb{R}^n} s_j(x) s_l(x) + (\varepsilon_k, A(x) \boldsymbol{\beta}_l)_{\mathbb{R}^n} s_j(x) s_l'(x)\} dx. \end{aligned} \quad (2.68)$$

Each spline s_j has a support point x_j . Thus for N sufficiently large, we can approximate the three integrals in the above equation as

$$\int_0^1 (\varepsilon_k, C(x) \boldsymbol{\beta}_l)_{\mathbb{R}^n} s_j(x) s_l(x) dx \doteq (\varepsilon_k, C(x_j) \boldsymbol{\beta}_l)_{\mathbb{R}^n} S_{jl}, \quad (2.69)$$

$$\int_0^1 (\varepsilon_k, B(x) \boldsymbol{\beta}_l)_{\mathbb{R}^n} s_j(x) s_l(x) dx \doteq (\varepsilon_k, B(x_j) \boldsymbol{\beta}_l)_{\mathbb{R}^n} S_{jl}, \quad (2.70)$$

$$\int_0^1 (\varepsilon_k, A(x) \boldsymbol{\beta}_l)_{\mathbb{R}^n} s_j(x) s_l'(x) dx \doteq (\varepsilon_k, A(x_j) \boldsymbol{\beta}_l)_{\mathbb{R}^n} T_{jl}, \quad (2.71)$$

where

$$S_{jl} = \int_0^1 s_j(x) s_l(x) dx, \quad (2.72)$$

$$T_{jl} = \int_0^1 s_j(x) s_l'(x) dx. \quad (2.73)$$

In matrix form the equations are written as

$$\gamma \tilde{C} \begin{pmatrix} \boldsymbol{\beta}_0 \\ \cdot \\ \cdot \\ \cdot \\ \boldsymbol{\beta}_N \end{pmatrix} = \tilde{B} \begin{pmatrix} \boldsymbol{\beta}_0 \\ \cdot \\ \cdot \\ \cdot \\ \boldsymbol{\beta}_N \end{pmatrix} + \tilde{A} \begin{pmatrix} \boldsymbol{\beta}_0 \\ \cdot \\ \cdot \\ \cdot \\ \boldsymbol{\beta}_N \end{pmatrix} \quad (2.74)$$

where the matrices \tilde{C} , \tilde{B} and \tilde{A} have dimension $(N+2)n \times (N+2)n$ and are in a block form described as

$$\tilde{C} = \begin{pmatrix} C(x_1) S_{1,N+2} & \cdot & \cdot & \cdot & C(x_{N+2}) S_{1,N+2} \\ \cdot & & & & \cdot \\ \cdot & & & & \cdot \\ \cdot & & & & \cdot \\ C(z_1) S_{N+2,1} & & & & C(x_{N+2}) S_{N+2,N+2} \end{pmatrix} = \text{diag}(C(x_1), \dots, C(x_{N+2})) \mathcal{S} \quad (2.75)$$

with

$$\mathcal{S} = \begin{pmatrix} S_{1,1} I_D & \cdot & \cdot & \cdot & S_{1,N+2} I_D \\ \cdot & & & & \cdot \\ \cdot & & & & \cdot \\ \cdot & & & & \cdot \\ S_{N+2,1} I_n & & & & S_{N+2,N+2} I_n \end{pmatrix} \quad (2.76)$$

and I_n is the $n \times n$ identity matrix;

$$\tilde{\mathcal{B}} = \text{diag}(B(x_1), \dots, B(x_{N+2})) \mathcal{S} \quad (2.77)$$

and

$$\tilde{\mathcal{A}} = \text{diag}(A(x_1), \dots, A(x_{N+2})) \mathcal{T} \quad (2.78)$$

with

$$\mathcal{T} = \begin{pmatrix} T_{1,1} I_n & \cdot & \cdot & \cdot & T_{1,N+2} I_n \\ \cdot & & & & \cdot \\ \cdot & & & & \cdot \\ \cdot & & & & \cdot \\ T_{N+2,1} I_n & & & & T_{N+2,N+2} I_n \end{pmatrix}. \quad (2.79)$$

Consider the homogeneous boundary condition at $x = 0$: $\langle p_i, \mathbf{u}(0) \rangle = 0$, $i = \overline{1, n-k}$. Let s_1, \dots, s_m , $N > 2m - 2$, be the splines that are non-zero in $x = 0$. Then the boundary condition at $x = 0$ reads

$$\sum_{r=1}^m s_r(0) \langle p_i, \boldsymbol{\beta}_r \rangle = 0, \quad i = \overline{1, n-k}. \quad (2.80)$$

This is a set of linear homogeneous equations for the vector coefficients $\boldsymbol{\beta}_1, \dots, \boldsymbol{\beta}_m$. Thus, we have $(n-k)$ equations for (mn) unknowns, which means that $mn - (n-k)$ coefficients are free and the others can be expressed in terms of them. For the sake of notation take

$$\mathbf{b} = (\boldsymbol{\beta}_1, \dots, \boldsymbol{\beta}_m)^T \in \mathbb{R}^{mn} \quad (2.81)$$

Then we may assume that

$$\begin{pmatrix} b_1 \\ \cdot \\ \cdot \\ \cdot \\ b_{n-k} \end{pmatrix} = \mathcal{Z}_0 \begin{pmatrix} b_{n-k+1} \\ \cdot \\ \cdot \\ \cdot \\ b_{mn} \end{pmatrix} \doteq \mathcal{Z}_0 \mathbf{b}_0 \quad (2.82)$$

for a matrix $\mathcal{Z}_0 \in \mathbb{R}^{(n-k) \times (mn - (n-k))}$. A similar matrix $\mathcal{Z}_1 \in \mathbb{R}^{k \times (mn-k)}$ and a vector $\mathbf{b}_1 \in \mathbb{R}^{mn-k}$ exist describing the boundary condition in $x = 1$. Thus, we find

$$\boldsymbol{\beta} = \begin{pmatrix} \boldsymbol{\beta}_1 \\ \cdot \\ \cdot \\ \cdot \\ \boldsymbol{\beta}_{N+2} \end{pmatrix} = \begin{pmatrix} \mathcal{Z} & \emptyset \\ I_0 & \\ & I \\ & & I_1 \\ \emptyset & & \mathcal{Z} \end{pmatrix} \begin{pmatrix} \mathbf{b}_0 \\ \boldsymbol{\beta}_{m+1} \\ \cdot \\ \boldsymbol{\beta}_{N+2-m} \\ \mathbf{b}_1 \end{pmatrix} \doteq \mathcal{Z} \boldsymbol{\beta}_{red} \quad (2.83)$$

Here I_0 is the identity matrix with dimension $mn - (n - k)$, I_1 is the identity matrix with dimension $mn - k$, and I is the identity matrix with dimension $N + 2 - 2m$. Define $\tilde{\mathcal{A}} = \tilde{\mathcal{A}}\mathcal{Z}$, $\tilde{\mathcal{C}} = \tilde{\mathcal{C}}\mathcal{Z}$, and $\tilde{\mathcal{B}} = \tilde{\mathcal{B}}\mathcal{Z}$, then the initial system with the incorporated boundary conditions is discretized by

$$[\gamma\tilde{\mathcal{C}}_{red} - (\tilde{\mathcal{B}}_{red} + \tilde{\mathcal{A}}_{red})]\boldsymbol{\beta}_{red} = 0. \quad (2.84)$$

Let us further introduce the following notation

$$\mathcal{M} = \tilde{\mathcal{B}}_{red} + \tilde{\mathcal{A}}_{red} \quad \text{and} \quad \mathcal{N} = \tilde{\mathcal{C}}_{red}.$$

In terms of \mathcal{M} and \mathcal{N} , Equation (2.84) becomes the generalized eigenvalue problem

$$[\gamma\mathcal{N} - \mathcal{M}]\boldsymbol{\beta}_{red} = 0. \quad (2.85)$$

The solution of this equation is obtained from the eigenvalue problem

$$[(M^T M)^{-1} M^T N - \mu \mathcal{I}]\boldsymbol{\beta}_{red} = 0, \quad (2.86)$$

where $\mu = \gamma^{-1}$. With this we conclude the generic description of our numerical method, which is applicable to a spectral analysis of Equation (2.62).

In our implementation we use linear splines s_1, \dots, s_{N+2} , where each node corresponds to one spline that has value 1 in that node and 0 in the other nodes. Then the nonzero elements of the matrices \mathcal{S} and \mathcal{T} are given by

$$S_{j,j} = \frac{2}{3(N+1)}, \quad S_{j,j-1} = \frac{1}{6(N+1)}, \quad S_{j,j+1} = \frac{1}{6(N+1)}, \quad j = 2, \dots, N+1,$$

$$S_{1,1} = \frac{1}{3(N+1)}, \quad S_{1,2} = \frac{1}{6(N+1)},$$

$$S_{N+2,N+1} = \frac{1}{6(N+1)}, \quad S_{N+2,N+2} = \frac{1}{3(N+1)},$$

and

$$T_{j,j-1} = -\frac{1}{2}, \quad j = 2, \dots, N+2, \quad T_{j,j+1} = \frac{1}{2}, \quad j = 1, \dots, N+1,$$

$$T_{1,1} = -\frac{1}{2}, \quad T_{N+2,N+2} = \frac{1}{2}.$$

The reduction matrix \mathcal{Z} has the same form as before, namely

$$\mathcal{Z} = \begin{pmatrix} \mathcal{Z}_0 & \emptyset \\ I_0 & \\ & I \\ & & I_1 \\ \emptyset & & & \mathcal{Z}_1 \end{pmatrix},$$

where in this case $\mathcal{Z}_0 \in R^{(n-k) \times k}$, $\mathcal{Z}_1 \in R^{k \times (n-k)}$, I_0 is the identity matrix with dimension k , I_1 is the identity matrix with dimension $(n - k)$, and I is the identity matrix with dimension N .

2.4 Illustration and Validation

In this section we present two examples in which we demonstrate the accuracy of our implementation. Moreover, we want to clarify the role of eigenfrequencies and eigen-phases of the related eigen-modes. In the first example we present a generalization of the classical wave equation and in the second example we consider a simple way of describing a fiber spinning process and compare our results with the ones from literature.

2.4.1 Generalized Wave Equation

We consider the stability of the steady state $\mathbf{u} = 0$ of the linear system of the form (2.27) with \mathcal{A} , \mathcal{C} and \mathbf{b} defined by

$$\mathcal{A} = \mathcal{I}, \quad (2.87)$$

$$\mathcal{C} = \begin{pmatrix} 0 & 1 \\ a^2 - b^2 & 2b \end{pmatrix}, \quad a > b > 0, \quad (2.88)$$

$$\mathbf{b} = \mathbf{0}. \quad (2.89)$$

The system consists of two equations for a two-dimensional state $\mathbf{u} = (u, v)$,

$$\frac{\partial \mathbf{u}}{\partial x} = \mathcal{C} \frac{\partial \mathbf{u}}{\partial t}, \quad (x, t) \in (0, 1) \times (0, \infty). \quad (2.90)$$

We consider (2.90) supplemented with the boundary conditions

$$u(0, t) = u(1, t) = 0. \quad (2.91)$$

System (2.90) is totally hyperbolic. The roots of the characteristic equation are the eigenvalues of \mathcal{C} ; the matrix \mathcal{C} has two real different eigenvalues

$$\lambda_1 = b + a, \quad \lambda_2 = b - a. \quad (2.92)$$

We include the analysis of the problem (2.90)-(2.91) for two reasons. First, this simple hyperbolic system represents the main concept of the systems describing traveling waves in polymeric filaments. Second, a straightforward calculation yields the analytical solution of this problem. These two reasons allow us to introduce the concept of a traveling wave described by the eigenmodes of the system, and to validate our numerical technique by comparing numerical results with results derived analytically. We are interested in the spectrum and the corresponding eigenmodes of the system (2.90). For that we put

$$\mathbf{u}(x, t) = \mathbf{U}(x)e^{\gamma t}, \quad (2.93)$$

where $\mathbf{U} = (U, V)^T$. Then the complex amplitude \mathbf{U} satisfies the following system

$$\frac{d\mathbf{U}}{dx} = \gamma \mathcal{C} \mathbf{U}. \quad (2.94)$$

The solution of this system can be written as

$$\mathbf{U}(x) = c_1 e^{\lambda_1 \gamma x} \mathbf{U}_1 + c_2 e^{\lambda_2 \gamma x} \mathbf{U}_2 \quad (2.95)$$

where λ_1 and λ_2 are the eigenvalues of the matrix \mathcal{C} given by (2.92), and \mathbf{U}_1 and \mathbf{U}_2 are the corresponding eigenvectors, $\mathbf{U}_1 = (1, b+a)^\top$ and $\mathbf{U}_2 = (1, b-a)^\top$. Substituting expressions for $\lambda_1, \lambda_2, \mathbf{U}_1$ and \mathbf{U}_2 into (2.95), we obtain the general solution of (2.94) in the form

$$\mathbf{U}(x) = e^{\gamma b x} (C_1 \mathbf{U}_1 e^{\gamma a x} + C_2 \mathbf{U}_2 e^{-\gamma a x}). \quad (2.96)$$

Using the boundary conditions, we obtain the following expression for the characteristic values

$$\gamma_n = \pm \frac{n\pi}{a} i, \quad n \in \mathbb{N}. \quad (2.97)$$

The components of the eigenmodes $\mathbf{U}_{\pm n}$ corresponding to γ_n are

$$U_{\pm n}(x) = e^{\pm \frac{n\pi b x}{a} i} \sin(n\pi x), \quad (2.98)$$

$$V_{\pm n}(x) = e^{\pm \frac{n\pi b x}{a} i} (b \sin(n\pi x) \mp i a \cos(n\pi x)). \quad (2.99)$$

We focus on the first component of the n -th eigenmode, U_n . Writing U_n in polar form

$$U_n(x) = A_n(x) e^{i\phi_n(x)}, \quad (2.100)$$

we obtain its amplitude $A_n(x)$, and its phase $\phi_n(x)$:

$$A_n(x) = |\sin n\pi x|, \quad (2.101)$$

$$\text{and } \phi_n(x) = \frac{n\pi b}{a} x + [nx]\pi. \quad (2.102)$$

Here $[\cdot]$ denotes the Entier function. In combination with the time factor $e^{\gamma_n t}$, the modes U_n determine the waves

$$\text{Re}(U_n e^{\gamma_n t}) = \cos\left(\frac{n\pi b}{a} \left(x + \frac{1}{b} t\right)\right) \sin(n\pi x), \quad (2.103)$$

$$\text{Im}(U_n e^{\gamma_n t}) = \sin\left(\frac{n\pi b}{a} \left(x + \frac{1}{b} t\right)\right) \sin(n\pi x). \quad (2.104)$$

The expressions (2.103), (2.104) describe waves that travel from $x = 1$ to $x = 0$ with the velocity $c_{tr} = \frac{1}{b}$ with knots in the points $x = \frac{k}{n}, k = 0, \dots, n$. We note that in case $b = 0$, the equations (2.103), (2.104) describe the classical wave equation with eigenmodes that are standing waves

$$\cos\left(\frac{n\pi}{a} t\right) \sin(n\pi x), \quad \sin\left(\frac{n\pi}{a} t\right) \sin(n\pi x). \quad (2.105)$$

Obviously, in case $b < 0$, the waves are traveling from $x = 0$ to $x = 1$,

$$\cos\left(\frac{n\pi b}{a} \left(x - \left|\frac{1}{b}\right| t\right)\right) \sin(n\pi x), \quad \sin\left(\frac{n\pi b}{a} \left(x - \left|\frac{1}{b}\right| t\right)\right) \sin(n\pi x). \quad (2.106)$$

This ends the classical analysis. Next we show that our numerical procedure, described in the previous section, is capable in handling this problem. In Figure 2.1 we present the resulting characteristic spectra of the problem considered, calculated by applying the numerical technique explained in Section 2.3.2. The calculations were carried out with the number of discretization

nodes $N = 200$. Generally, the calculation takes a few seconds. Calculations are performed for 4 cases, namely, when $a = 1, 2, 3$ and 4 . According to (2.97), the actual spectra corresponding to the selected values of the parameter a are

$$a = 1 \Rightarrow \gamma_n = \pm n\pi i, \quad n \in \mathbb{N}, \quad (2.107)$$

$$a = 2 \Rightarrow \gamma_n = \pm \frac{n\pi}{2} i, \quad n \in \mathbb{N}, \quad (2.108)$$

$$a = 3 \Rightarrow \gamma_n = \pm \frac{n\pi}{3} i, \quad n \in \mathbb{N}, \quad (2.109)$$

$$a = 4 \Rightarrow \gamma_n = \pm \frac{n\pi}{4} i, \quad n \in \mathbb{N}. \quad (2.110)$$

Comparing the numerical results with the actual results given by (2.107)-(2.110), we conclude that our numerical technique is very accurate in estimating the spectrum $\{\gamma\}$ of hyperbolic systems, like the one under consideration. Figure 2.2 presents amplitude and phase for the first component of the first ($n = 1$) and the second ($n = 2$) eigenmode found for the two different sets of parameters: $a = 2, b = 1$, and $a = 4, b = 1$. We observe that the phase is a continuous linear function; both phase and amplitude agree perfectly with the ones given by formulas (2.102) and (2.101).

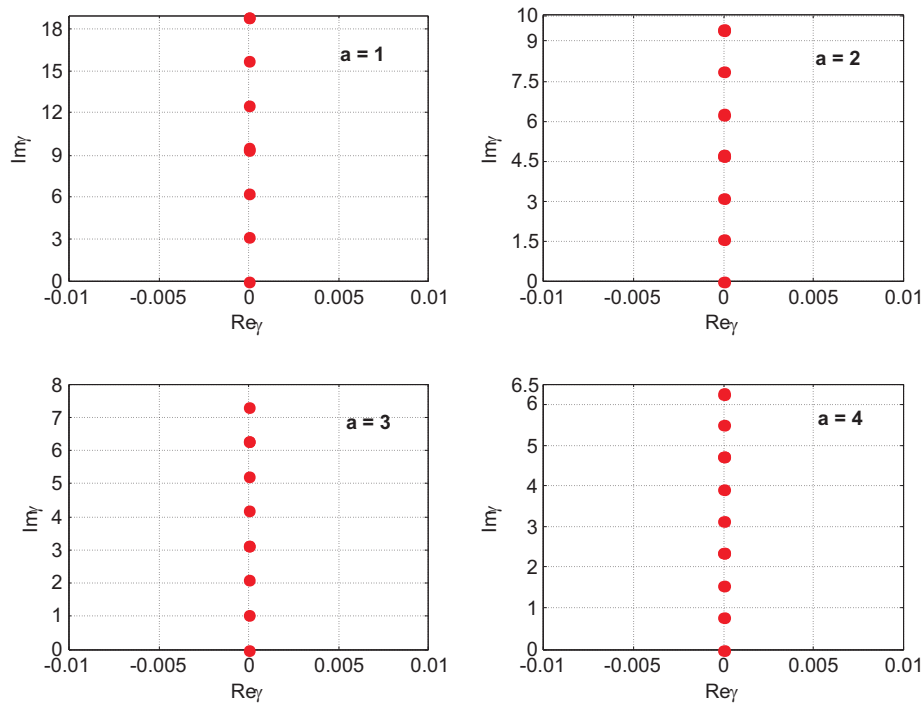


Figure 2.1: Numerically found characteristic spectra of the problem (2.94) for the following values of parameter a : $a = 1, 2, 3, 4$.

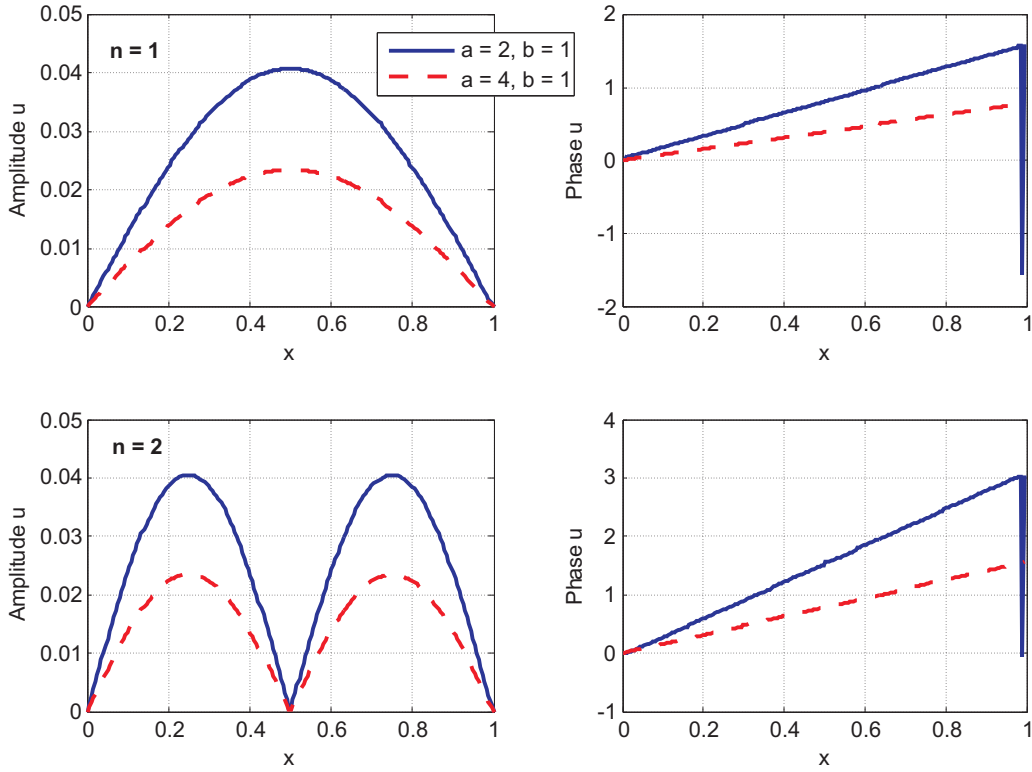


Figure 2.2: Numerically found amplitude and phase of the U_1 and U_2 , first and second eigenmodes. Two different sets of parameters are considered: $(a, b) = (2, 1)$ and $(a, b) = (4, 1)$.

2.4.2 Fiber Spinning: Simple Model

As explained in the introduction, we are interested in practical applications, namely in the prediction the draw resonance instability occurring in polymer elongation processes. Therefore, in this section we consider a fiber spinning process described by a simple model to validate our numerical routine.

We adopt a model discussed in recent literature by *Hagen and Langwallner*, [40]. In this model it is assumed that the cross-section of the polymer fluid filament is circular and that the radial variations are small compared to the fiber drawing length. Surface tension and gravity are neglected but viscous and inertial forces are accounted for. Then the governing equations describing the process of forced elongation (equations of conservation of mass and momentum) take the following dimensionless form

$$\frac{\partial a}{\partial t} + \frac{\partial(ua)}{\partial x} = 0, \quad (2.111)$$

$$Re a \left(\frac{\partial u}{\partial t} + u \frac{\partial u}{\partial x} \right) = \frac{\partial}{\partial x} \left(a \frac{\partial u}{\partial x} \right), \quad (2.112)$$

and associated 2-point boundary conditions

$$a(0, t) = u(0, t) = 1, \quad u(1, t) = Dr. \quad (2.113)$$

In this hyperbolic system x , $x \in [0, 1]$, and t , $t \in [0, \infty)$, are the independent variables denoting the normalized flow direction and the normalized time, respectively. The point $x = 0$ denotes

the source of the polymer fluid. The point $x = 1$ denotes the position where the pulling force is applied. The functions $a(x, t)$ and $u(x, t)$ denote the area of cross-section of the polymer flow and the axial velocity of the polymer flow, respectively. The parameter Re denotes the Reynolds number, $Re = \rho u R / \eta$ with R - radius of the cross-section, the parameter Dr - the dimensionless final velocity imposed by the pulling force. The parameter Dr actually represents a ratio between the final and the initial flow velocities and is called "draw ratio".

The problem (2.111)-(2.113) was recently discussed by *Hagen and Langwallner*, [40]. After applying a linear stability analysis, they solve the resulting spectral problem by employing the Chebyshev collocation method, and they present several spectra for different values of the parameters Dr and Re . This allows us to use [40] as a validation reference for our numerical routine used to calculate the spectrum. Without repeating the analysis of the results, we use the same values of the parameters Dr and Re and compare the spectra obtained with our methodology with those presented in [40].

In order to solve (2.111)-(2.113), we reduce the order of the system by introducing the state variable $w = \frac{\partial u}{\partial x}$. After the corresponding steady state (a_0, u_0, w_0) is found¹, we linearize the system around the steady state, and arrive at the following linear problem

$$A(x) \frac{\partial \mathbf{y}}{\partial x} + B(x) \mathbf{y} = C(x) \frac{\partial \mathbf{y}}{\partial t}, \quad x \in (0, 1), \quad (2.114)$$

$$a_p(0) = u_p(0) = 0, \quad u_p(1) = 0, \quad (2.115)$$

where the matrices A , B , and C are given by

$$A = \begin{pmatrix} u_0 & 0 & 0 \\ -w_0 & 0 & a_0 \\ 0 & -1 & 1 \end{pmatrix}, \quad C = \begin{pmatrix} -1 & 0 & 0 \\ 0 & -Re a_0 & 0 \\ 0 & 0 & 0 \end{pmatrix}, \quad (2.116)$$

$$B = \begin{pmatrix} w_0 & \frac{da_0}{dx} & a_0 \\ Re u_0 w_0 - \frac{dw_0}{dx} & Re a_0 w_0 & Re u_0 a_0 - \frac{da_0}{dx} \\ 0 & 0 & 1 \end{pmatrix} \quad (2.117)$$

Applying now the numerical routine discussed in Section 2.3, we calculate the spectra $\{\gamma\}$ from the problem (2.114)-(2.115) for the parameters $Dr = 34$, and $Re = 0.035$ and 0.06 . The comparison between the spectra obtained and the ones given in [40] is presented in Figure 2.3. In both cases we observe perfect agreement, especially for the leading values in the spectra.

Let us now look at the frequencies determined by the values of the spectrum calculated for $Dr = 34$ and $Re = 0.035$, see Figure 2.4. We observe that the frequencies form a shifted harmonic complex, where the first mode frequency is approximately $2.30f_c$ Hz, and the difference between each next frequency is $3.45f_c$ Hz. Here f_c is the characteristic frequency determined by the characteristic time of the process according to $f_c = 1/t_c$. In Figure 2.5 we present the amplitude and the phase of the cross-sectional area a_p and the flow velocity u_p corresponding to the first mode in the spectrum.

¹The calculation of the steady state is not an issue; thus we do not present here the solution of the steady state of (2.111)-(2.113). If interested in steady state, see [40].

Taking the phase of the velocity at $x = 0$ equal to 0, the eigenstate of the velocity is determined up to a positive constant. Therefore, we can determine phase differences between state components, phase changes in a state component, and the relative amplitude. From the phase being increasing or decreasing, we conclude that the wave is traveling towards or from the die exit, respectively. To conclude the direction of the wave we have to take the phase corresponding to the characteristic value with the positive imaginary part. We note that we cannot conclude anything about the size of the wave traveling through the polymer filament because the amplitude is found up to a constant. However, we see the shape of the wave. Also, based on the phase information, we conclude that the wave velocity increases slightly as the wave travels.

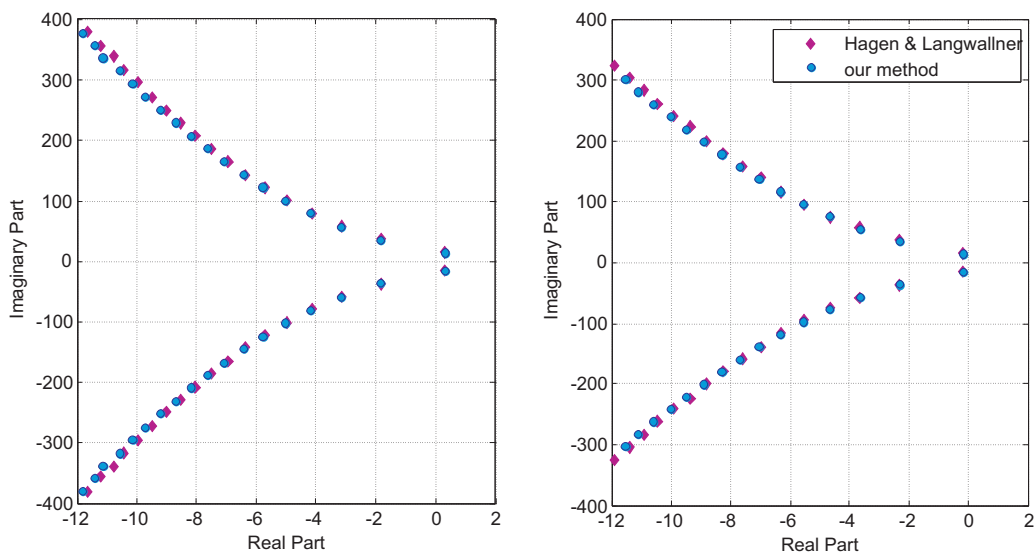


Figure 2.3: Characteristic spectra for $Dr = 34$, and $Re = 0.035$ (left), $Re = 0.06$ (right). Comparison between our numerical calculations and the one from Hagen and Langwallner, [40].

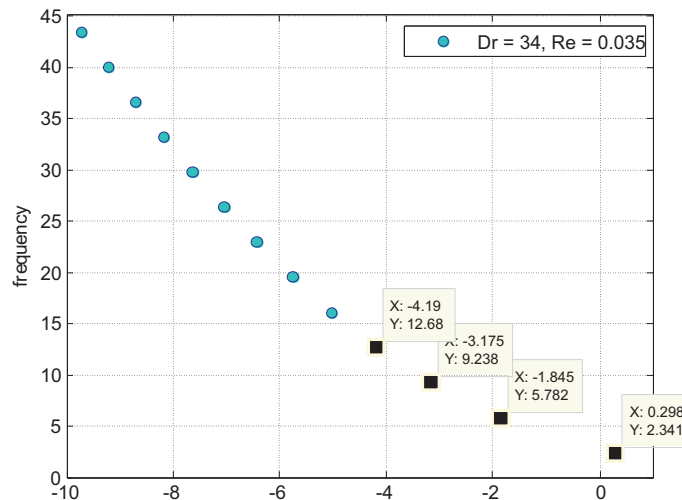


Figure 2.4: Frequencies correspondent to the spectrum obtained for $Dr = 34$ and $Re = 0.035$.

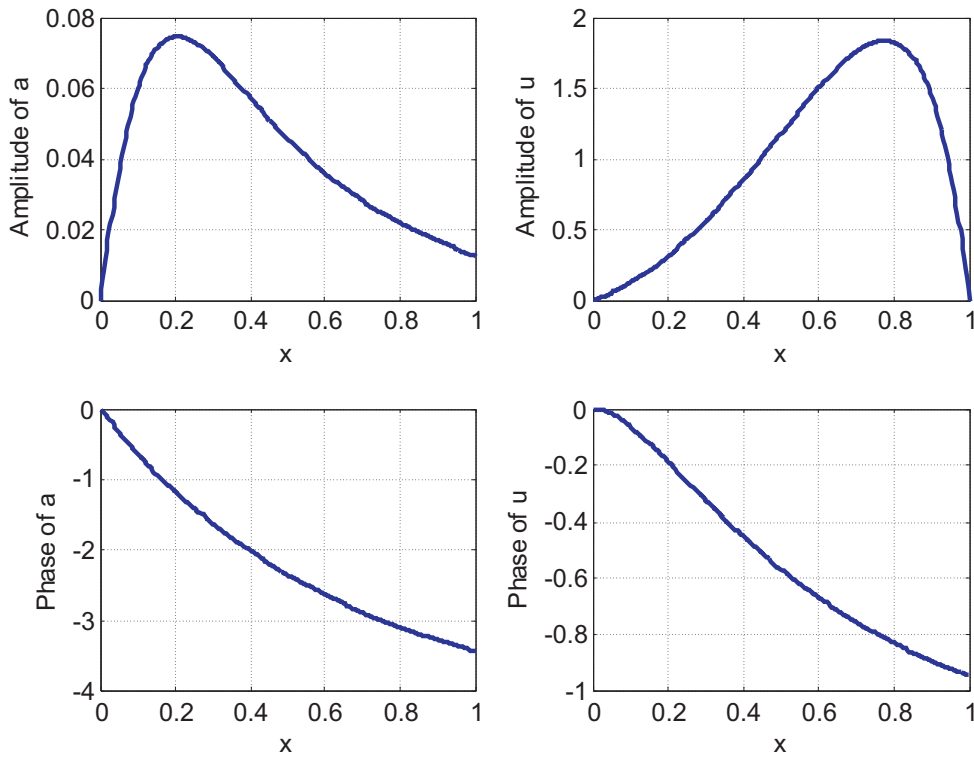


Figure 2.5: *The amplitude and the phase of the eigenstates corresponding to the leading value in the spectrum of (2.114)-(2.115) calculated for $Dr = 34$ and $Re = 0.035$*

2.5 Conclusions

In this chapter we consider a general mathematical description of polymer elongation processes, which is a hyperbolic system of quasi-linear differential equations with two-point boundary conditions. We prove applicability of linear stability analysis to tackle the problem whether the steady state is stable or not. For that we showed that the differential operator that drives the linear system has a compact inverse and concluded that the spectrum of the linearized hyperbolic system is discrete. This conclusion is essential as it indicates that numerical calculations of the spectrum of eigenvalues and the corresponding eigenmodes make sense. The numerical routine developed to calculate the spectrum is based on a modified Galerkin approach, using local basis functions and a novel way to incorporate the homogeneous boundary conditions. We demonstrate the routine to work splendidly for two benchmark problems; it produces a spectrum without spurious modes, in contrast to other methods used to determine spectra of hyperbolic systems, and, furthermore, within a reasonable calculation time. The complete spectrum with eigenmodes is calculated in a few seconds on a standard PC with one processor and 256 Mb of operational memory. The mathematical strategy developed, both the model as well as the implementation, allows us to tackle real processes using more adequate viscoelastic constitutive equations in the next chapters.

Appendix A

A1 Formal Expression for Spectrum

We consider the eigenvalue problem

$$\mathcal{K}\mathcal{G}\mathbf{u}(x) = \mu\mathbf{u}(x), \quad (\text{A-1})$$

or the equivalent generalized eigenvalue problem

$$\mathcal{D}\mathbf{u}(x) = \gamma\mathcal{G}\mathbf{u}(x), \quad \text{where } \gamma = \frac{1}{\mu}. \quad (\text{A-2})$$

For the definition of the operators \mathcal{G} , \mathcal{D} , and \mathcal{K} see formulas (2.45), (2.46), and (2.26) in Section 2.2.2. Here we shall derive a formal expression for the eigenvalues of $\mathcal{K}\mathcal{G}$. We note that \mathcal{K} maps the space $C([0, 1], \mathbf{V})$ onto \mathcal{W} . Thus, \mathbf{u} that satisfies the eigenvalue equation (2.52) belongs to \mathcal{W} . We assume that solution \mathbf{u} can be found in the following form:

$$\mathbf{u}(x) = P(x)\mathbf{v}(x), \quad (\text{A-3})$$

where \mathbf{v} is in $C([0, 1], \mathbf{V})$; and the matrix function $P(x)$ is the fundamental solution of the system $\mathcal{D}\mathbf{u} = 0$. If \mathbf{u} satisfies (A-1) then $\mathbf{v}(x)$ satisfies $\mathbf{v}(0) = \mathbf{u}(0)$ and

$$\mathbf{v}(z) = \mathbf{v}(0) + \gamma \int_0^z P(\sigma)^{-1}C(\sigma)P(\sigma)\mathbf{v}(\sigma)d\sigma. \quad (\text{A-4})$$

Now we define the operator \mathcal{J} on $C([0, 1], \mathbf{V})$ by

$$(\mathcal{J}\mathbf{v})(x) = \int_0^x P(\sigma)^{-1}C(\sigma)P(\sigma)\mathbf{v}(\sigma)d\sigma. \quad (\text{A-5})$$

The operator \mathcal{J} is compact and quasi-nilpotent because

$$\|\mathcal{J}^n\| \leq \frac{M^n}{n!} \quad \text{where } M = \max_{\sigma \in [0,1]} \|P(\sigma)\|C(\sigma)\|P(\sigma)^{-1}\|. \quad (\text{A-6})$$

This yields that the map $\lambda \mapsto (\mathcal{I} - \lambda\mathcal{J})^{-1}$ is entirely analytic, i.e. $(\mathcal{I} - \lambda\mathcal{J})^{-1}$ exists for all λ ,

$$(\mathcal{I} - \gamma\mathcal{J})^{-1} = \sum_{n=0}^{\infty} \gamma^n \mathcal{J}^n \quad (\text{A-7})$$

Using (A-5) and introducing the mapping $\Theta : \mathbf{V} \rightarrow C([0, 1], \mathbf{V})$ such that

$$(\Theta\mathbf{c})(z) = \mathbf{c}, \quad (\text{A-8})$$

we can rewrite Eq. (A-4) in the following way

$$\mathbf{v} = \Theta[\mathbf{u}(0)] + \gamma\mathcal{J}\mathbf{v}. \quad (\text{A-9})$$

The solution of this equation is then given by

$$\mathbf{v}_\gamma = (\mathcal{I} - \gamma\mathcal{J})^{-1}\Theta[\mathbf{u}(0)] \quad (\text{A-10})$$

and thus \mathbf{u}_γ defined by $\mathbf{u}_\gamma(x) = P(x)\mathbf{v}_\gamma$ satisfies Equation (A-2).

Next we determine the γ 's by considering the homogeneous conditions in $x = 0$ and in $x = 1$. Following the approach we already used while proving Statement 1, see (2.18), we write

$$\mathbf{u}(0) = \sum_{j=1}^{n-k} \phi_j \mathbf{c}_j, \quad (\text{A-11})$$

Additionally, we introduce the mapping $\mathcal{H} : C([0, 1], V) \rightarrow V$ such that

$$\mathcal{H}\mathbf{v} = \mathbf{v}(1). \quad (\text{A-12})$$

With (A-11) and (A-12), the boundary condition in $z = 1$ reads

$$\sum_{j=1}^{n-k} \phi_j \langle q_i, \mathcal{F}_\gamma \mathbf{c}_j \rangle = 0, \quad (\text{A-13})$$

where the operator $\mathcal{F}_\gamma : V \rightarrow V$ is defined by the following

$$\mathcal{F}_\gamma = P(1)\mathcal{H}(\mathcal{I} - \gamma\mathcal{J})^{-1}\Theta \quad (\text{A-14})$$

If G_γ denotes the matrix $(\langle q_i, \mathcal{F}_\gamma \mathbf{c}_j \rangle)$ then the coefficient array $\{\phi_j\}$ is in the kernel of that matrix. Therefore, Equation (A-2), and so Equation (A-1), has a non-trivial solution \mathbf{u}_γ if and only if $\det(G_\gamma) = 0$. Since the function $\gamma \mapsto \det(G_\gamma)$ is analytic, there can be at most a countable number of zeros. The collection of zeros is called the spectrum. It is equivalent to the spectrum of the operator $\mathcal{K}\mathcal{G}$ in a sense that $\mu = 1/\gamma$. Knowing the aspects of \mathcal{F}_γ gives knowledge on the behavior of the spectrum.

CHAPTER THREE

Rheotens

3.1 Introduction

3.1.1 Background

In polymer forming simulations, an important aim is to discover the best processing windows for a given material without running the actual processes by tedious trial and error experiments. In practice, simulation software is often used with simple rheological models only that are not up to the complexity of the real polymer behavior. More complex polymer constitutive models are under-used, even if they are implemented, because their parameters are not known a priori and are difficult to determine. This is especially true for the transient elongational viscosity of polymer melts and solutions that is extremely difficult to capture. A way to estimate model parameters is to apply the model in question to simulate some generated data from the chosen experiment. The model parameters are then defined as the best fitting parameters that make a correspondence between the simulated data and the experimental data.

In this context, this chapter addresses the Rheotens experiment as an appropriate candidate for model parameter estimation. The Rheotens experiment is a lab-scale fiber spinning experiment. A polymer melt is extruded through a capillary die and stretched in the air under the action of a drawing force. The drawing force is imposed and measured by a device developed by *Meissner* [41; 42]. Actually, the device is called "Rheotens", but nowadays also the experiment is referred to as Rheotens. The scheme of the Rheotens tester can be seen in Figure 3.1.¹

¹Both pictures are taken from the official brochure of the Rheotens 71.97 tensile tester available at the web-page of the producer www.goettfert.com

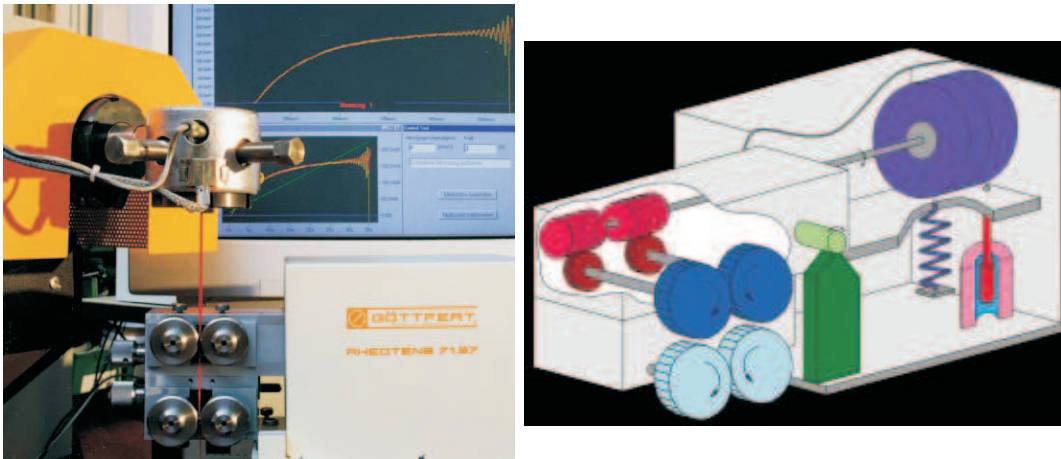


Figure 3.1: experimental set-up for Rheotens measurements (left), and a scheme of an actual Rheotens unit (right)

3.1.2 Literature Review

The Rheotens test has found widespread application both in industry (for characterization purposes) and in scientific research for polymer properties investigations or process modeling. In particular, we mention: *Meissner* [43], who proved the sensitivity of the Rheotens test with respect to small changes in polymer properties; *White and Yamane* [44], and *Field et al.* [45] who found correlations between the Rheotens melt strength and filament extensibility with bubble stability and minimum film thickness in film blowing. *La Mantia and Acierno* [46] reported on the influence of molecular mass on melt strength and extensibility of linear and branched polyethylenes. *Ghijssels et al.* investigated melt strength of polyethylenes [47], polyethylene blends [48], and polypropylenes [49]. All of these tests were performed at a constant mass flow rate and their results can only represent a qualitative comparison of melt strength because of the non-isothermal stretching and prehistory of the polymer melt in the die and extruder.

For the more meaningful rheological results (in a quantitative sense), *Sampers and Leblanc* [50], carried out tensile flow measurements by extruding the melt strand into a thermostatted chamber so that drawing was carried out isothermally. *Wagner et al.* [51] proposed Rheotens mastercurves for thermo-rheologically simple polymer melts, which provide a rheologically correct basis for a quantitative comparison of Rheotens flow curves. *Bernnat* (see *Bernnat et al.* [52], *Bernnat* [53]) extended the latter work, proving the existence of various mastercurves.

In a Rheotens experiment elongation of the polymer melt is performed under the action of a tensile drawing force, and not at a prescribed elongation rate. Therefore, the Rheotens test does not provide an elongational viscosity directly, as in the case of an uniaxial elongational rheometer (RME or SER). Thus, for fundamental analysis, a model of the Rheotens process is needed. *Laun and Schuch* [54] assumed a Newtonian fluid approximation in their research, i.e., the filament diameter decreases exponentially with the distance from the die. *Rauschenberger and Laun* [55] developed

a recursive algorithm to solve the equations of motion of the elongated strand complemented by a single integral constitutive equation of the Wagner model under the condition of a constant drawing force. A similar numerical scheme was developed by *Fulchiron et al.* [56]. *Wagner et al.* [57; 58] proposed a model, where the elongational viscosity is a function of the draw ratio only. This model, however, does not have a rheological constitutive equation basis. Recently *Doufas* [61] presented a full approach for modeling and analysis of the Rheotens experiment. He considered and modeled the Rheotens experiment as a small-scale fiber spinning process. *Doufas*' model combines the filament transport equations (mass, momentum, and energy) with differential type constitutive equations (modified Giesekus model). *Doufas* was also the first who used Rheotens to determine parameters of the modified Giesekus constitutive model. His work is our starting point.

3.1.3 Objective

There are two procedures for running Rheotens: (i) the "acceleration mode", where the velocity of the wheels is increased according to a specified constant acceleration and the force is measured as a function of velocity; (ii) the "constant mode", where the velocity of the wheels is kept constant for a certain measurement time, and the force is measured as a function of time. The graphs depicting measurement data show force oscillations after a certain drawing velocity is reached. These oscillations represent a stretching-related instability, called "draw resonance". Thus, Rheotens establishes two different polymer operational regimes: stable and unstable.

In literature, when referring to the Rheotens experiment, only the acceleration mode is considered and not the constant mode; from the resulting curve only the part related to the stable operation is fitted (*Doufas* [61]). In this chapter, we study the constant mode of operating Rheotens and demonstrate its applicability and importance for parameter estimation. The constant mode results provide the precise value of the onset velocity of draw resonance. Additionally, by applying the Fourier Transformation to the discrete time signal given by the force versus time measurements, we obtain the frequency of the transversal oscillations of the fiber diameter. In this chapter we describe a method to determine the model parameters from the measurement data obtained from both, the acceleration and the constant mode. From acceleration mode we rely on the results of a stable operation, and from the constant mode we use the results related to an instable operation. Simulations of a low density polyethylene (LDPE), a linear low density polyethylene (LLDPE), a polypropylene (PP), and a polystyrene (PS) with a modified Giesekus constitutive model demonstrate the accuracy and efficiency of the method.

3.2 Rheotens Experiment

3.2.1 Description

The Rheotens experiment set-up system consists of a single-screw extruder with a gear pump, a reservoir with a changeable circularly shaped small die, and the actual Rheotens device for filament stretching. The extruder provides a constant polymer mass throughput Q at initial temperature

T_0 . This temperature is imposed by heating elements in the extruder and near the die. Local temperature variation due to e.g. viscous heating is usually neglected. In the experiments presented here, a die was used with an entrance angle $\beta = 60^\circ$, a length $L_{die} = 60$ mm, and a diameter $d_{die} = 2.5$ mm. The values of entrance angle and length of the die affect the pressure in the barrel, the die diameter affects the extrusion velocity of the polymer. Upon exiting the die, the polymer melt initially swells after which it elongates due to the pulling motion of the take-up wheels. The distance between the die exit and the take-up wheels, L , is typically 100 mm but may vary from experiment to experiment. The final velocity of the filament u_f is directly related to the wheel velocity. At the take-up point the drawing force is measured. The measurement frequency varies from 5 Hz to 100 Hz. The total number of measurement data points can go up to 10000. The measurement error is $\pm 10^{-3}$ N. The Rheotens test is non-isothermal. The air into which the sample is extruded is not climate-controlled, but is assumed to be at room temperature and quiescent.

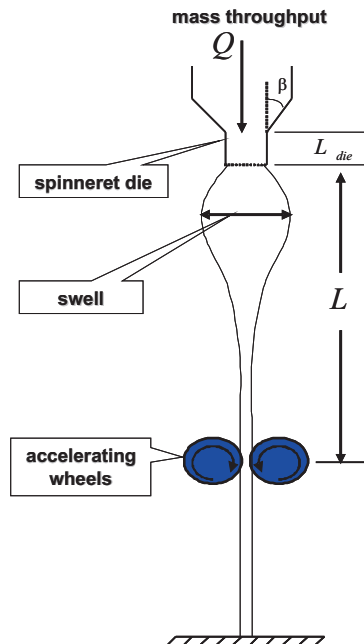


Figure 3.2: Scheme of the Rheotens experiment

Acceleration Mode

We recall that there are two procedures to run Rheotens. In the standard procedure, called here the "acceleration mode", the take-up wheels are rotating with a constant acceleration a , and thus impose a change in final velocity u_f of the polymer flow. The tensile force F , which is required to stretch the filament, is continuously measured at the wheels as a function of the take-up velocity.

An example of the typical output of the acceleration mode for a linear low-density polyethylene is given in Figure 3.3, where the horizontal axis represents the take-up velocity in millimeters per second, and the vertical axis presents the tensile, draw-down force in Newton. The measurements were performed for an acceleration of 24 mm/s^2 with a sampling frequency of 100 Hz, i.e. 100 measurements a second were taken. The maximum drawing velocity achieved is called drawability

of the melt; the maximum force value at rupture is called melt strength.

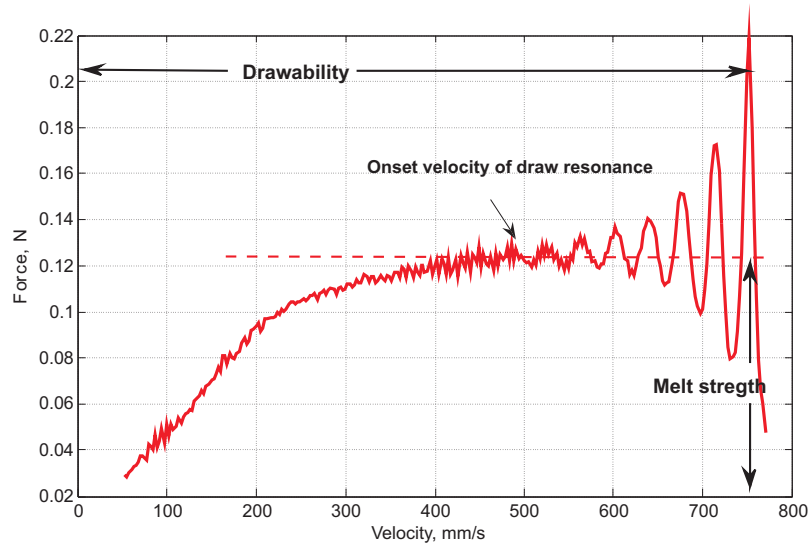


Figure 3.3: Acceleration mode, $a = 24 \text{ mm/s}^2$. LLDPE resin: $Q = 600 \text{ g/h}$, $T_{extr} = 190^\circ \text{C}$, $L = 0.1 \text{ m}$

Constant Mode

In the "constant mode" procedure, the velocity of the wheels is kept constant, taken from a predefined range. The tensile force is measured as a function of time. An example of the output of the constant mode operation is given in Figure 3.4. The experiment was done for a linear low-density polyethylene. In Figure 3.4 the horizontal axis represents the time in seconds, the right vertical axis represents the tensile force in Newton, and the left vertical axis represents the take-up velocity, in millimeters per second. The measurements were performed at a sampling frequency of 10 Hz. We observe that at low velocities the variation in force level is small, in the range of the measurement error. As the velocity reaches a value of 500 mm/s, the amplitude of the force oscillations increases significantly, indicating that draw resonance is present. Increase of the velocity above 500 mm/s yields further increase of the amplitude of oscillations.

Further in this chapter, we discuss the onset velocities of draw resonance for different materials and different processing conditions. We determine the onset velocities by analyzing the force-time-velocity plots, as the one given in Figure 3.4. The error in determining the onset velocities depends on the measurement resolution, i.e. the velocity step chosen in the measurements. The measurement resolution varies for the different experiments. For instance, in the experiment considered in Figure 3.4, at a velocity of 475 mm/s the process is stable, and at a velocity of 500 mm/s, the next taken, the process is unstable. Therefore, the critical velocity is reported in the range of 475 – 500 mm/s. Similarly, everywhere further, the critical velocity is reported to be in a certain interval, where the lower boundary indicates the last value of velocity leading to stable processing, and the

higher boundary indicates the first value of the velocity at which draw resonance is observed.

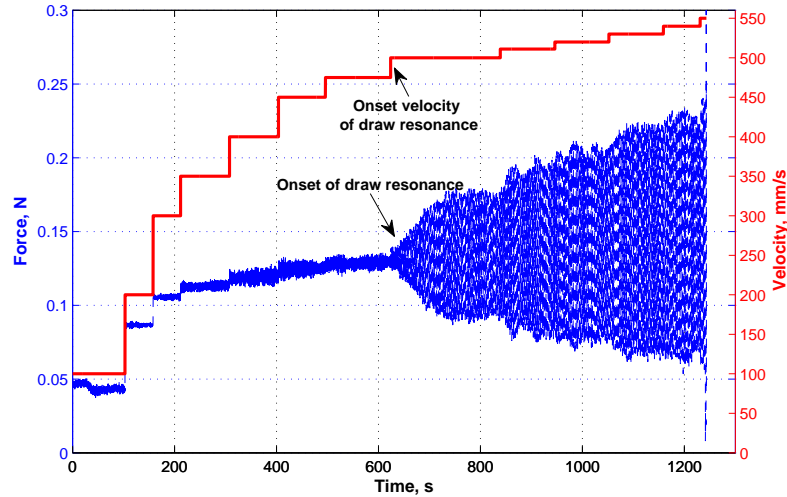


Figure 3.4: Constant mode: draw velocity is piece-wise constant. LLDPE resin: $Q = 600 \text{ g/h}$, $T_{extr} = 190^\circ \text{C}$, $L = 0.1 \text{ m}$

Frequency Data

The data presented in Figure 3.4 is basically a discrete-time signal with a sampling frequency of 10 Hz. Treating them as such, we find the frequency of a force signal for any chosen velocity. Let us consider the data from the segment related to the onset velocity of draw resonance, $v = 500 \text{ mm/s}$ (see Figure 3.5, right diagram). By applying the Discrete Fourier Transformation to these time series, we obtain the amplitude spectrum depicted in the right diagram in Figure 3.5. In this Figure the horizontal axis shows frequencies up to 5 Hz, the vertical axis shows amplitudes in dB,

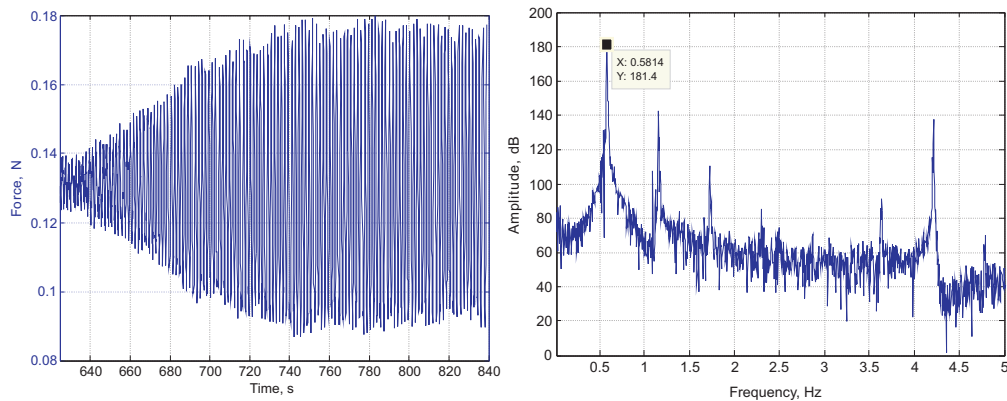


Figure 3.5: *LLDPE 1: $Q = 600$ g/h, $T_{extr} = 190^\circ\text{C}$, $L = 0.1$ m. Picture on the left: constant mode force measurements for $v = 500$ mm/s (onset of the draw resonance). Picture on the right: amplitude spectrum of force signal obtained after application of the Fourier Transformation to all data depicted in the left picture.*

which is achieved by the following transformation:

$$A[dB] = 20 \log_{10} \left(\frac{A[N]}{A_0[N]} \right). \quad (3.1)$$

We take $A_0 = 10^{-5}$ N, which makes the scale such that value of 0 dB denotes an amplitude equal to 10^{-5} N. Keep in mind that A_0 is not "measurable", as the measurement error is 10^{-3} N. So in the amplitude spectrum we do not observe amplitudes with dB smaller than 0. In the spectrum we observe a harmonic complex with a basic frequency of 0.58 Hz, which corresponds to the frequency of the force oscillations in the draw resonance.

Further, we use the term "onset frequency" that is defined as the peak frequency related to the force signal measured at the onset velocity. As the experimental onset velocity is determined within a range, we calculate the onset frequency for the highest value of the velocity in the given range. For instance, if the onset velocity is 475-500 mm/s, then the onset frequency of 0.58 Hz is related to 500 mm/s.

The absolute error of the frequency calculations depends on the measurement sampling frequency and the total number of measurement data points. The frequency bin size is then given by

$$\text{frequency bin size} = \frac{f_s}{N}, \quad (3.2)$$

and the absolute error of the frequency calculations is half of the bin size. In the considered example (Figure 3.5), the sampling frequency is 10 Hz, and the total number of measurements is 2150, which means that absolute error is 0.0023 Hz. In all other experiments, we take a sampling frequency of 10 Hz and a sampling horizon of 110 s, which means that the number of samples is 1100. Therefore the frequency bin size is 0.009 Hz, which yields the absolute error of 0.0045 Hz.

3.2.2 Materials

All materials used in the experiments described in this thesis were provided by the Dow Chemical Company. Selected materials belong to 4 different classes:

1. *low density polyethylene*; we use 300E that is referred to as "LDPE".
2. *linear low density polyethylene*; we consider two materials of this class, namely DOWLEX™ NG5056,² further denoted by "LLDPE 1", and DOWLEX™ NG5056.01, further denoted as "LLDPE 2".
3. *polypropylene*; we use DH109.00, which is referred to further simply as "PP".
4. *polystyrene*; material STYRON™ 648 is considered, it is denoted further by "PS".

The emphasis of our analysis is on the experiments with LDPE and LLDPE2 that were designed and carried out within the scope of this Ph.D. project. Additionally, we make use of the results of the experiments with LLDPE1, PP, and PS that were carried out at Dow in 2005 within the framework of the 3PI (Postpone Polymer Processing Instabilities) project. In our work we apply the new analysis tools to some of those 2005-data.

An overview of various material properties of all tested resins is given in Table 3.1. The melt index (MI) is determined according to the ASTM D1238 method (190°C, 2.16 kg for LLDPE1, LLDPE2; 230°C, 2.16 kg for PP; 200°C, 5 kg for PS.) Solid density is determined according to ASTM D792 method. The molecular mass distribution data are obtained using a Waters 150C instrument via triple detector gel permeation chromatography (GPC). It is noteworthy, however, that the Mw data should be treated as indicative only because it was obtained in different experiments with different calibration. Measurements of viscosity and relaxation time spectra at a reference temperature of 190°C are presented in Figures 3.6 and 3.7.

Table 3.1: Material properties

Name	Resin	MI (g/10min)	Mw (g/mol)	Mn (g/mol)	Mz (g/mol)	E_a (kJ/mol)	Solid density (kg/m ³)
LLDPE1	DOWLEX™ NG5056	1.05	105000	30000	279000	34.6	919
LLDPE2	DOWLEX™ NG5056.01G	1.03	136000	50000	367000		910
LDPE	300E	0.81	96600	15300	366000	57.7	924
PP	DH 109.00	0.28	495000	114000	1950000	41.4	902.3
PS	STYRON™ 648	1.3	296000	136000	462000	114.1	1046.8

² ™ - Trademark of The Dow Chemical Company

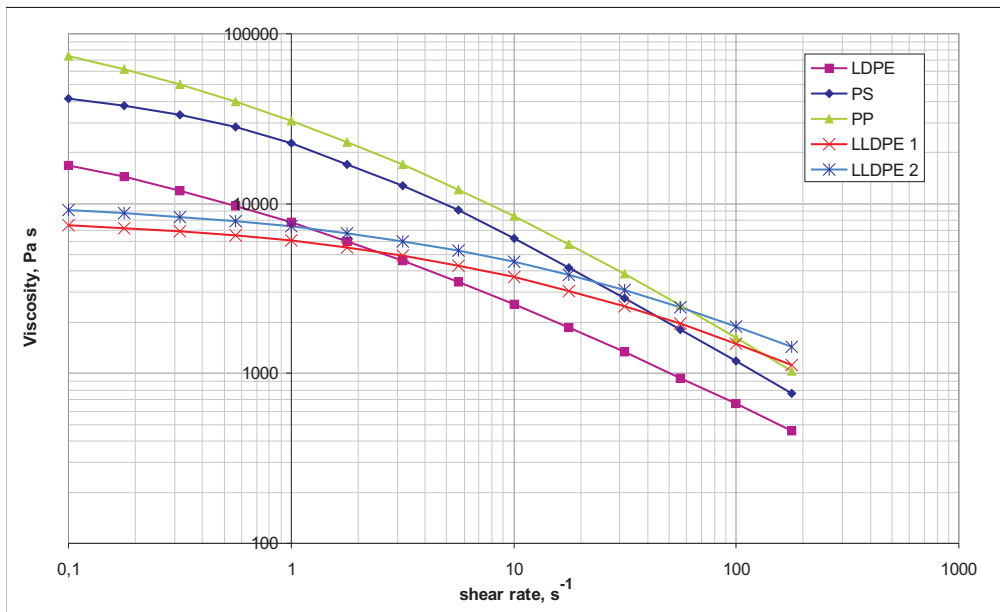


Figure 3.6: Viscosity data for the tested materials at 190°C.

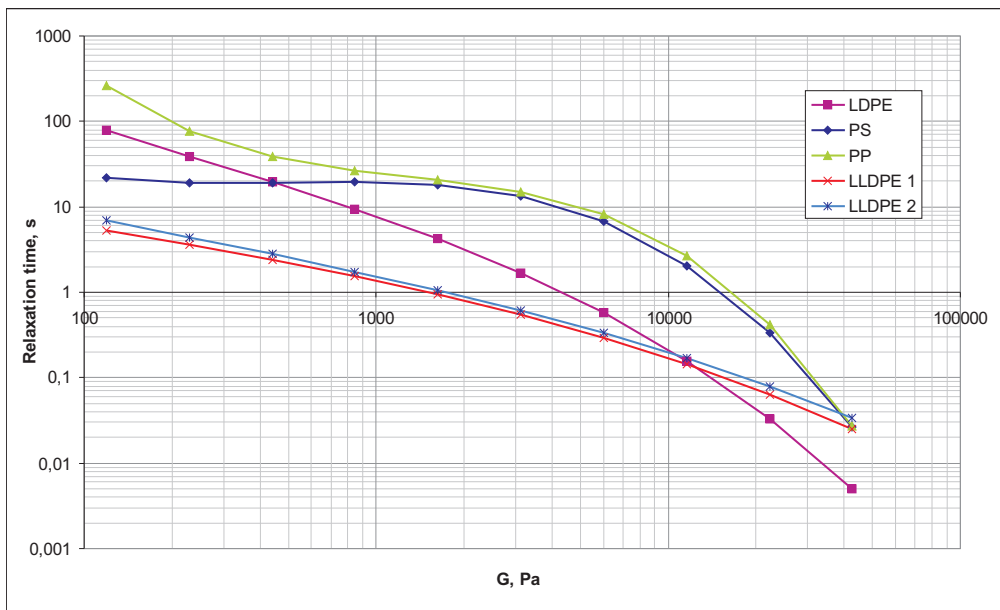


Figure 3.7: Relaxation time spectra for the tested materials at 190°C.

3.2.3 Influence of Operating Conditions

Before using the experimental data for analysis, it is important to know what the factors are that influence the experimental outcome. In Rheotens, one can choose different types of take-up wheels, flat or grooved; different dimensions of the gap between the wheels, from 0.1 mm to 0.6 mm; and different sampling frequencies of force measurements, from 5 to 100 Hz. Additionally, the Rheotens software contains a hardware filter, called damping factor, that is applied to the measurement data. This damping factor can range from 1 to 100, but by default it is set to 10. Finally, operating in the acceleration mode, we can choose different values of the acceleration, ranging from 0.12 mm/s² to 120 mm/s².

Acceleration Mode

We test the acceleration mode for an LLDPE 2 under various conditions, regardless how obvious the answer might seem. First, we notice that the measurement sampling frequency does not influence the resulting curve; this result is visualized in Figure 3.8. Next, we test the influence of the damping factor, more precisely, we look at the difference between the results obtained with the default value of this parameter, which is equal to 10, and the minimal damping, which is 1. We conclude that this change does not influence the resulting Rheotens curves significantly, see Figure 3.9. The data obtained with the minimal damping are more noisy, and filtering (increase of damping factor to 10) makes the curve smoother, but it does not influence the appearance of the draw resonance oscillations.

Figures 3.10 and 3.11 show the Rheotens curves obtained at different values of wheel's acceleration. The visible oscillations of force start sooner if the acceleration is smaller. Besides that these figures also demonstrate that the curve obtained at $a = 24 \text{ mm/s}^2$ is always somewhat lower than the ones obtained at $a = 2.4$ and $a = 0.24 \text{ mm/s}^2$. The force values obtained at constant velocity (see Figure 3.11) are at the same level as force values obtained at low acceleration. This observation is important: when we fit the Rheotens curves to obtain parameters, we sometimes use experimental curves that are obtained at $a = 24 \text{ mm/s}^2$.

Another conclusion from our tests of the acceleration mode is that it does not really matter whether we use the grooved or the flat wheels, when the gap between the wheels is 3 mm. This fact is supported by Figure 3.12. The figure also confirms the reproducibility of the experiment. The size of the gap between the wheels influences the outcome, see Figure 3.13. The smaller the gap the higher the drawability. The curves presented in Figure 3.13 are obtained with different wheels because the gap between the grooved wheels cannot be set smaller than 3 mm; for the 3 mm gap there is no difference in the surface of the wheels; and for the flat wheels the gap of 6 mm in the last stages of drawing becomes too big, i.e. the filament is thinner than 6 mm, thus the Rheotens equipment reports a breakage, while it does not happen.

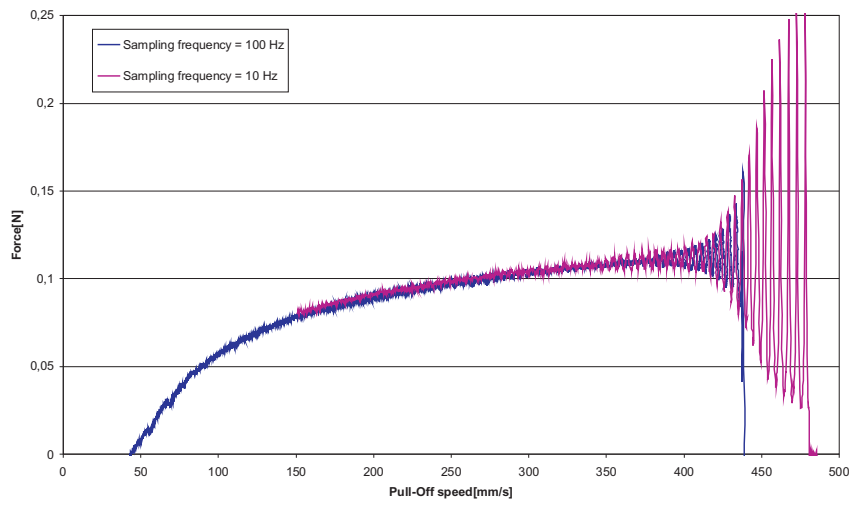


Figure 3.8: Acceleration mode, $a = 2.4 \text{ mm/s}^2$, gap = 0.3 mm, grooved wheels, LLDPE2: $Q = 600 \text{ g/h}$, $T_{extr} = 190^\circ \text{C}$, $L = 0.1 \text{ m}$

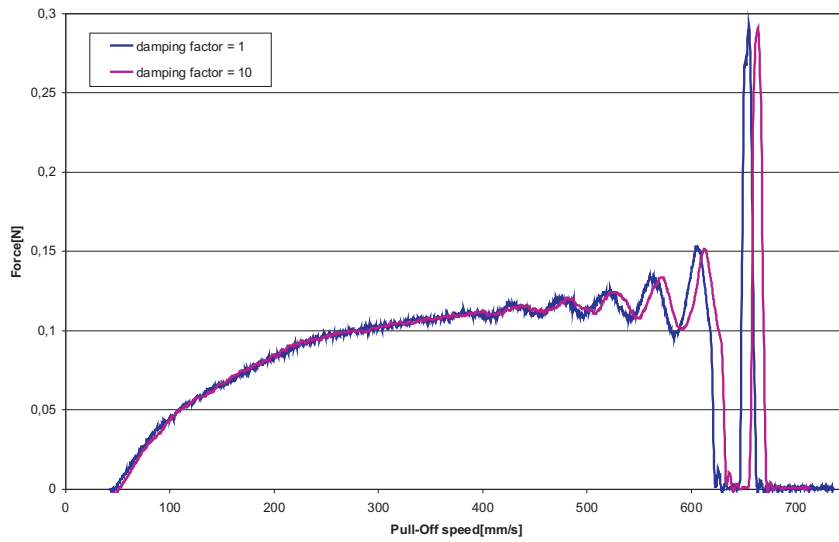


Figure 3.9: Acceleration mode, $a = 2.4 \text{ mm/s}^2$, gap = 0.3 mm, flat wheels, LLDPE2: $Q = 600 \text{ g/h}$, $T_{extr} = 190^\circ \text{C}$, $L = 0.1 \text{ m}$

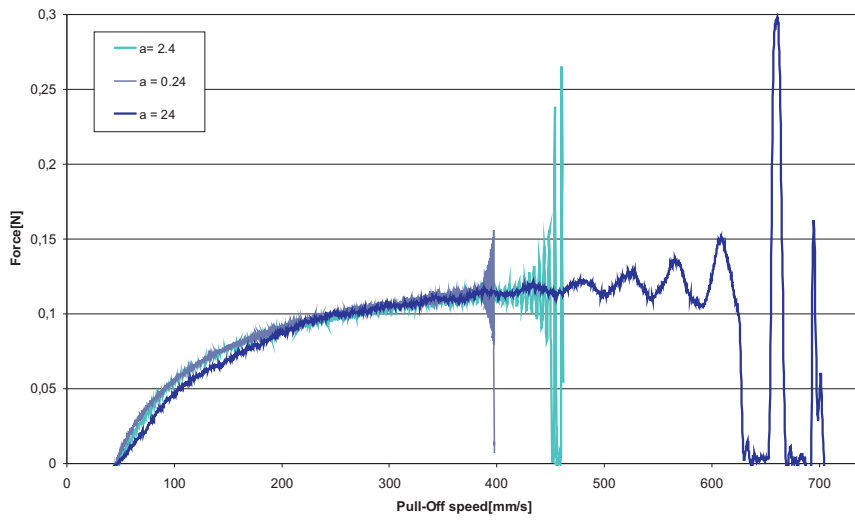


Figure 3.10: Acceleration mode, LLDPE2: $Q = 600 \text{ g/h}$, $T_{extr} = 190^\circ\text{C}$, $L = 0.1 \text{ m}$

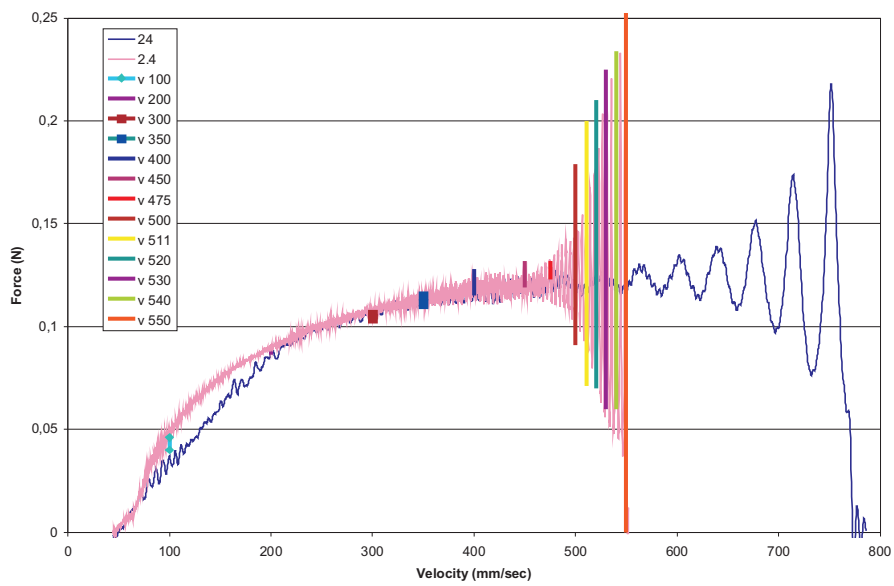


Figure 3.11: Acceleration mode. LLDPE1: $Q = 600 \text{ g/h}$, $T_{extr} = 190^\circ\text{C}$, $L = 0.1 \text{ m}$

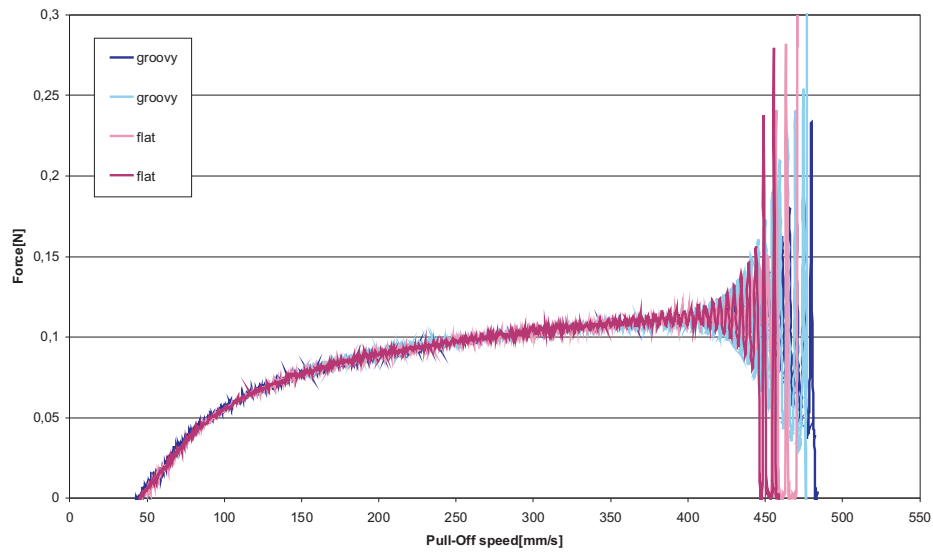


Figure 3.12: Acceleration mode, $a = 2.4 \text{ mm/s}^2$, gap = 0.3 mm. LLDPE2: $Q = 600 \text{ g/h}$, $T_{extr} = 190^\circ\text{C}$, $L = 0.1 \text{ m}$

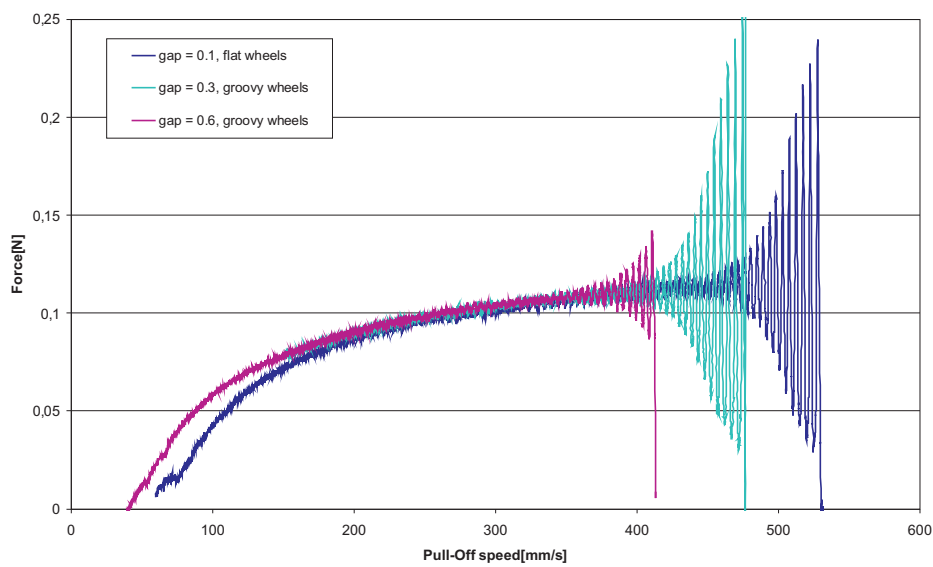


Figure 3.13: Acceleration mode, $a = 2.4 \text{ mm/s}^2$. LLDPE2: $Q = 600 \text{ g/h}$, $T_{extr} = 190^\circ\text{C}$, $L = 0.1 \text{ m}$

Constant Mode

The next step is to study and analyze the influence of the operating conditions on the outcome of the constant mode Rheotens. The results of the studies are presented in Tables 3.2, 3.3, and 3.4. We remind that the way we determine the onset velocity and frequency are described in Sections 3.2.1 and 3.2.1, where the absolute error of the measurements and calculations is also presented.

In Table 3.2 the impact of a change in damping factor on the results of constant mode Rheotens measurements is presented. The onset velocity and onset frequency are listed in columns 4 and 5 for LLDPE2 and LDPE, both for damping factor 1 and 10. In columns 6 and 7, velocities other than onset and related frequencies are given. Because for velocities higher than critical, a harmonic complex shows in the amplitude spectrum for LLDPE, but not for LDPE (discussion follows in Section 3.2.4), in column 7 we present three values of the frequency for LLDPE 2, one basic frequency and two higher harmonics, and one value of the frequency for LDPE. Analyzing the results, we conclude that, as in the case of acceleration, the change in damping factor from 1 to 10 does not influence the onset velocity. However, the frequencies calculated for the same velocities might become slightly lower.

In Table 3.3, we list the results of the evaluation of the different wheel surfaces, flat and grooved, for LLDPE2 and LDPE. A damping factor of 1 and a gap size of 0.3 mm are taken in these experiments. The use of flat or grooved wheels does not result in large differences in the frequencies obtained at the same velocities. Moreover, as may be seen from column 6, Table 3.3, these frequencies coincide. The onset velocities obtained with flat and grooved wheels differ only by 10 mm/s, which is within our error margin.

Finally, in Table 3.4, we present the results of experimenting with two different sizes of the gap between the wheels in the Rheotens constant mode for LLDPE2 and LDPE. Other conditions were kept as follows: drawing length is 100 mm, damping factor is 1, and wheel surface is flat. Analyzing the results, we conclude that the gap size, as in the acceleration mode, has a big influence on the value of the onset velocity observed. For the gap of 0.1 mm the onset velocity is about 50 mm/s higher than the one for the gap of 0.3 mm. Strikingly, however, the onset frequency does not change.

Summarizing, the change of the damping factor from 1 to 10 does not influence the outcome of the Rheotens constant mode. The difference in wheel surface, for a gap size of 0.3 mm, does not have a significant influence on the results either. But we would like to emphasize that the latter conclusion holds only if the gap size is 0.3 mm. Different wheel surfaces combined with other gap sizes yield different results. The size of the gap between the wheels has a clear influence on the onset velocity, but does not change the onset frequency. We notice that, even though the onset velocity might vary either slightly due to the flat/grooved surface, or significantly due to the size of the gap between the wheels, the onset frequency in all experiments remains the same; the variation of 0.01 Hz is within our error margin. We conclude that the onset frequency of draw resonance force oscillations does not depend on the operating conditions used.

Table 3.2: Evaluation of the **damping factor influence** on the results of the Rheotens constant mode with $L = 100$ mm and wheels with the flat surface. LLDPE2 is operated at 190°C and LDPE at 150°C .

Material	Gap (mm)	Damping factor	Onset velocity (mm/s)	Frequency (Hz)	Velocity mm/s	Frequency (Hz)
LLDPE2	0.1	1	410 - 420	0.52	430	0.51, 1.00, 1.50
		10	410 - 420	0.51	430	0.49, 0.98, 1.45
LDPE	0.3	1	420 - 430	0.85	420	0.85
		10	420 - 430	0.85	420	0.84

Table 3.3: Evaluation of the **wheel surface influence** on the results of the Rheotens constant mode with $L = 100$ mm, damping factor being 1, and gap between the wheels 0.3 mm. LLDPE2 is operated at 190°C and LDPE at 150°C .

Material	Wheel surface	Onset velocity (mm/s)	Frequency (Hz)	Velocity mm/s	Frequency (Hz)
LLDPE2	flat	360 - 365	0.52	380	0.48, 0.95, 1.42
	grooved	350 - 355	0.51	380	0.48, 0.95, 1.42
LDPE	flat	420 - 430	0.85	440	0.86
	grooved	430 - 440	0.86	430	0.85

Table 3.4: Evaluation of the **influence of the size of the gap between the wheels** on the results of the Rheotens constant mode with $L = 100$ mm, damping factor being 1, and wheels with the flat surface. LLDPE2 is operated at 190°C and LDPE at 150°C .

Material	Gap (mm)	Onset velocity (mm/s)	Frequency (Hz)
LLDPE2	0.1	410 - 420	0.52
	0.3	360 - 365	0.52
LDPE	0.1	470 - 480	0.86
	0.3	420 - 430	0.85

3.2.4 Difference in Materials

In this section we look at the amplitude spectra of the Rheotens response of different polymer materials and we compare their characteristic frequencies. The aim is to find a confirmation that the oscillation frequency at draw resonance can indeed be considered as a characteristic of a polymer. In all experiments considered in this section, the drawing length is 100 mm, wheels are flat with the gap 0.1 mm.

Figure 3.14 shows the amplitude spectra of the force of LLDPE 1 at different drawing velocities. The choices of $v = 400, 450,$ and 475 mm/s, correspond to stable operation; $v = 500$ mm/s corresponds to first appearance of draw resonance. Analyzing the given plots, we see that all spectra contain one distinctive peak of the same amplitude value, 140 dB, but with a frequency value changing from 3.4 to 4.2 Hz. We think that this frequency is imposed by the wheels; naturally it is changing, as the operating wheel velocity is changing. We notice also another frequency peak present in all spectra, although at first sight it might be confused with the noise. This frequency has approximately the same value in all spectra, 0.56-0.58 Hz, but the related amplitude is growing as the velocity is increasing. Finally, when the velocity reaches the onset of the draw resonance, i.e., $v = 500$ mm/s, the amplitude related to frequency 0.58 Hz becomes much higher than the amplitude of the supposedly wheel frequency of 4.2 Hz. More strikingly, at the draw resonance we also observe the harmonic complex with 0.58 Hz being its basic frequency. In the pictures related to stable operation, harmonic complexes are not clearly present yet. If the velocity is increased further above the critical level, the frequency peaks of the harmonic complex also grow, see Figure 3.15.

Next, we consider the same material, LLDPE 1, operated at a constant wheel velocity of 325 mm/s, but with a changing mass throughput, $Q = 100, 150, 200$ g/h. A change of Q yields a change of the initial velocity of the melt. Thus, even with the wheel velocity fixed, we still obtain different drawing conditions (force). In all three tests, the input conditions are at stable operation, i.e. draw resonance is not observed. The resulting spectra are given in Figure 3.16. Comparing the results of these experiments with the previous ones (see Figure 3.14), we conclude that indeed the motion of the wheels imposes a peak in the amplitude spectrum. This time the peak of higher frequency has the same value for all three experiments, namely 2.7 Hz, as in this experiment we did not change the value of wheel velocity.

Figure 3.17 shows the development of the amplitude spectrum of LLDPE 2 for a drawing velocity ranging from 100 to 440 mm/s. We observe that at lower velocities not only the harmonic complex but also the basic frequency disappears. At 300 mm/s, a basic frequency is present but with a not well pronounced amplitude. At 400 mm/s, the amplitude related to the basic frequency is quite high, but not yet higher than the peak corresponding to the wheel motion. Finally, at 420 mm/s draw resonance is observed, and it is confirmed by the spectrum, where the basic frequency peak becomes much higher than the peak correspondent to the wheel motion. Finally, at 440 mm/s, a harmonic complex related to the draw resonance is fully present.

For LLDPE materials the harmonic complex appearing at draw resonance seems to be a material

characteristic, while for LDPE material it is not. We observe this in Figure 3.18, where the spectra of LDPE are presented for $v = 460, 470, 480$ and 500 mm/s. According to the constant mode measurements, the drawing velocities 460 and 470 mm/s correspond to stable operations and the drawing velocities 480 and 500 mm/s correspond to draw resonance. At 480 mm/s, the oscillations just start and do not yet have a high amplitude, whereas at 500 mm/s, after oscillating for some time, the filament breaks. The amplitude spectra built for these velocities do indicate the presence of a basic frequency of resonance oscillations, but the related amplitude is visibly lower than the one for LLDPE material. A harmonic complex is not observed.

We summarize all the onset velocity and frequency data obtained for different materials in Table 3.5. In this Table, along with the already discussed LLDPE 1 we also present the results available for PP and PC obtained from the experiments carried out at Dow in 2005. In those experiments flat wheels were used with the default gap size, which is 0.3 mm. That is why we present here the values of the onset velocities of LLDPE 2 and LDPE also obtained for a 0.3 mm gap size. The onset frequency does not depend on the gap size between the wheels. We conclude that the velocity and frequency of the draw resonance oscillations depend on the polymer material and, therefore, can be considered a material characteristic.

Table 3.5: Velocity and frequency at onset of draw resonance oscillations for different materials. $L = 100$ mm, gap size = 0.3 mm.

Polymer	Onset velocity (mm/s)	Frequency (Hz)
LLDPE 1	500	0.58
LLDPE 2	365	0.52
LDPE	430	0.86
PP	300	0.44
PC	575	0.63

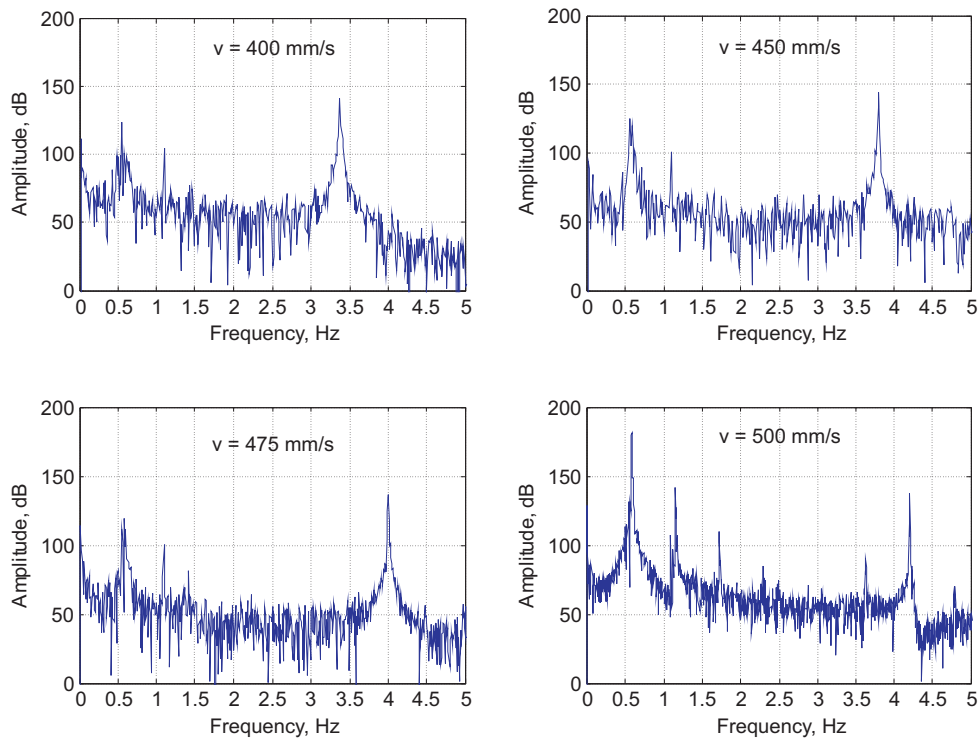


Figure 3.14: Change of amplitude spectra of force versus frequency for LLDPE 1, when the draw velocities are taken at 400, 450, 475 and 500(DR) mm/s.

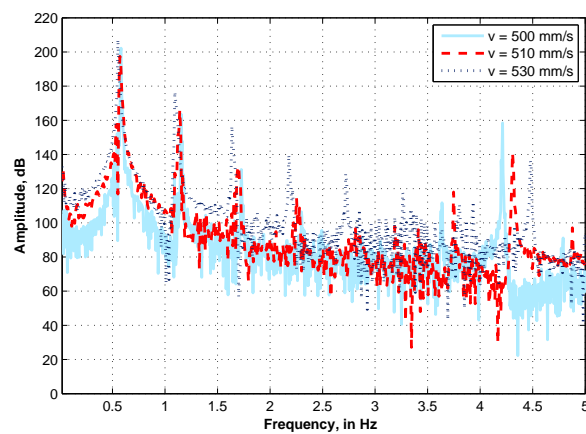


Figure 3.15: Amplitude spectra of force versus frequency for LLDPE 1, at $T = 190^{\circ}\text{C}$, $L = 100\text{ mm}$, $Q = 600\text{ g/h}$. The draw velocities are 500, 510, and 530 mm/s.

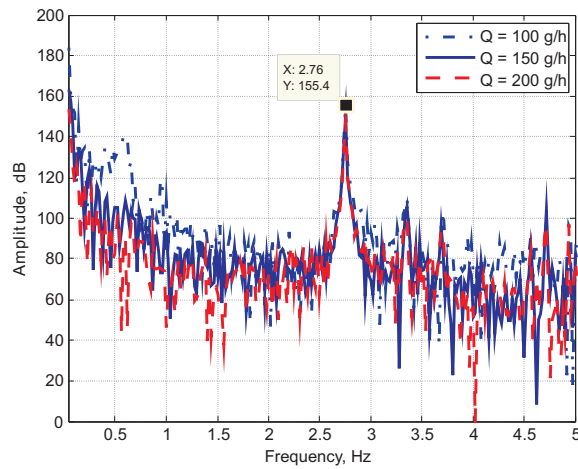


Figure 3.16: Amplitude spectra of force versus frequency for LLDPE 1, at $T = 190^{\circ}\text{C}$, $L = 100$ mm, with the smaller die, $d_{\text{die}} = 1$ mm. The draw velocity is fixed at 325 mm/s and a polymer mass throughput is changing, $Q = 100, 150$ and 200 g/h.

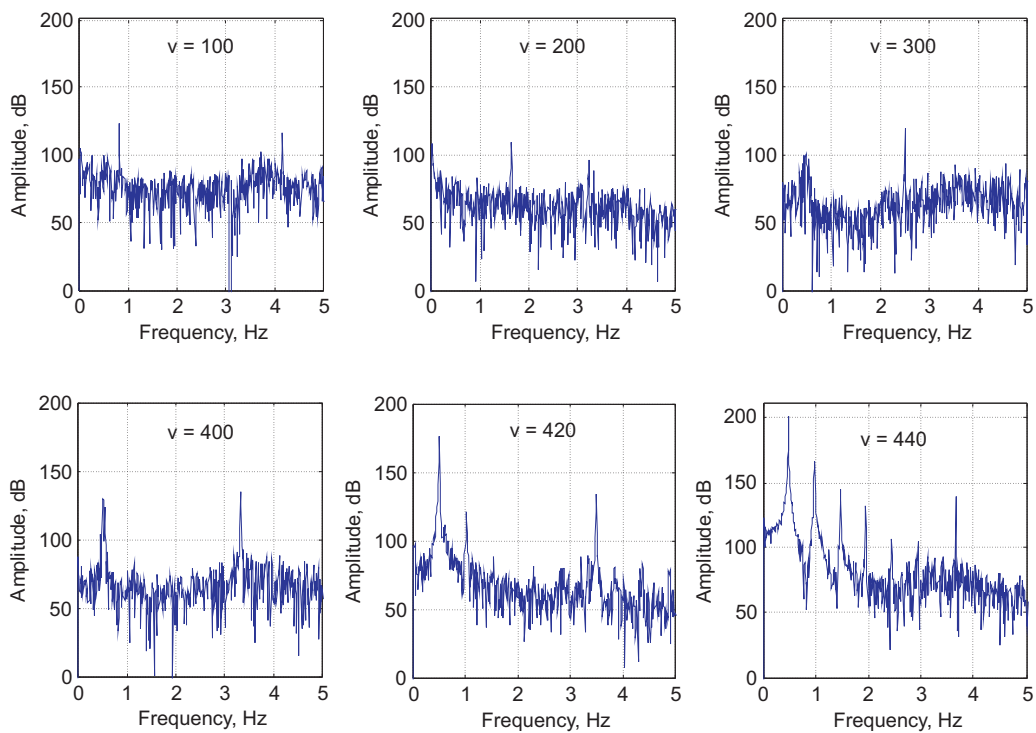


Figure 3.17: Change of amplitude spectra of force versus frequency for LLDPE 2, when the draw velocities are taken at 100, 200, 300, 400, 420(DR) and 440(DR) mm/s.

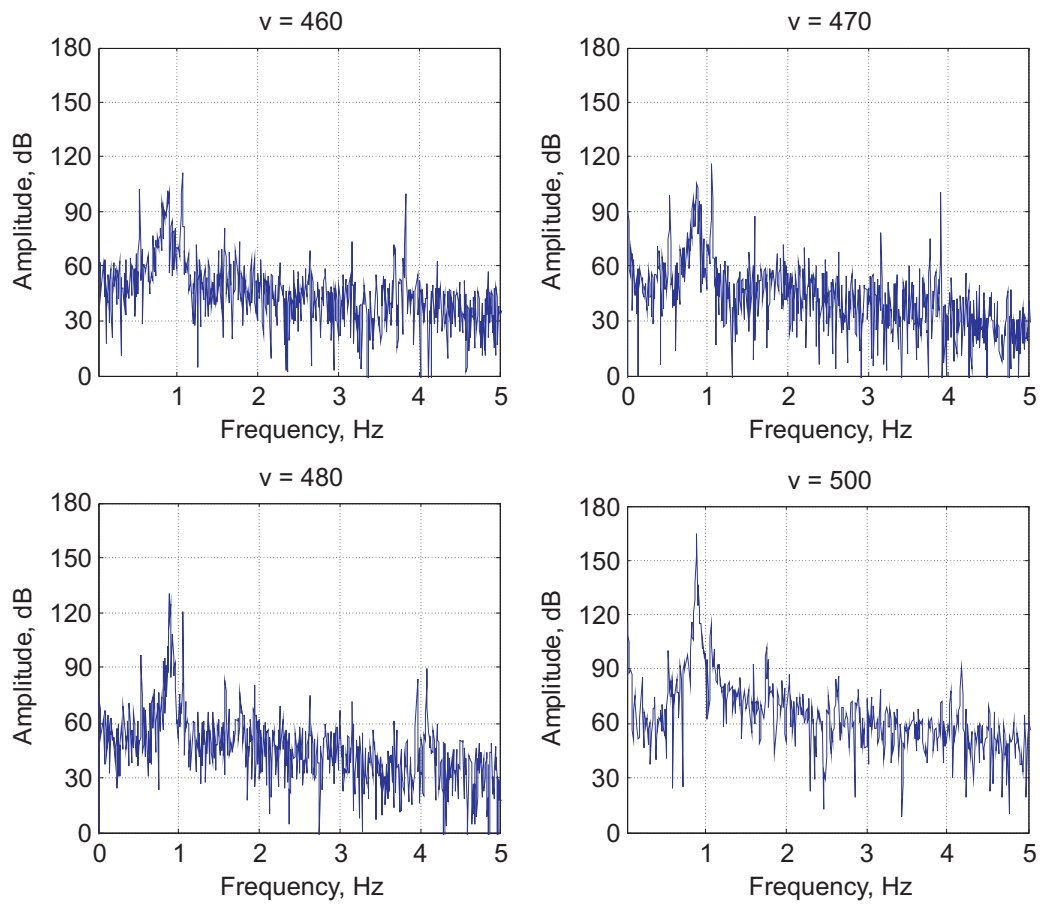


Figure 3.18: Change of amplitude spectra of force versus frequency for LDPE, when the draw velocities are taken at 460(stable), 470(stable), 480(DR) and 500(DR) mm/s. $L = 100\text{mm}$, flat wheels, $g = 0.1\text{ mm}$

3.2.5 Influence of the Drawing Length

Because in the experiments on draw resonance oscillations we deal with wave phenomena, the drawing length L has influence on the wave length and the frequency of oscillations. To check how big that influence is, we conducted several experiments with both, acceleration and constant mode. We determined the frequencies by applying the DFT. The experimental results obtained by acceleration mode are presented in Figures 3.19 and 3.20. Figure 3.19 shows Rheotens curves for LLDPE2 obtained for 4 different lengths, $L = 100, 144, 185$ and 300 mm, at an acceleration of 24 mm/s^2 . In Figure 3.20 the Rheotens curve for LDPE are present for 3 different lengths, $L = 100, 140,$ and 300 mm. The curves are obtained with an acceleration 2.4 mm/s^2 . We conclude that the longer the drawing length the higher the drawability of the polymer and the lower its melt strength.

The relationship between the drawing length L and the onset velocity and onset frequency, respectively, is shown in Table 3.6. Visually these data are represented in Figure 3.21, where the onset velocity is plotted versus the drawing length, and in Figure 3.22, where the onset frequency is plotted versus the inverse of the drawing length. Experiments indicate that onset velocity is linear with respect to length in the observation range, see Figure 3.21. An interesting result is that the slopes of the velocity vs length are the same for both materials. It seems that the slope of velocity is material independent. We do not want to draw more conclusions at the moment, experiments with other materials should confirm our observations.

The onset frequency is linear with respect to the inverse of the length, as shown in Figure 3.22. Since the offset values for both lines are 1 or 2 bin, thus within the accuracy of the experiment, we may conclude that as the length increases, the onset frequency decreases with a limiting value in zero. The slopes of the frequency lines are different, depending on the material. We conclude that the dependence of frequency on the drawing length resembles the one of the frequency of a pure string fixed at both edges.

Table 3.6: Change of the onset velocity and the onset frequency with the change of the drawing length investigated for two materials, LLDPE2 and LDPE.

Material	Length (mm)	Onset velocity (mm/s)	Frequency (Hz)
LLDPE2	100	410 - 420	0.52
	144	430 - 440	0.36
	185	470 - 480	0.29
	300	510 - 520	0.19
LDPE	100	470 - 480	0.86
	140	510 - 515	0.64
	300	580 - 590	0.30

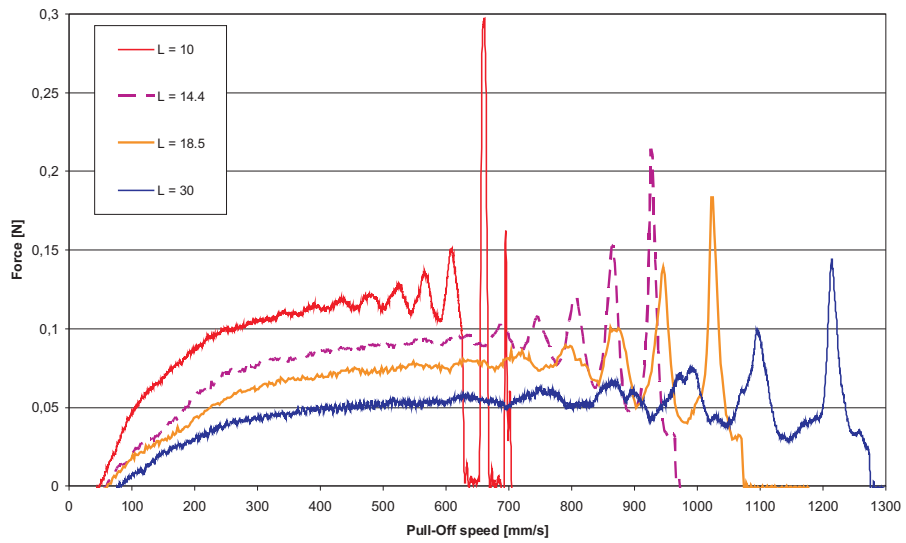


Figure 3.19: Acceleration mode, $a = 24 \text{ mm/s}^2$, flat wheels, gap = 0.1 mm. LLDPE2: $Q = 600 \text{ g/h}$, $T_{\text{extr}} = 190^\circ \text{C}$, drawing length varies.

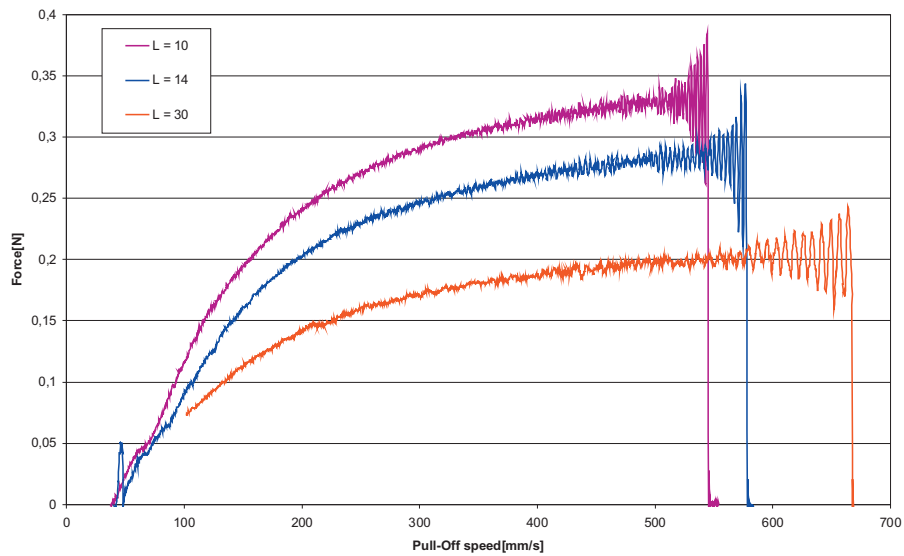


Figure 3.20: Acceleration mode, $a = 2.4 \text{ mm/s}^2$, flat wheels, gap = 0.1 mm. LDPE: $Q = 600 \text{ g/h}$, $T_{\text{extr}} = 150^\circ \text{C}$, drawing length varies.

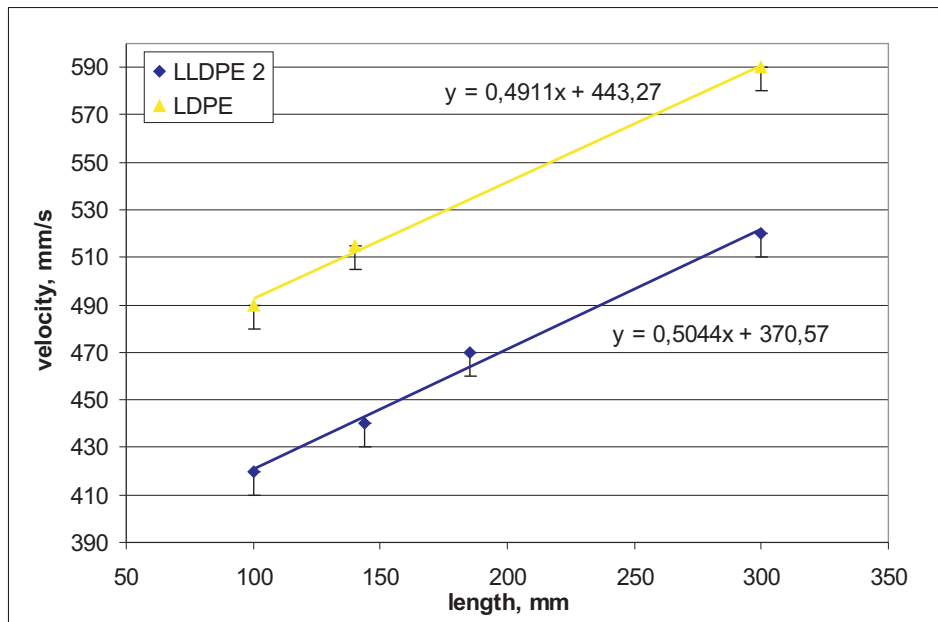


Figure 3.21: Measured onset velocity vs drawing length

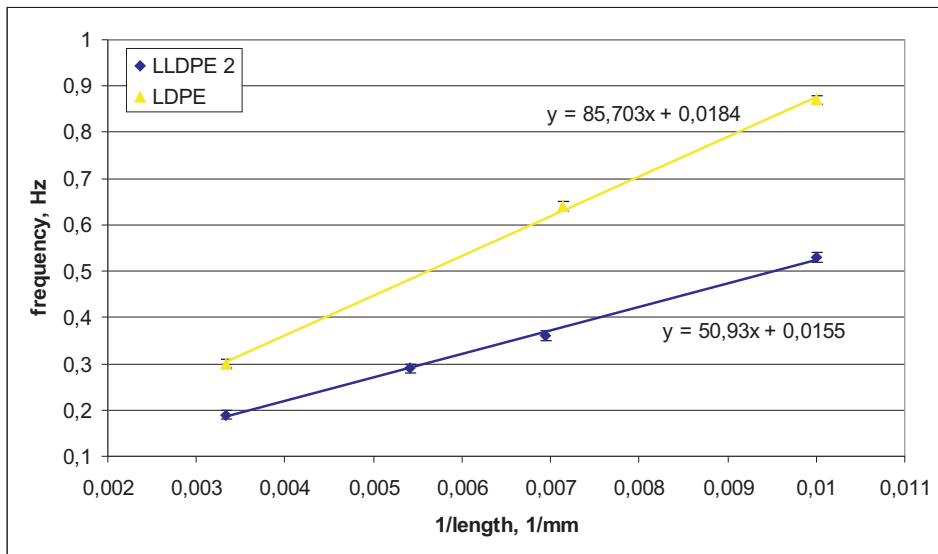


Figure 3.22: Measured frequency of oscillations vs drawing length

3.2.6 Conclusions from Experiments

Experimental data obtained from operating Rheotens at constant mode is not reported in literature, and the analysis of this data is one of the novel contributions of this thesis to material characterization. This data not only confirms the acceleration mode measurements but brings much more information: a more accurate onset velocity estimation and an accurate estimation of the frequency of oscillations, which effectively are traveling waves. Combined data from the acceleration mode and the constant mode can be used to estimate constitutive model parameters. We build a model to simulate the Rheotens constant mode experiment; it predicts the force response for a given draw velocity (for modeling see Section 3.3). With respect to that, the main conclusion from the acceleration mode experiments is that

- at low velocities, before the force reaches a plateau, the shape of the Rheotens steady state curve depends on the acceleration used in the experiment. The results obtained at low acceleration (2.4 mm/s^2) are close to the results obtained at constant operating mode. The results obtained at high acceleration (24 mm/s^2) are slightly lower than the results obtained at constant mode. This dependence of the shape of the Rheotens curve on the acceleration should be remembered when the Rheotens curve is used for fitting parameters.

The main conclusions from the constant mode experiments are that:

- the peak height in the amplitude spectrum at the resonance frequency is material dependent.
- the frequency at draw resonance does not depend on the gap size; it also does not depend on the wheel surface, for a gap size of 0.3 mm.
- the onset velocity of draw resonance depends on the gap size. The onset velocity obtained for gap size of 0.1 mm is about 50 mm/s higher than the one obtained for a gap size of 0.3 mm.
- the frequency at draw resonance depends on the kind of material and is, therefore, a material characteristic.
- the frequency at draw resonance is linearly related to the inverse of the drawing length, with zero offset.
- the onset velocity is linearly related with the drawing length, where the slope seems to be material independent and the offset - material dependent.
- for LLDPE a harmonic complex develops at draw resonance.

All conclusions imply that any mathematical model of the Rheotens experiment should contain material and process parameters that distinguish the different materials and process conditions.

3.3 Mathematical Modeling

3.3.1 Configuration and Assumptions

The flow domain of the polymer is described by cylindrical coordinates (r, θ, z) , as indicated in Figure 3.23. The origin of the coordinate system is taken at the point of maximal swell. Thus, the initial radius R_0 of the fiber is the radius at maximal swell, $R_0 = R_{swell}$ ³. The flow is assumed to be rotationally symmetric, i.e., independent of θ . The change of radius of the filament is quantified

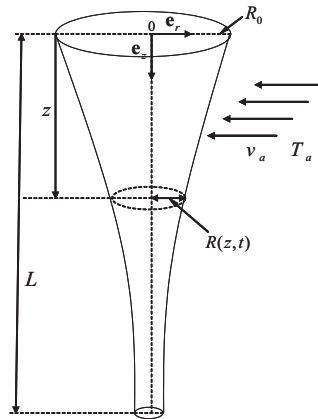


Figure 3.23: Configuration of the polymer flow domain in Rheotens experiment

by the function $R(z, t)$. The thickness of the fiber, given by the radius, even in its highest value is in the order of 10^{-2} smaller than its length. Thus, the fiber is approximated by a slender filament. The polymer flow is assumed to be incompressible, i.e., the density ρ does not change with the temperature and, thus, mass throughput Q [kg/h] is conserved. The initial velocity of the flow, u_0 , depends on the mass throughput Q and on the initial radius R_0 ,

$$u_0 = \frac{Q}{\rho \pi R_0^2}. \quad (3.3)$$

The velocity of the fiber at the pulling wheels is u_f . The ratio between the initial and final velocities is called Draw ratio ($Dr = \frac{u_f}{u_0}$). It is an important dimensionless parameter that actually specifies the drawing force. The velocity field of the polymer flow is

$$\mathbf{u} = u_r \mathbf{e}_r + u_z \mathbf{e}_z. \quad (3.4)$$

The polymer flow field is considered to be in elongation direction mainly. Thus, the velocity component in the extension direction is assumed to be uniform over the cross-section,

$$u_z = u_z(z, t). \quad (3.5)$$

The forces acting in the process on a filament segment are drawing force, gravity, inertia, air drag, and surface tension. All of them are considered in the modeling, except for the surface tension

³One can always neglect extrudate swell by taking $R_0 = R_{die}$.

since it is relatively small with respect to drawing force. The stress tensor is denoted by σ . We consider the normal stresses introduced in the filament by σ_{rr} , $\sigma_{\theta\theta}$, and σ_{zz} . The normal stress at the fiber surface is zero, $\sigma_{rr}(z, R, t) = 0$. Due to the slender filament approximation, the latter statement is replaced by

$$\sigma_{rr}(z, r, t) = 0. \quad (3.6)$$

Because diffusion of heat in the considered process is much slower than convection of heat, we consider the temperature averaged over the cross-section. Thus, the temperature profile in the length direction is specified by the function $T(z, t)$. The temperature dependence of polymer characteristics, such as viscosity η and relaxation time λ , is assumed to be reflected by an Arrhenius law.

This way, the fundamental unknowns of our problem are the velocity $\mathbf{u}(r, z, t)$, the radius of the filament $R(z, t)$, the temperature of the filament $T(z, t)$, and the normal stress $\sigma_{zz}(z, r, t)$, with the independent variables r , z , and t .

3.3.2 Equations

For a given process configuration, with all introduced assumptions and unknowns, the system of governing equations consists of conservation of mass, momentum, and energy, and polymer constitutive equations, which are presented in this section.

Conservation of Mass

The mass in the fiber must be conserved,

$$\frac{\partial}{\partial t}(\rho A) + \frac{\partial}{\partial z}(\rho A u_z) = 0. \quad (3.7)$$

Here A denotes the area of a cross-section, $A = \pi R^2$, and ρ - the density of the polymer. The polymer fluid of the fiber is assumed to be incompressible. This implies that ρ is constant and uniform, $\rho(z, t) = \rho$, which in turn yields

$$\frac{\partial R}{\partial t} + u_z \frac{\partial R}{\partial z} + \frac{R}{2} \frac{\partial u_z}{\partial z} = 0. \quad (3.8)$$

Air Drag Effect

At the surface of the fiber $r = R(z, t)$, we have the following condition for the stresses due to the air friction

$$\mathbf{n} = \tau \mathbf{s}, \quad (3.9)$$

where \mathbf{n} and \mathbf{s} are the normal and the tangential unit vectors along the filament, and τ expresses the amount of air friction. The normal and the tangential vectors at the surface of the fiber obey

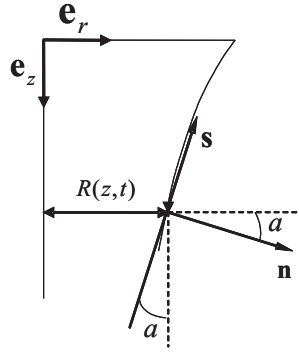


Figure 3.24: 2-D geometry expressing the boundary conditions at the fiber surface

the following expressions (see Fig.3.24)

$$\mathbf{n} = \cos \alpha \mathbf{e}_r + \sin \alpha \mathbf{e}_z, \quad (3.10)$$

$$\mathbf{s} = \sin \alpha \mathbf{e}_r - \cos \alpha \mathbf{e}_z, \quad (3.11)$$

where the small angle $\alpha = \alpha(z, t)$ is defined by

$$\tan \alpha = -\frac{\partial R}{\partial z}. \quad (3.12)$$

With this we get from the z - component of (3.9)

$$\sigma_{rz} \cos \alpha + \sigma_{zz} \sin \alpha = -\tau \cos \alpha. \quad (3.13)$$

Dividing (3.13) by $\cos \alpha$ and using (3.12), we get

$$\sigma_{rz} = \sigma_{zz} \frac{\partial R}{\partial z} - \tau. \quad (3.14)$$

After Matsui [59], Gould and Smith [60], it is common to use for air friction the following relation

$$\tau = C_f \rho_a u_z^2, \quad (3.15)$$

where ρ_a is the air density, and C_f is the dimensionless air drag coefficient, which is expressed via Reynolds number for the air

$$C_f = 0.205 \text{Re}_a^{-0.61} = 0.205 \left(\frac{\rho_a u_z R}{\eta_a} \right)^{-0.61}. \quad (3.16)$$

Equation of Motion

The equation of motion takes in our case the following quasi-static form

$$\rho L \mathbf{v} = \text{div} \boldsymbol{\sigma}^T + \rho \mathbf{b}. \quad (3.17)$$

We consider only the most important component of that equation, namely the last one,

$$\rho u_z \frac{\partial u_z}{\partial z} = \frac{\partial \sigma_{zz}}{\partial z} + \frac{1}{r} \sigma_{rz} + \rho g. \quad (3.18)$$

By integrating this equation over the cross-section, we obtain

$$\pi R^2 \rho u_z \frac{\partial u_z}{\partial z} = \pi R^2 \frac{\partial \sigma_{zz}}{\partial z} + 2\pi R \sigma_{rz} + \pi R^2 \rho g. \quad (3.19)$$

The left hand side term of (3.19) presents inertia, the last term on the right hand side presents gravity. By substituting (3.14) and (3.15) into (3.19), and making a simple transformation, we get

$$\rho R^2 u_z \frac{\partial u_z}{\partial z} = \frac{\partial}{\partial z} (R^2 \sigma_{zz}) - 2C_f \rho_a R u_z^2 + \rho g R^2. \quad (3.20)$$

Temperature Evolution Equation

Generally, in accordance with our assumptions the temperature evolution in the fiber is given by the following quasi-static equation

$$\rho C_p u_z \frac{\partial T}{\partial z} = -\frac{2h_c}{R} (T - T_a) + \sigma_{zz} \frac{\partial u_z}{\partial z}, \quad (3.21)$$

where C_p ($\frac{J}{kgK}$) is the heat capacity of the polymer, which is assumed to depend linearly on the temperature of the polymer according to

$$C_p = 969.9 + 3.7T. \quad (3.22)$$

The first term on the right hand side of (3.21) presents the heat transfer between the fiber and the surrounding air due to the forced convection of the air. Here the convective heat transfer coefficient h_c takes the form

$$h_c = 0.21 \frac{k_a}{R} (Re_a)^{1/3}, \quad (3.23)$$

with air heat conductivity k_a , and Reynolds number for the air $Re_{air} = \left(\frac{\rho_a u_z R}{\eta_a} \right)^{-0.61}$.

The second term on the right hand side of (3.21) is the viscous heat dissipation.

Constitutive Equations

Here we first give the general expressions that are valid for any constitutive model applied to the Rheotens experiment, and then go to the particular examples of a Newtonian and a modified Giesekus model. For any constitutive model, the total stress tensor σ is given by

$$\sigma = -p\mathcal{I} + \mathcal{T}, \quad (3.24)$$

where $p = p(z, t)$ is the pressure, and \mathcal{T} is the extra-stress tensor, satisfying $tr\mathcal{T} = 0$. From the assumption about the zero normal stress at the fiber surface (3.6), we deduce the pressure

$$\sigma_{rr} = -p + \tau_{rr} = 0 \Rightarrow p = \tau_{rr}. \quad (3.25)$$

Any constitutive model contains the gradient of the velocity field, $\mathcal{L} = \text{grad}\mathbf{v}$. The incompressibility assumption, $\text{div}\mathbf{v} = 0$, yields the following relation for the velocity component u_r in terms of u_z

$$u_r = -\frac{r}{2} \frac{\partial u_z}{\partial z}. \quad (3.26)$$

The polymer flow is strongly elongational, meaning that the diagonal terms of the tensor \mathcal{L} dominate the off-diagonal ones. Now, using the expression (3.26) and neglecting the off-diagonal terms, we write the velocity gradient tensor \mathcal{L} as

$$\mathcal{L} = \begin{pmatrix} \frac{\partial u_r}{\partial r} & 0 & \frac{\partial u_r}{\partial z} \\ 0 & \frac{1}{r}u_r & 0 \\ \frac{\partial u_z}{\partial r} & 0 & \frac{\partial u_z}{\partial z} \end{pmatrix} \simeq \begin{pmatrix} -\frac{1}{2} \frac{\partial u_z}{\partial z} & 0 & 0 \\ 0 & -\frac{1}{2} \frac{\partial u_z}{\partial z} & 0 \\ 0 & 0 & \frac{\partial u_z}{\partial z} \end{pmatrix}. \quad (3.27)$$

Also further we use λ to denote the characteristic relaxation time of a polymer (as we consider only one mode models); η to denote the viscosity of a polymer. The temperature dependence of both, λ and η , is assumed to be covered by Arrhenius law,

$$\lambda(T) = \lambda_0 \exp\left[\frac{E_a}{RT_0} \left(\frac{T_0}{T} - 1\right)\right], \quad (3.28)$$

$$\eta(T) = \eta_0 \exp\left[\frac{E_a}{RT_0} \left(\frac{T_0}{T} - 1\right)\right], \quad (3.29)$$

where E_a is the activation energy of the polymer, T_0 - reference temperature that we take as extrusion temperature, R - the universal gas constant, λ_0 and η_0 are the values of the relaxation time and the viscosity at the extrusion temperature T_0 : $\lambda_0 = \lambda(T_0)$, $\eta_0 = \eta(T_0)$.

• Newtonian Constitutive Equations

For a Newtonian incompressible fluid, the extra-stress tensor satisfies a simple relation

$$\mathcal{T} = 2\eta\mathcal{D}, \quad (3.30)$$

where the polymer viscosity η is temperature dependent. The rate-of-deformation tensor \mathcal{D} is defined as

$$\mathcal{D} = \frac{1}{2}(\mathcal{L} + \mathcal{L}^T). \quad (3.31)$$

Substituting (3.30) into (3.24), and using relation (3.25) afterwards, we find that $\sigma_{\theta\theta} = 0$, and the only remaining equation is the one for σ_{zz} ,

$$\sigma_{zz} = 3\eta \frac{\partial u_z}{\partial z}. \quad (3.32)$$

• Modified Giesekus Constitutive Equations

Expressing a polymer rheological behavior with the modified Giesekus constitutive equations, we follow *Doufas et al.* [61]. We express the extra-stress tensor, and so the stress

tensor, in terms of conformation tensor \mathcal{C} (components c_{ij}). The conformation tensor is proposed to characterize the microstructure, i.e. molecular orientation and stretching, of a melt. The relation between the extra-stress tensor and the conformation tensor is

$$\mathcal{T} = nk_B T \left(\frac{3}{N_0 l^2} EC - \mathcal{I} \right). \quad (3.33)$$

The polymer melt exiting the die is modeled as a concentrated suspension of non-linear elastic dumbbell molecules. Each molecular chain is assumed to contain N_0 flexible statistical links of length l . In (3.33), n is the number of molecules per unit volume, and k_b is the Boltzmann constant. The quantity E , the non-linear spring force factor accounting for a finite chain extensibility, is approximated by *Cohen* [62] with the following expression

$$E = \frac{3N_0^2 l^2 - \text{tr}\mathcal{C}}{3N_0^2 l^2 - 3\text{tr}\mathcal{C}}. \quad (3.34)$$

Now, substituting (3.33) into (3.24), and using (3.25), we find also an expression of σ_{zz} in terms of the conformation tensor,

$$\sigma_{zz} = \frac{3nk_B T}{N_0 l^2} E (c_{zz} - c_{rr}). \quad (3.35)$$

We use this expression of σ_{zz} in the equation of motion (3.20) and the equation of temperature evolution (3.21) when considering the modified Giesekus constitutive model.

Finally, the evolution equation for the conformation tensor \mathcal{C} is

$$\frac{D\mathcal{C}}{Dt} = -\frac{1}{\lambda} \frac{k_b T}{K_0} \left((1 - \alpha)\mathcal{I} + \alpha \frac{K_0}{k_b T} EC \right) \left(\frac{K_0}{k_b T} EC - \mathcal{I} \right). \quad (3.36)$$

Here α is a modified Giesekus model parameter representing molecular mobility. The upper convective derivative $\frac{D}{Dt}$ is in general form defined by

$$\frac{D^*}{Dt} = \frac{\partial^*}{\partial t} + (\mathbf{v}, \frac{\partial}{\partial \mathbf{x}})^* - \mathcal{L}^* - {}^* \mathcal{L}^T. \quad (3.37)$$

With (3.37) and \mathcal{L} given by (3.27), and with component $c_{\theta\theta}$ excluded (as we assume $c_{\theta\theta} = c_{rr}$), the evolution equation of conformation tensor (3.36) in components reads

$$\lambda \left(\frac{\partial c_{rr}}{\partial t} + u_z \frac{\partial c_{rr}}{\partial z} + c_{rr} \frac{\partial u_z}{\partial z} \right) = \frac{N_0 l^2}{3} \left((1 - \alpha) + \alpha \frac{3}{N_0 l^2} E c_{rr} \right) \left(1 - \frac{3}{N_0 l^2} E c_{rr} \right), \quad (3.38)$$

$$\lambda \left(\frac{\partial c_{zz}}{\partial t} + u_z \frac{\partial c_{zz}}{\partial z} - 2c_{zz} \frac{\partial u_z}{\partial z} \right) = \frac{N_0 l^2}{3} \left((1 - \alpha) + \alpha \frac{3}{N_0 l^2} E c_{zz} \right) \left(\frac{3}{1 - N_0 l^2} E c_{zz} \right). \quad (3.39)$$

3.3.3 Boundary Conditions

In the previous subsection we derived the governing system of equations for the small scale fiber spinning process represented by the Rheotens experiment. We recall that this system of governing equations consists of

- (3.8), (3.20), (3.21), and (3.32) with unknowns $R(z, t)$, $u_z(z, t)$, $T(z, t)$, and $\sigma_{zz}(z, t)$ for the Newtonian fluid;
- (3.8), (3.20), (3.21), (3.38), and (3.39) with unknowns $R(z, t)$, $u_z(z, t)$, $T(z, t)$, $c_{rr}(z, t)$ and $c_{zz}(z, t)$ for the modified Giesekus fluid.

For a complete problem descriptions boundary conditions need to be added. From the process conditions, we deduce the following obvious boundary conditions at $z = 0$ and $z = L$:

$$u_z(0, t) = u_0, \quad R(0, t) = R_0, \quad T(0, t) = T_{extr}, \quad u_z(L, t) = u_f. \quad (3.40)$$

In case of the Newtonian model, the number of conditions are enough. In case of the modified Giesekus model, we additionally need one more boundary condition. We assume that the polymeric fluid in the point of the highest swell is in nearly equilibrium state. Thus, we take the boundary value of c_{rr} at the equilibrium value, keeping in mind that all extra stresses are relaxed at equilibrium,

$$c_{rr}(0, t) = c_{rr}^{eq} = \frac{N_0 l^2}{3E_{eq}}. \quad (3.41)$$

The value of $E_{eq} = E(c_{ii}^{eq})$ is found by substituting (3.41) in (3.34) and then solving the quadratic equation with respect to E_{eq}

$$E_{eq} = \frac{1 + N_0}{2N_0} + \frac{\sqrt{9 + 6N_0 + 9N_0^2}}{6N_0}. \quad (3.42)$$

3.3.4 Scaling

To have a simpler form of governing equations, and also to better identify which parameters have the most influence on the solution stability, we apply a dimensionless form of the system. For that, the following dimensionless variables are used:

$$\hat{z} = \frac{z}{L}; \quad \hat{u} = \frac{u}{u_0}; \quad \hat{R} = \frac{R}{R_0}; \quad \hat{T} = \frac{T}{T_0}; \quad \hat{t} = \frac{u_0}{L}t; \quad (3.43)$$

In the Newtonian formulation of the problem, the stress component is naturally scaled according to

$$\hat{\sigma}_{zz} = \frac{\sigma_{zz}}{\sigma_{zz}^0}, \quad (3.44)$$

where the value σ_{zz}^0 represents the initial value of the stress factor at the point $z = 0$. In the modified Giesekus formulation of the problem, the components of the conformation tensor become dimensionless via

$$\hat{c}_{ii} = \frac{c_{ii}}{N_0 l^2 / 3}, \quad (3.45)$$

and the stress component σ_{zz} is now scaled according to

$$\hat{\sigma}_{zz} = \frac{\sigma_{zz}}{G_0}, \quad (3.46)$$

where G_0 is the shear modulus at the initial temperature, $G_0 = \frac{\eta(T_0)}{\lambda(T_0)}$.

3.3.5 Dimensionless Systems

Grouping and Notations

In our representation of the scaled systems, for convenience, hats are omitted and the following dimensionless groups are introduced:

$$W = \frac{u_0}{\sigma_{zz}^0 L}, \quad (3.47)$$

$$K_1 = \frac{\rho u_0^2}{\sigma_{zz}^0}, \quad (3.48)$$

$$K_2 = \frac{L}{u_0^2} g, \quad (3.49)$$

$$K_3(u_z, R) = 2C_f \frac{\rho_a L}{\rho R_0} = 0.21 \frac{\rho_a L}{\rho R_0} \left(\frac{\rho_a u_0 R_0 u_z R}{\eta_a} \right)^{-0.61}, \quad (3.50)$$

$$V_1 = \frac{0.42 L k_a}{\rho u_0^{2/3} R_0^{5/3}} \left(\frac{\rho_a}{\eta_a} \right)^{1/3}, \quad (3.51)$$

$$V_2 = \frac{\sigma_{zz}^0}{\rho T_0}, \quad (3.52)$$

$$V_3 = \frac{G_0}{\rho T_0}, \quad (3.53)$$

$$C_1 = \frac{\rho u_0^2}{G_0}, \quad (3.54)$$

$$C_2 = \frac{2C_f \rho_a L u_0^2}{G_0 R_0}, \quad (3.55)$$

$$C_3 = \frac{\rho g L}{G_0}. \quad (3.56)$$

The non-linear force factor E and its derivative are in the dimensionless form given by

$$E(C) = \frac{9N_0 - 2c_{rr} - c_{zz}}{9N_0 - 6c_{rr} - 3c_{zz}}, \quad (3.57)$$

$$\frac{\partial E}{\partial z}(C) = \frac{18N_0}{(9N_0 - 6c_{rr} - 3c_{zz})^2}. \quad (3.58)$$

The heat capacity C_p has the following representation in the new variables

$$C_p(T) = a + bT_0 T. \quad (3.59)$$

The important dimensionless processing parameters are the draw ratio Dr , representing the ratio between the final and initial velocity of the filament, and the Deborah number $De(T)$, representing the ratio of relaxation time and process time,

$$Dr = \frac{u_f}{u_0}; \quad De(T) = \frac{\lambda(T)u_0}{L}.$$

We also use the notation De_0 for Deborah number at initial temperature, $De_0 = \lambda_0 u_0 / L$.

Dimensionless System for a Newtonian Fluid

With the above introduced grouping and notations, the system characterizing the non-isothermal Rheotens experiment for the case of the Newtonian fluid takes the form

$$\sigma_{zz} = 3\eta W \frac{\partial u_z}{\partial z}, \quad (3.60)$$

$$\frac{\partial R}{\partial t} + u_z \frac{\partial R}{\partial z} + \frac{R}{2} \frac{\partial u_z}{\partial z} = 0, \quad (3.61)$$

$$2\sigma_{zz} \frac{\partial R}{\partial z} + R \frac{\partial \sigma_{zz}}{\partial z} = K_1 \left(R u_z \frac{\partial u_z}{\partial z} - K_2 R + K_3 (u_z, R) u_z^2 \right), \quad (3.62)$$

$$\frac{\partial T}{\partial z} = -V_1 \frac{1}{C_p(T) u_z^{2/3} R^{5/3}} \left(T - \frac{T_a}{T_0} \right) + V_2 \frac{\sigma_{zz}}{C_p(T) u_z} \frac{\partial u_z}{\partial z}, \quad (3.63)$$

where $0 < z < 1$ and $t > 0$. Dimensionless boundary conditions are

$$u_z(0, t) = 1, \quad R(0, t) = 1, \quad T(0, t) = 1, \quad u_z(1, t) = Dr. \quad (3.64)$$

Dimensionless System for a Modified Giesekus Fluid

The system characterizing the non-isothermal Rheotens experiment for the case of the modified Giesekus constitutive model takes the form

$$\frac{\partial c_{rr}}{\partial t} + u_z \frac{\partial c_{rr}}{\partial z} + c_{rr} \frac{\partial u_z}{\partial z} = -\frac{T}{De(T)} \left((1 - \alpha) + \alpha \frac{E(\mathcal{C})c_{rr}}{T} \right) \left(\frac{E(\mathcal{C})c_{rr}}{T} - 1 \right), \quad (3.65)$$

$$\frac{\partial c_{zz}}{\partial t} + u_z \frac{\partial c_{zz}}{\partial z} - 2c_{zz} \frac{\partial u_z}{\partial z} = -\frac{T}{De(T)} \left((1 - \alpha) + \alpha \frac{E(\mathcal{C})c_{zz}}{T} \right) \left(\frac{E(\mathcal{C})c_{zz}}{T} - 1 \right), \quad (3.66)$$

$$\frac{\partial R}{\partial t} + u_z \frac{\partial R}{\partial z} + \frac{R}{2} \frac{\partial u_z}{\partial z} = 0, \quad (3.67)$$

$$\begin{aligned} & \frac{2E(\mathcal{C})(c_{zz} - c_{rr})}{R} \frac{\partial R}{\partial z} + \left(2 \frac{\partial E}{\partial z} (c_{zz} - c_{rr}) - E(\mathcal{C}) \right) \frac{\partial c_{rr}}{\partial z} + \\ & \left(\frac{\partial E}{\partial z} (c_{zz} - c_{rr}) + E(\mathcal{C}) \right) \frac{\partial c_{zz}}{\partial z} - C_1 u_z \frac{\partial u_z}{\partial z} - C_2 \frac{u_z^2}{R} + C_3 = 0, \end{aligned} \quad (3.68)$$

$$\frac{\partial T}{\partial z} = -V_1 \frac{1}{C_p(T) u_z^{2/3} R^{5/3}} \left(T - \frac{T_a}{T_0} \right) + V_3 \frac{E(\mathcal{C})(c_{zz} - c_{rr})}{C_p(T) u_z} \frac{\partial u_z}{\partial z}, \quad (3.69)$$

where $0 < z < 1$ and $t > 0$. The boundary conditions are

$$u_z(0, t) = 1, \quad R(0, t) = 1, \quad T(0, t) = 1, \quad u_z(1, t) = Dr, \quad c_{rr}(0, t) = \frac{1}{E_{eq}}, \quad (3.70)$$

where E_{eq} is given by (3.42).

3.3.6 General Formulation

After scaling, the model of fiber spinning results in a quasi-linear system of differential equations with two point boundary conditions. Its general form can be written as given in Chapter 2,

$$\begin{aligned} \mathcal{C}(\mathbf{y}) \frac{\partial \mathbf{y}}{\partial t} &= \mathcal{A}(\mathbf{y}) \frac{\partial \mathbf{y}}{\partial z} + \mathbf{b}(\mathbf{y}), \quad 0 < z < 1, t > 0. \\ P(\mathbf{y}(0, t)) &= \xi, \quad Q(\mathbf{y}(1, t)) = \zeta. \end{aligned}$$

In this formulation z and t are independent variables; $\mathbf{y}(z, t)$ is a vector function consisting of all the state variables in the dynamic autonomous system:

$\mathbf{y} = (u_z, R, \sigma_{zz}, T)$ for the Newtonian model;

$\mathbf{y} = (u_z, R, c_{rr}, c_{zz}, T)$ for the modified Gieskus model.

Connection between Numerical and Experimental Data

The ultimate goal of the development of the mathematical model is to simulate the results of the Rheotens experiment in order to find the constitutive model parameters. Having established these parameters we can use them in the simulations of other industrial polymer processes. The experimental results that we use for parameter estimation are the steady state Rheotens curve, the onset velocity and frequency at draw resonance. In order to compare the simulation results with the steady state Rheotens curve, we have to establish such a curve from our mathematical model. To do this, we compute the steady state solution $\mathbf{y}_{steady}(x)$ for several drawing velocities from the system of the form

$$\mathcal{A}(\mathbf{y}_{steady}) \frac{\partial \mathbf{y}_{steady}}{\partial z} + \mathbf{b}(\mathbf{y}_{steady}) = \mathbf{0}, \quad 0 < z < 1,$$

completed with the inhomogeneous 2-point boundary conditions. In the calculation of the steady state, a shooting method combined with a fourth order Runge-Kutta scheme is used. As a result we obtain the steady state velocity, radius, and stress profile in a filament for each given drawing velocity. From the calculated stress we recalculate the force at each drawing velocity, so we can compare the computed force with the force measured by the Rheotens experiment and presented by the Rheotens curve. This is the procedure to obtain numerically a "force vs velocity" curve for one given set of model parameters. We also developed a program where the simulation procedure mentioned is repeated a certain number of times, depending on the convergence of the optimization routine. In each iteration step the model parameters are changed until the simulated curve differs slightly from the experimental curve. In this search for optimal parameters that yield the best fit between the simulated and experimental curve, we use particle swarm optimization (PSO), which is a stochastic, population based technique developed by *Kennedy and Eberhart*, [63], in 1995.⁴

⁴Although relatively new, PSO has been applied to a variety of tasks and has evolved greatly since the original version; for more information see www.swarmintelligence.org or *Kennedy and Eberhart* [64].

To find the onset velocity and frequency, we linearize the initial system around the steady solution by introducing $\mathbf{y}(z, t) = \mathbf{y}_{steady}(z) + \mathbf{y}_{pert}(z, t)$, where we look for the perturbations \mathbf{y}_{pert} that satisfy $\mathbf{y}_{pert}(z, t) = \tilde{\mathbf{y}}(z) \exp \gamma t$. The temperature is not taken as a component of \mathbf{y}_{pert} because of its quasi-static nature. As explained in Chapter 2, the result of the linearization is a generalized eigenvalue problem that yields a set of complex characteristic values $\{\gamma\}$, which we call the spectrum. Once the spectrum is known, the stability/instability of the steady state solution is determined according to the following criterium:

$$\begin{aligned} \text{if } \forall \gamma \quad \text{Re}(\gamma) < 0 &\Rightarrow \text{the calculated steady state is stable,} \\ \text{if } \exists \gamma \quad \text{Re}(\gamma) > 0 &\Rightarrow \text{the calculated steady state is unstable.} \end{aligned}$$

To calculate the spectrum $\{\gamma\}$ we use the numerical routine explained in detail in Chapter 2, Section 2.3. To find the onset velocity of draw resonance for a specified set of model parameters, we calculate the spectrum for a number of drawing velocities, starting from relatively small values and moving upward with a step of 10 mm/s. The drawing velocity for which the spectrum contains a critical point, γ_{crit} , with a positive real part is then defined as the onset velocity. The imaginary part of γ_{crit} determines the frequency of draw resonance oscillations according to

$$f_{crit} = \frac{u_0}{L} \left[\frac{\text{Im}(\gamma_{crit})}{2\pi} \right]. \quad (3.71)$$

The calculated onset velocity and onset frequency for one particular set of model parameters are then compared to the experimentally measured ones. If the calculated values are not sufficiently close to the measured values of the onset velocity and frequency, we tune the model parameters and repeat the calculation procedure.

3.4 Simulations: Newtonian Model

In this section we present the results of the Newtonian model. The Newtonian model is the simplest constitutive model. The only material parameter it contains is viscosity. Apart from viscosity, in this section we also discuss the initial diameter of the filament, which is a process parameter, and its influence on the simulation results. This way we hope to clarify our choices of viscosity and initial diameter, when we work with the more enhanced rheological models, like the modified Giesekus model.

3.4.1 Remarks about Viscosity

Viscosity is the only polymer characteristic present in the Newtonian model. In our simulations, we do not use a zero-shear viscosity, as in common practice, but we rather choose the value of viscosity at shear rate $\dot{\gamma} = 1 \text{ s}^{-1}$. On one hand, using the ANSYS[®] POLYFLOW^{®5} simulations carried out

⁵ANSYS, ANSYS Workbench, AUTODYN, CFX, FLUENT and any and all ANSYS, Inc. brand, product, service and feature names, logos and slogans are registered trademarks or trademarks of ANSYS, Inc. or its subsidiaries in the United States or other countries. All other brand, product, service and feature names or trademarks are the property of their respective owners.

at Dow [65], we found that a shear rate of 1 s^{-1} is more realistic for the average share rate at the extrudate swell. On the other hand, running our stability simulations, we found that the value of viscosity does not have a significant influence on the prediction of draw resonance. Viscosity does indicate the level of the drawing force at steady state (see Figure 3.25), but prediction for the onset velocity for these choices of viscosity remains the same.

Qualitatively the Newtonian model gives a well predicted Rheotens curve, quantitatively it does not, for whatever value of the viscosity. But, obviously, with the viscosity at $\dot{\gamma} = 1 \text{ s}^{-1}$ the predicted Rheotens curve gives a much better indication of the real values of the drawing force than the curve predicted with the zero-shear viscosity. If we try to fit sophisticated models with two or more parameters on the Rheotens curve, it is good to eliminate at least one of the parameters before hand.

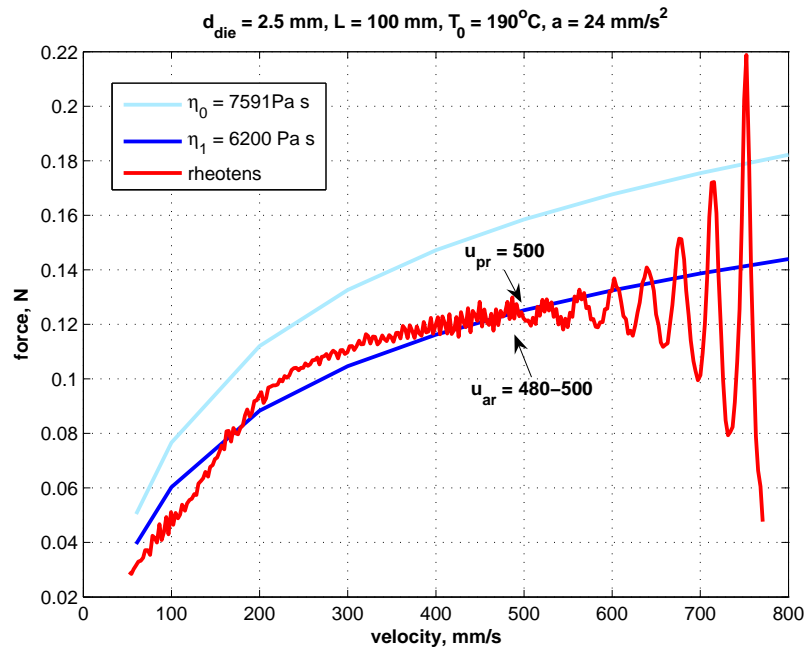


Figure 3.25: *Dependence of the fitted curve on the viscosity values: the upper curve was found for $\eta = 7591 \text{ Pa}\cdot\text{s}$, the lower curve for $\eta = 6200 \text{ Pa}\cdot\text{s}$. The Rheotens curve presents the LLDPE 1 experiment for the conditions: $d_{\text{die}} = 2.5 \text{ mm}$, $L = 100 \text{ mm}$, $T = 190^\circ\text{C}$, $Q = 600 \text{ g/h}$, $\rho = 762 \text{ kg/m}^3$*

3.4.2 Influence of Extrudate Swell

It is common practice to ignore extrudate swell when simulating models of the fiber spinning process, even when a small scale process like the Rheotens test is considered. We think that neglect of extrudate swell is not necessarily a correct assumption. Thus, in this section we discuss the relevance of the choice of the initial diameter for the draw resonance predictions. We base our discussion on the Newtonian model results. For the simulations we choose the experiment with LLDPE 1 with an extrusion temperature of 190°C , since for this experiment the actual onset

velocity u_{ar} and frequency of transversal oscillations were measured accurately.

We run the simulations, keeping all operating conditions the same, only changing the value of the initial diameter. Results are given in Table 3.7. The first row represents the value of the initial diameter used in numerical simulations. The first value chosen is the die diameter with no swell, the diameter of 2.5 mm. The last value chosen is the value measured with a laser system in the following way: the polymer extruded through the die was allowed to fall freely; the radius of the resulting filament was measured at the end of the spin line. The second row in the table indicates how much the chosen value of the initial diameter is larger than the die diameter, in percentage. The third row gives the values of the initial velocity that significantly changes with the change of the initial diameter. Next, the predicted onset velocity is given for each value of the initial diameter. The last row indicates the critical Draw ratio Dr .

The change of the initial diameter yields a significant change of initial velocity of the flow because this velocity depends on the initial diameter d_0 , on the mass throughput Q , and on the density ρ :

$$u_0 = \frac{4Q}{\rho\pi d_0^2}.$$

Because the mass throughput Q is kept constant and the fluid is assumed incompressible, thus, the density is constant⁶, the only factor that remains in play is the diameter.

Thus, the initial velocity is influenced by extrudate swell. The critical Draw ratio, however, is about the same, $Dr \in (20, 21)$, for all tested conditions. Therefore, the onset velocity of draw resonance changes with the change of the radius. The higher the extrudate swell is, meaning the higher the initial diameter, the lower the initial velocity of the flow is and thus the lower the onset velocity of draw resonance. With the extrudate swell neglected, the onset velocity of draw resonance is about 910 mm/s, which is completely unrealistic.

Table 3.7: Influence of extrudate swell on draw resonance: LLDPE, $T = 190^\circ\text{C}$, $Q = 600 \text{ g/h}$, $L = 100 \text{ mm}$, $\rho = 762 \text{ kg/m}^3$, $d_{die} = 2.5 \text{ mm}$, $u_{ar} = 480 - 500 \text{ mm/s}$

d_0 (mm)	2.5 (die)	3.3	3.4	3.5	3.63 (value of swell measured after 100 mm)
swell (%)	0	32	35	40	45
u_0 (mm/s)	44.56	25.57	24.09	22.73	21.13
u_{pr} (mm/s)	910	530	500	480	440
Dr	20.42	20.73	20.76	21.11	20.82

The results presented prove that the value chosen for the initial diameter of the fiber is an important factor in the prediction of stability. Thus, if we want to have a reliable stability prediction, we cannot neglect extrudate swell. We do not regard the above described procedure to measure extrudate swell as completely satisfactory for the following reasons: the diameter of the filament is measured after 100 mm and the real swelling, if any, takes place in a few millimeters from the die

⁶Even if we do not assume incompressibility, the change of temperature on a short distance of few millimeters near the die is insignificant, and thus density does not change either.

exit; besides, the pulling motion of the wheels obviously has a decreasing influence on extrudate swell. Also, as poor as the measurements of extrudate swell might be, they are simply not available for all experiments we are analyzing. Therefore, we decided to consider the initial diameter as an additional fitting parameter when interpreting the results of the Rheotens experiment with the results of numerical simulations.

3.5 Simulations: the Modified Giesekus Model

The goal of our research on the Rheotens experiment is to establish a method to estimate constitutive model parameters from the experimental results. We achieve this goal by considering two types of experimental results: the steady state Rheotens curve and onset velocity and frequency of oscillations. We simulate this data with the modified Giesekus model. The two parameters of this model are α ($0 < \alpha < 1$) and N_0 ($N_0 > 0$), which characterize the flexibility and the average number of links in the molecular chain, respectively. However, α and N_0 are not the only unknown material parameters that we have to deal with in the simulations. Others are the viscosity of the polymer melt η , the relaxation time λ (keep in mind that the model we use has only one mode, i.e. one relaxation time), and the initial diameter of a filament d_0 , which is supposed to be taken at the highest swell. In literature, the fiber spinning models usually suggest to take a zero-shear viscosity as input and neglect extrudate swell. In this way *Doufas* [61] attempted to find the constitutive model parameters from the Rheotens steady state curve; fitting the relaxation time λ along with α and N_0 . Our simulations of the Newtonian model, however, suggest that a zero-shear value for viscosity as well as a die diameter value instead of an initial diameter might not necessarily be the best choice (see Sections 3.4.1 and 3.4.2).

With five parameters at hand, we found that if we consider only the steady state Rheotens curve obtained from the acceleration mode, we can find several different parameter settings that fit the curve equally well, see Figure 3.26, where two different settings are presented. In other words, any optimization procedure, in which the parameters at every step are adjusted in order to fit the Rheotens curve will result into an infinite number of solutions. Therefore we decided to extend the procedure of parameter determination with additional experimental results obtained with the Rheotens constant mode, namely: the onset velocity and onset frequency at draw resonance oscillations. Before we start to describe the fitting procedure, in the following subsection we carry out a sensitivity analysis. In this analysis we determine if and how the frequency and the onset velocity depend on parameters α , N_0 , d_0 , λ , and η .

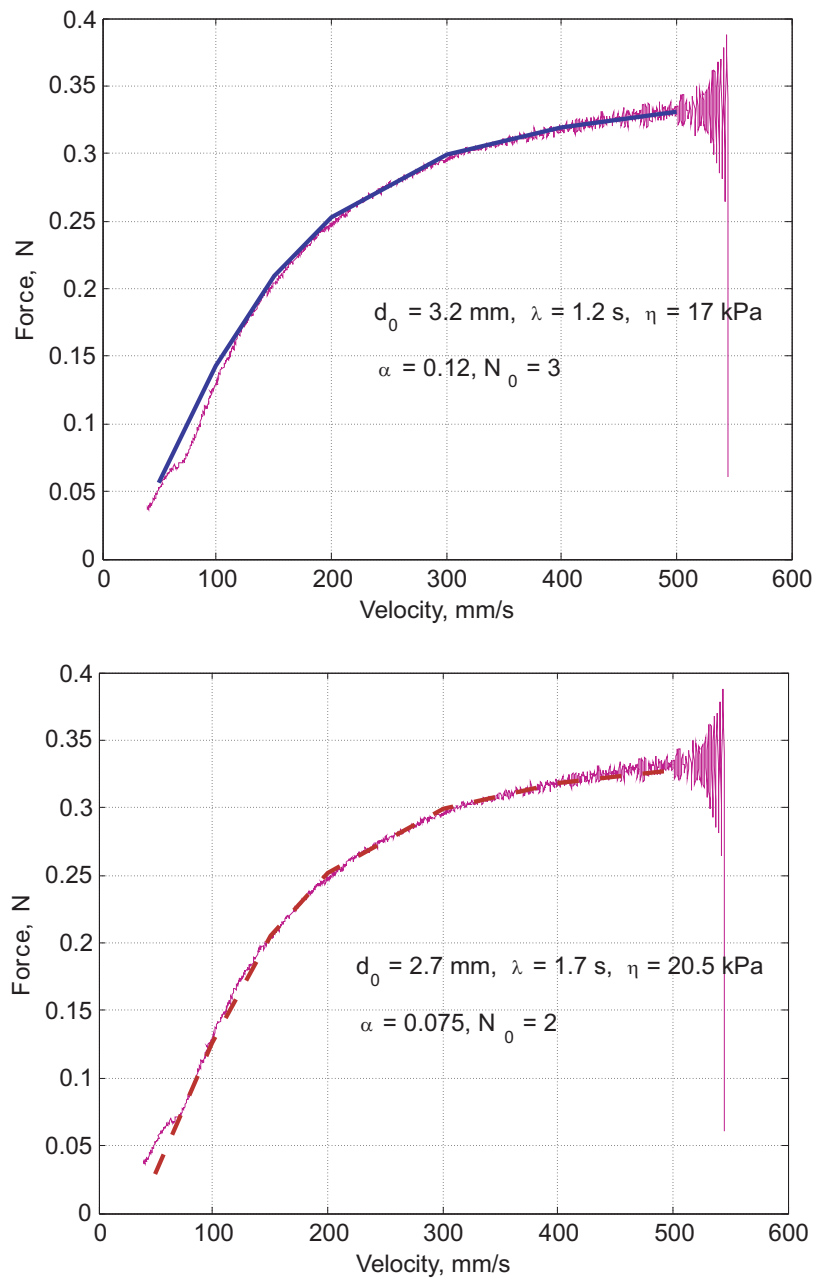


Figure 3.26: Numerical simulations: example of the fit of the Rheotens steady state curve found with 2 different sets of parameters. The experimental curve is obtained for LDPE with a drawing length of 100 mm.

3.5.1 Sensitivity Analysis

In this section we investigate the influence that the parameters of our model have on the resulting frequency and onset velocity. For that, as a basis, we take the experimental conditions of LDPE, meaning that the extrusion temperature is 150 °C, activation energy is 57.7 kJ/mol, density is 781.5 kg/m³, mass throughput is 0.6 kg/h, drawing length is 100 mm, and the die diameter is $d_{die} = 2,5$ mm. In every numerical simulation, we keep all parameters fixed except the parameter under investigation; that parameter we vary within a given range and for each of its values we calculate the onset critical velocity and for a fixed velocity of 480 mm/s we calculate the frequency. In our numerical calculations the velocity step size is 10 mm/s, so that a reported predicted onset velocity of 450 mm/s means that the previous one, 440 mm/s, leads to a stable solution, when 450 mm/s does not.

To be able to estimate whether the sensitivity of the results to a change in parameters is significant, we recall that the frequency bin size in the experiments conducted with LDPE is 0.009 Hz. We also recall that, in contrast to the onset frequency, the onset velocity depends slightly on the gap size between the wheels. As we do not consider a final condition on filament radius in our model, which would be determined by the gap size, we do not know if the results of our model are closer to the experiments with a gap size of 0.1 mm or with a gap size of 0.3 mm. That is why for the onset velocity we consider a wider bin size, namely, instead of the initial experimental step size of 10 mm/s, we consider 50 mm/s, which is the difference between the experimental onset velocities obtained with 0.1 mm and 0.3 mm gap.

Influence of Viscosity

The plot of a viscosity *versus* shear rate for LDPE at 150°C is given in Appendix B1. From the plot we see that viscosity ranges from approximately 1 kPa·s to about 70 kPa·s, with an estimated zero-shear value of 95 kPa·s. We vary the viscosity in the specified range, while keeping the other parameters fixed, $d_0 = 2.5$ mm, $\lambda = 0.08$ s, $\alpha = 0.1$, $N_0 = 10$. The results of simulations are presented in the graphs of Figure 3.27. The left hand side graph shows how the frequency at 480 mm/s changes with the change of viscosity and the right hand side graph shows the same with respect to the onset velocity. Minding the scale of the frequency vs viscosity plot, we see that influence of the viscosity on frequency prediction is very small. The frequency changes mainly when the viscosity is very low, 1-10 kPa; such low values are unlikely to fit the force level in the Rheotens curve of LDPE. But even if they do, the maximum frequency variation is 0.02 Hz, when the frequency drops from 1.002 Hz to 0.982 Hz. In the experiments the frequency bin size is 0.009 Hz; thus, the difference of about 2 bins (0.02 Hz) is negligible. With respect to the onset velocity, the change of 10 mm/s over the whole range of tested viscosities falls within one bin size, as we consider a bin size of 50 mm/s. Thus, we conclude that viscosity influences neither the prediction of frequency nor the onset velocity.

Influence of the Modified Giesekus Model Parameters α and N_0

The sensitivity of frequency and onset velocity with respect to change in the modified Giesekus model parameters α and N_0 is visualized in the graphs of Figure 3.28. We recall that $\alpha \in (0, 1)$ and $N_0 \in (0, \infty)$. It turns out that N_0 does not influence the predicted frequency value at all. We observe a slight change of frequency for $N_0 < 5$, but this difference is far less than 2 bin sizes for all test cases. For $N_0 > 5$, the frequency remains the same if all other conditions are not changed. The influence of the parameter α on frequency is larger and increasing α from 0.01 to 0.9 gives a difference of approximately 0.127 Hz, which is about 14 bin sizes.

A change in parameter α does not lead to a significant change in onset velocity, as one can see from the graph on the right hand side of Figure 3.28. For α -values varying from 0 to 1, the onset velocity remains almost the same. It changes only slightly, mainly for the smaller α -values, $\alpha < 0.3$. This change varies from 10 to 30 mm/s depending on the choice of N_0 . But the largest difference of 30 mm/s is still far within 1 velocity bin size. A change in parameter N_0 influences the calculated onset velocity, especially when N_0 is between 2 and 10; for N_0 between 10 and 100, the difference in the onset velocity is only 20 mm/s, which is within a bin size.

Influence of the Initial Diameter

Figure 3.29 shows the sensitivity of the calculated frequency (top diagram) and the calculated onset velocity (bottom diagram) to the change of initial diameter d_0 . Each plot contains 4 graphs obtained for 4 different settings of α and N_0 . The frequency decreases to almost half its value, when the diameter increases from 2.5 mm to 3.8 mm. Even more, in terms of influence on the resulting frequency, a change in diameter by only 0.2 mm has the same effect as the change in α over its whole range, from 0.01 to 0.9. The parameter N_0 does not influence the frequency, as discussed in the previous section. Thus, the overall influence of the initial diameter on frequency is much more significant than the influence of the parameter α . Similarly to the frequency, the calculated onset velocity is sensitive for the initial diameter. As can be seen in the plot at a right hand side of Figure 3.29, increasing the initial diameter from 2.5 mm to 3.8 mm yields the decrease of the onset velocity on average by 200 mm/s.

Influence of the Relaxation Time

The sensitivity of the numerical results, frequency and onset velocity, to a change in relaxation time is shown in Figure 3.30. We consider the relaxation time λ ranging from 0.01 to 5 seconds. In the plots, these values are shown in a logarithmical scale for better visualization. We observe that both frequency and onset velocity are strongly influenced by λ ; although the influence of λ on onset velocity seems to be more significant than on frequency. The frequency is not uniquely determined by λ : the same value of frequency is obtained for two and in some cases even three different values of λ . In contrast, the onset velocity is only determined by one value of the relaxation time.

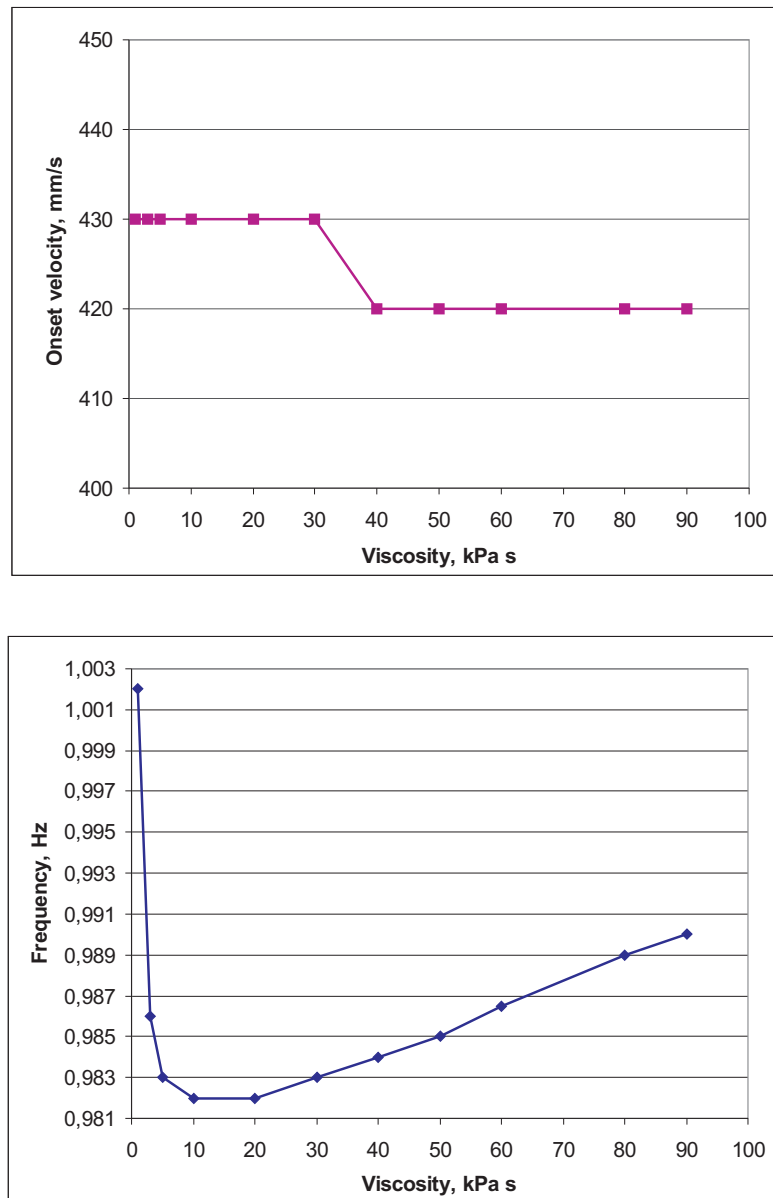


Figure 3.27: Numerical simulations: sensitivity of frequency (top) and onset velocity (bottom) to a change in viscosity. The input conditions are taken according to the experiment with LDPE using a drawing length of 100 mm. The frequency is calculated for the velocity of 480 mm/s. Other parameters are kept fixed: $d_0 = 2.5$ mm, $\lambda = 0.08$ s, $\alpha = 0.1$, $N_0 = 10$. The frequency vs viscosity plot is zoomed-in, thus mind the scale.

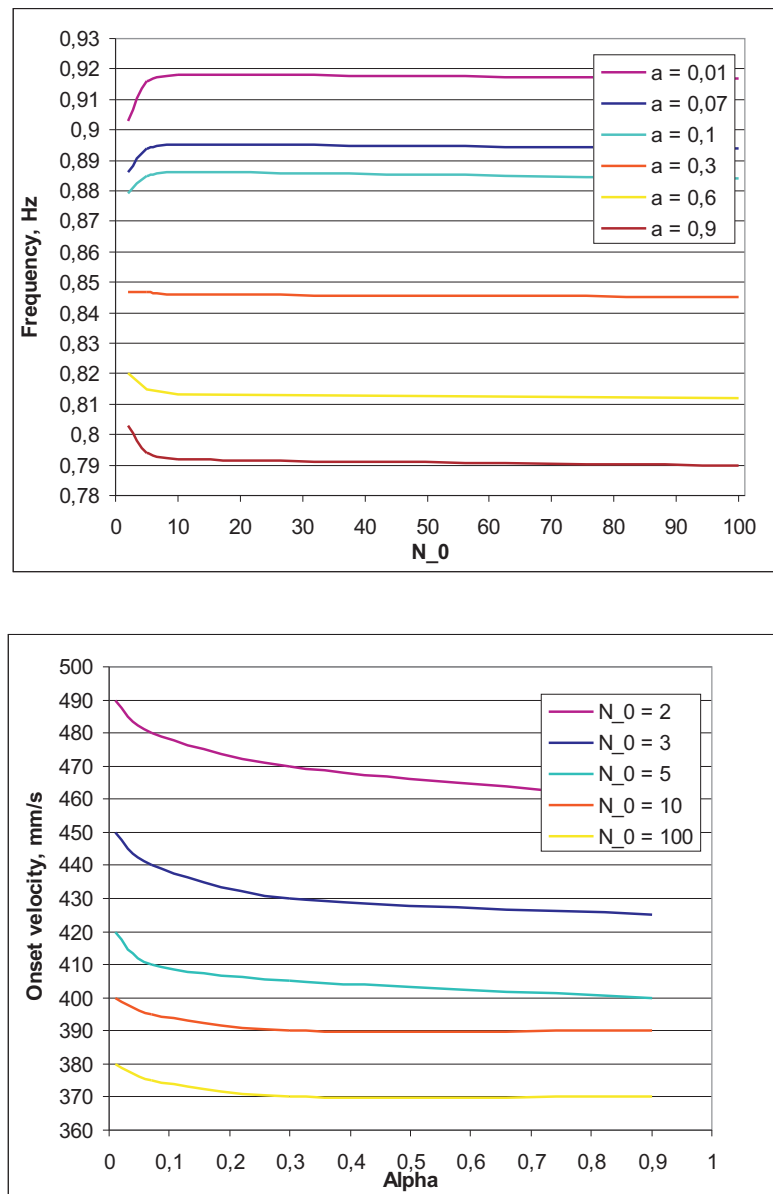


Figure 3.28: Numerical simulations: sensitivity of frequency (top) and onset velocity (bottom) to a change in the parameters α and N_0 . The input conditions are taken according to the experiment with LDPE using a drawing length of 100 mm. The frequency is calculated for the velocity of 480 mm/s. Other parameters are kept fixed: $d_0 = 2.7$ mm, $\lambda = 0.08$ s, $\eta = 22$ kPa s.

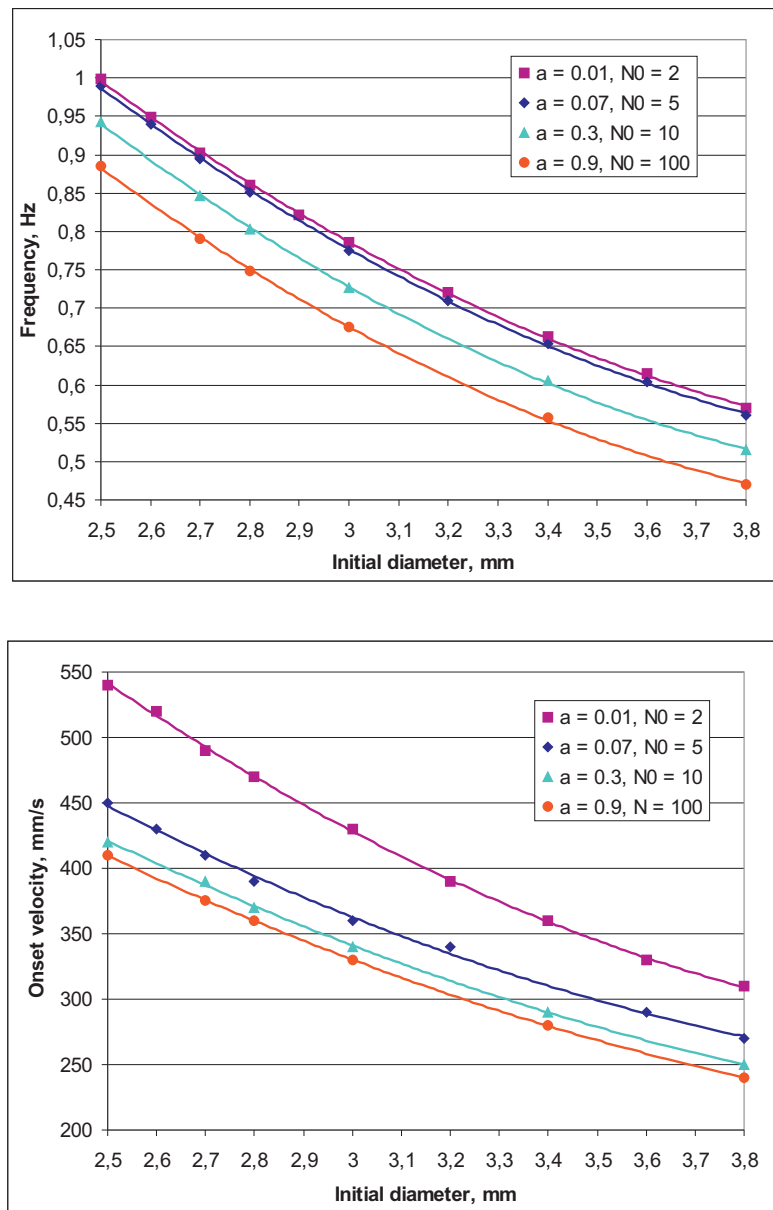


Figure 3.29: Numerical simulations: sensitivity of frequency (top) and onset velocity (bottom) to a change in initial diameter d_0 . The results are calculated for a few different sets of α and N_0 . The input conditions are taken according to the experiment with LDPE using a drawing length of 100 mm. The frequency is calculated for the velocity of 480 mm/s. Other parameters are: $\lambda = 0.08$ s, $\eta = 22$ kPa s.

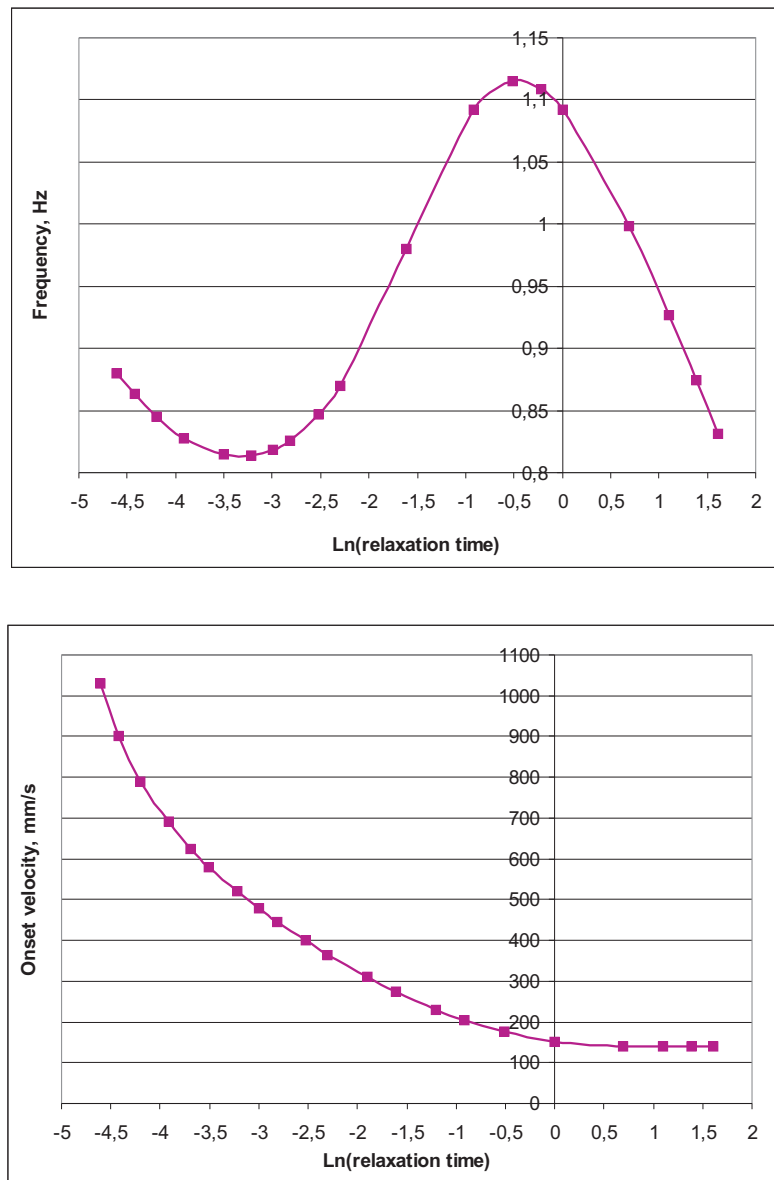


Figure 3.30: Numerical simulations: sensitivity of frequency (top) and onset velocity (bottom) to a change in relaxation time λ . The horizontal axis is in ln-scale; the relaxation times tested vary from 0.01 to 5 s. The input conditions are taken according to the experiment with LDPE using a drawing length of 100 mm. The frequency is calculated for the velocity of 480 mm/s. Other parameters are: $d_0 = 2.7$ mm, $\eta = 22$ kPa s, $\alpha = 0.3$, and $N_0 = 5$.

3.5.2 Parameter Estimation

Procedure

As we showed in the sensibility analysis discussed in the previous subsections, the initial diameter and the relaxation time are the most important parameters in terms of their influence on calculated frequency and onset velocity. Parameter N_0 has no influence on frequency and only a slight influence on the onset velocity; α does not influence the onset velocity but has a slight influence on the frequency. Based on these observations we design a scheme by which we can estimate the materials and process parameters, including the parameters of the modified Giesekus constitutive model. First, we go after a value of the initial diameter that is supposed to be taken at the point of highest swell. For each fixed value of d_0 , starting from 2.5 mm and moving up with a step of 0.1 mm, we consider 2 limiting settings of a pair (α, N_0) ; here we take (0.01, 2) and (0.9, 100). For both sets we find the value of the relaxation time, further referred to as λ_1 , that leads to a correct prediction of the onset velocity of draw resonance; we record also the correspondent onset frequency. This simple numerical experiment yields the range of onset frequencies that can be obtained for each given d_0 . The difference between the maximum and the minimum possible onset frequency is not large; this difference is determined by α , thus is not more than 0.13 Hz, as we demonstrated in Subsection 3.5.1. Such an evaluation allows us to estimate the initial diameter d_0 up to ± 0.1 mm, by comparing the calculated range of onset frequencies to the measured value of the onset frequency. Thus, we bring d_0 down to three values which differ by 0.1 mm. For each of these three values of d_0 , we calculate λ_1 and the corresponding onset frequency for a few more wisely chosen sets of (α, N_0) . This allows to determine roughly the range of the parameters α and N_0 , again by making a correspondence between the calculated onset frequency and the measured one. We notice that for different values of d_0 the estimated regions of α and N_0 do not overlap. With this information at hand, we proceed with simulations of the Rheotens steady state curve; the optimization procedure takes a reasonably short time to run, since we have limited the region in the parameter space to be explored. In fitting the Rheotens curve, the value of the viscosity becomes important, as it influences the resulting force. According to the conclusions drawn from the Newtonian model simulations, we choose the viscosity according to shear rates between 0 and 1, but rather in the vicinity of 1 per second. We found that whatever values of the other parameters we take, it proves impossible to get a good fit of the Rheotens curve using the relaxation time value of λ_1 , which is in the order of 10^{-2} . Therefore, to fit the Rheotens curve, we introduce a second mode with a second relaxation time, further called λ_2 . We usually take λ_2 coupled with the viscosity, meaning that λ_2 is the inverse of the shear rate at which the viscosity value is chosen. Therefore λ_2 is in the order of 1, which is much higher than the value of λ_1 . Thus, in order to predict both, the steady state and the oscillations characteristics accurately, we need two different modes of λ . This makes λ the unique Hopf bifurcation parameter that switches between two states of the physical system describing a process: the steady state and the oscillations about the steady state.⁷

⁷For bifurcation theory see *Marsden and McCracken* [66], *Strogatz* [67], *Kuznetsov* [68]. Application of bifurcation theory to oscillations in polymer elongation processes is considered by *Demay* [69].

Finally, in order to avoid ending up with more than one set of estimated parameters, which is possible as demonstrated in Figure 3.26, and which can not be prevented using the procedure described above, we suggest the following approach. When performing the Rheotens experiment for further use in parameter estimation, one should perform measurements at constant and acceleration mode with the same material for at least two different drawing lengths. Then, the analysis of the experimental onset frequencies compared to the calculated ones allows to specify the initial diameter d_0 taken at a swell region precisely. Moreover, from this frequency analysis the values of α and N_0 can be estimated accurately. In this case, it is not necessary any longer to fit the Rheotens steady state curve, although we still suggest to do that, either for validation or for higher precision of estimated parameters, or for both of these reasons. The suggested procedure does require to obtain the experimental data for two drawing lengths, which increases the time of performing the actual Rheotens experiments. However, this procedure yields the highly desired result, namely the unique set of parameters (for a given material at a given temperature). Moreover, it makes the analysis simple and fast.

Results

In this section we present the parameter estimation results for LDPE, LLDPE1, PP, and PS. The input values for the simulations performed for these materials are given in Table 3.8. In the same table we find the estimated values of the modified Giesekus constitutive model parameters α and N_0 , as well as two relaxation time modes λ_1 and λ_2 that specify the oscillatory and stationary states of the system, respectively.

Table 3.8: Process and polymer experimental conditions for LDPE, LLDPE1, PP, and PS. The second part of the Table contains the estimated values of the relaxation time and the modified Giesekus model parameters.

	LDPE			LLDPE1	PP	PS
T_{extr} ($^{\circ}\text{C}$)	150			190	220	220
T_{air} ($^{\circ}\text{C}$)	20			20	20	20
Q (kg/h)	0.6			0.6	0.6	0.6
ρ (kg/m ³)	781.5			760	748.5	957
E_a (kJ/mol)	57.7			34.5	41.4	114.1
L (mm)	100	140	300	100	100	50
d_{die} (mm)	2.5			2.5	2.5	2.5
d_0 (mm)	2.7			3.6	4.0	3.8
λ_1 (s)	0.007	0.075	0.095	0.024	0.060	0.009
λ_2 (s)	1.5	2	4	1	2.8	1.4
η (kPa·s)	18.5	22	32	6	33.6	7.6
α	0.105			0.19	0.31	0.29
N_0	3			5	3	14

For LDPE we have experimental data obtained for 3 different drawing lengths, $L = 100, 140,$ and 300 mm for both the constant and the acceleration mode. The analysis of the onset velocities and frequencies, as described in Section 3.5.2, yields the a value of the initial diameter of 2.7 mm, and following values for the modified Giesekus model parameters: $\alpha = 0.105, N_0 = 3$. The quality of the fit between the experimental and calculated onset velocity and frequency may be seen in Table 3.9. We observe that the relaxation time mode λ_1 is increasing linearly with the increase in drawing length. To validate the established model parameters, we also fitted the Rheotens steady state curves obtained with the acceleration mode for the same three drawing lengths. The result of this fitting is given in Figure 3.31.⁸ We observe a perfect fit between the experimental and the simulated curves. Similar to λ_1 , the value of λ_2 is increasing linearly as drawing length is increasing.

For the materials LLDPE1, PP, and PS we do not have the measurements of frequency and onset velocity for different drawing lengths. Thus, in order to establish the model parameters we have to rely on both, velocity-frequency analysis and the fit of the steady state Rheotens curve. The best fit between the simulated and the experimental onset velocity and frequency data obtained from the Rheotens constant mode is presented in Table 3.9. The best fit between the simulated and the experimental Rheotens curves is presented in Figure 3.32.

Table 3.9: Critical velocity at onset of draw resonance and frequency of force oscillations: comparison of experimentally measured values (exp) with the simulated ones (sim). In experiments with LDPE the frequency bin size is 0.0046 Hz; for LLDPE1 the frequency bin size is 0.0046 Hz, for PP it is 0.05 Hz, and for PS it is 0.009 Hz.

Material	Drawing length L (mm)	Relaxation time λ_1 (s)	Onset velocity (mm/s)		Frequency (Hz)	
			exp	sim	exp	sim
LDPE	100	0.07	430 - 480	450-460	0.86	0.85
	140	0.075	470 - 515	510-520	0.64	0.63
	300	0.095	540 - 590	580-590	0.30	0.30
LLDPE1	100	0.024	475 - 500	470-480	0.58	0.59
PP	100	0.06	290 - 300	300-310	0.44	0.44
PS	50	0.009	400 - 425	420-430	1.15	1.17

Finally, we also consider the Rheotens experiment where LLDPE1 is used at different temperatures. The results of the fitting of simulation data to experimental curves are presented in Figure 3.33. We do not have precise measurements of the onset velocity or frequency of oscillations for this experiment, thus, the results of the fitting should be considered carefully. We notice, however, that the fitting results are consistent and indicative for the dependence of the model parameters on temperature. The model parameters obtained by the best fit are decreasing as temperature increases.

⁸All experimental curves considered in this section are corrected for the influence of gravity according to [61].

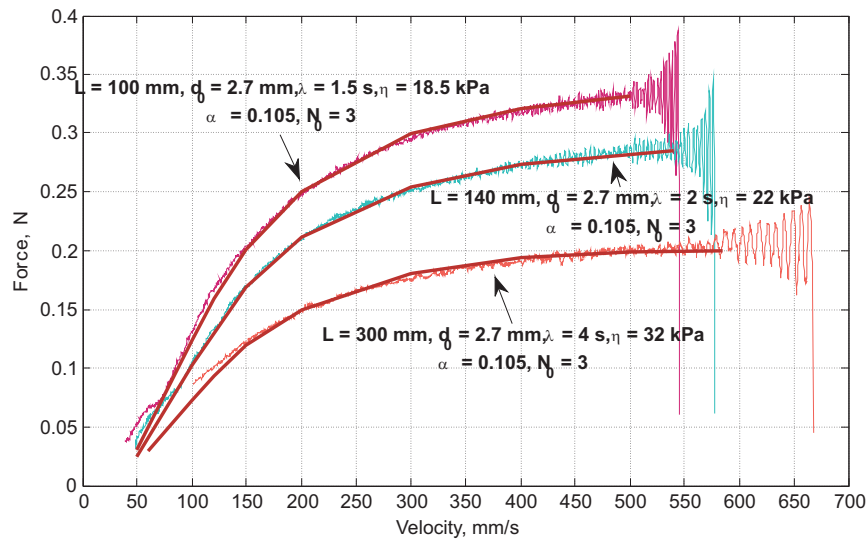


Figure 3.31: Demonstration of the Rheotens curves fitted under the steady state conditions for LDPE. The curves are obtained for the drawing lengths of (from up to down): 100, 140, and 300 mm. The experiments were performed at $T = 150^{\circ}\text{C}$.

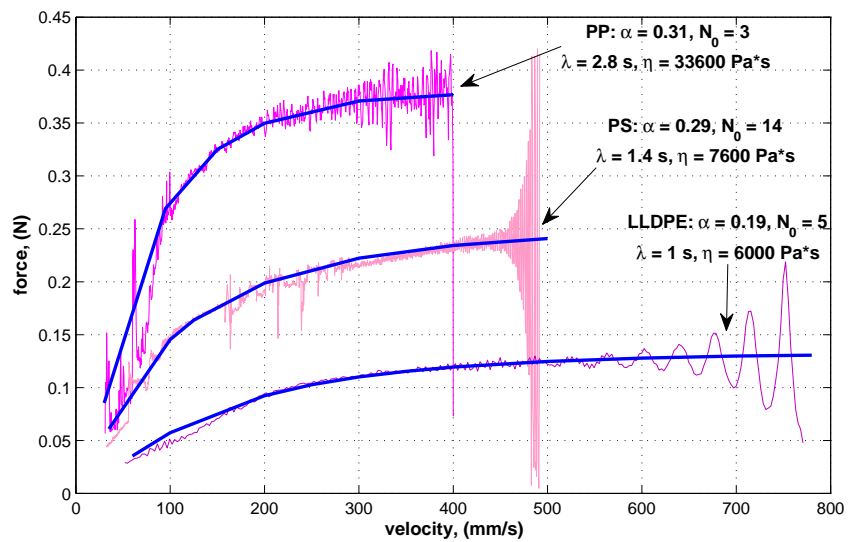


Figure 3.32: Demonstration of the Rheotens curves fitted under the steady state conditions for LLDPE, PP, and PS

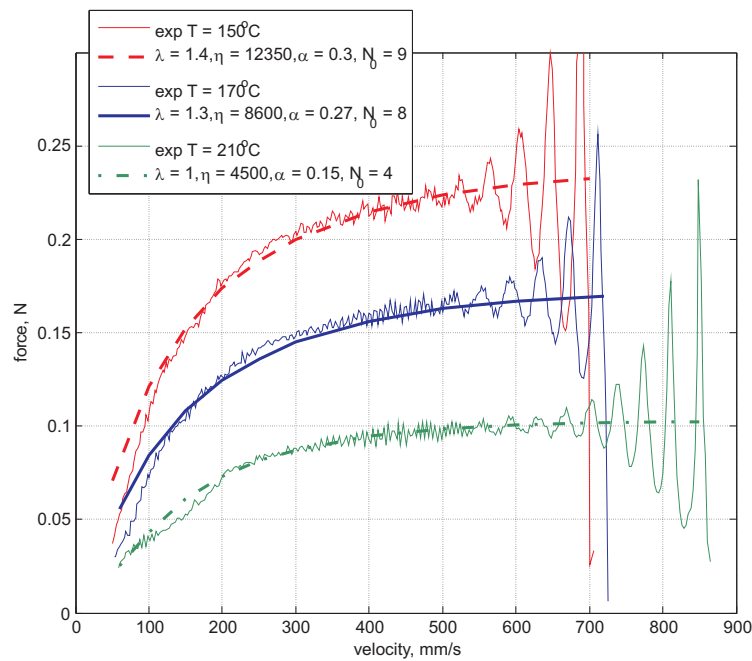


Figure 3.33: Demonstration of the fitted under the steady state conditions Rheotens curves obtained for LLDPE 1 at three different temperatures: $T = 150, 170,$ and 210°C .

Conclusions

The results presented in the previous section show the accuracy and efficiency of the suggested methodology for model parameters estimation when the modified Giesekus model is applied in the mathematical description. Analysis of the data obtained by the Rheotens constant mode, when the velocity of the pulling wheels is constant, proves the importance of those experimental data not only for the parameter determination problem, but for many other possible applications.

Appendix B

B1 Viscosity Data for LDPE at 150⁰C

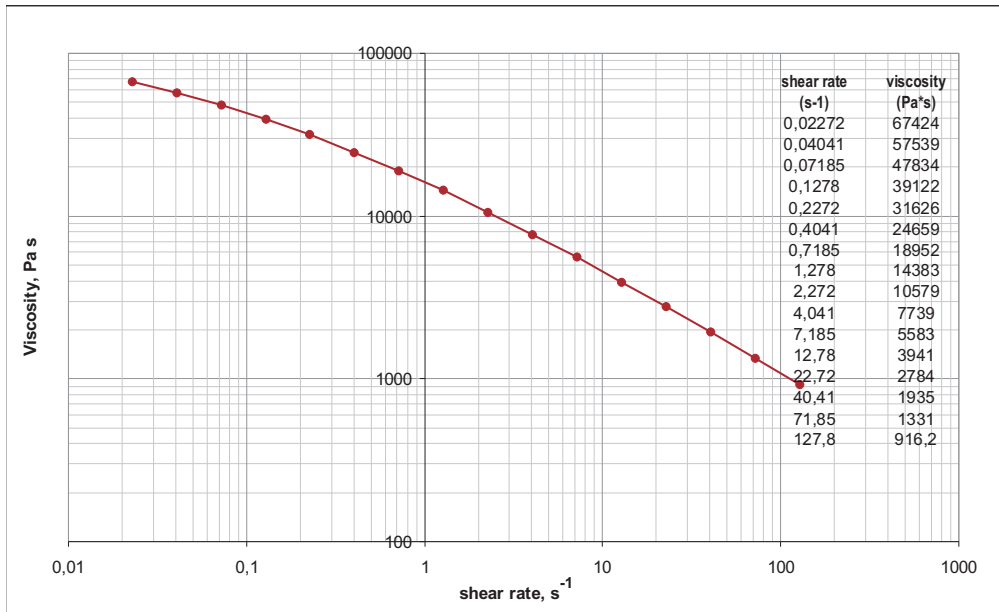


Figure B.1: Viscosity versus shear rate for LDPE at 150⁰C.

Film Casting

4.1 Introduction

4.1.1 Description of the Process

In the process of film casting, a molten polymer is extruded through a flat die, elongated, and taken up by a rotating chill roll (see Figure 4.1). The elongation is due to the positive difference between the take-up velocity at the chill roll and the extrusion velocity. The distance between the die and the chill roll is relatively short, with respect to the die width. Although the film is mainly cooled at the chill roll, the casting process between the die and the chill-roll is not completely isothermal. The polymer also loses heat by convection that happens due to the motion of the hot polymer in low temperature environment and due to blown quench air.

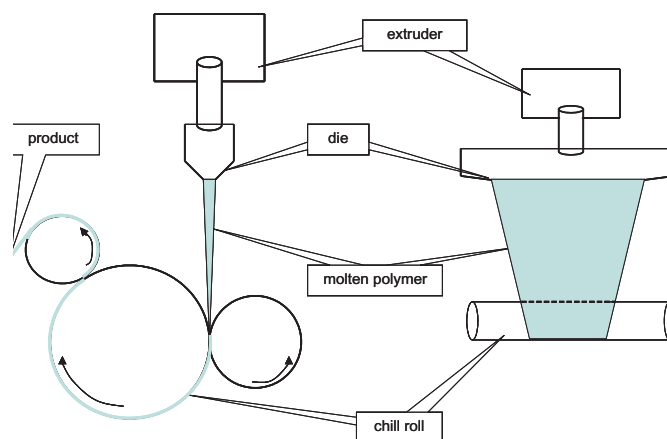


Figure 4.1: Production process: front and side view.

The productivity of the process is linearly related to draw velocity that is only limited by the

equipment and by the material. As newer cast film lines allow operations at ever higher speed, an opportunity arises for development of new resins that would have high drawability and, most importantly, would avoid stretching instability, called "draw resonance". This instability manifests itself as sudden periodic variations of film dimensions that occur at high production speeds but still below the take-up speed expected to lead to breakage. In order to develop materials with high performance, it is critical to be able to accurately predict the onset of draw resonance, taking into account the effect of cooling.

4.1.2 Literature Review

From the earliest observations of draw resonance, in the beginning of the 60-ties, many experimental and theoretical studies on this subject have been carried out. Different constitutive models describing the polymer behavior were adopted in modeling the film casting process. In particular, we can mention the work of *Silagy et al.* [70; 71], who used Newtonian, Maxwell, and Phan-Thien and Tanner constitutive models; *Anturkar and Co* [72] with the Maxwell model; *Lee et al.* [73; 74] with the Phan-Thien and Tanner model; *Iyengar and Co* [75; 76] with a Giesekus model. The resulting mathematical model of the casting process is represented by a quasi-linear system of first order partial differential equations. This model allows to replace the process instability by a mathematical instability that can be tackled with various techniques. Most researchers, like *Silagy et al.* [70; 71], *Anturkar and Co* [72], *Pis-Lopez and Co* [77; 78] treat stability of the system by performing linear stability analysis. Other researchers approached the stability problem by using a non-linear analysis, *Iyengar and Co* [76], a kinematic wave approach, *Lee et al.* [73; 74; 79], and a frequency response method, *Lee et al.* [80].

The non-isothermality of the film casting process has drawn more attention in recent years and is considered only in a few papers, for instance in work of *Sologoub et al.* [81], *Agassant et al.* [82], *Lamberti et al.* [84; 85], *Smith* [86], [87]. These works concentrate on the modeling of the steady state of the process; stability is not addressed. The work of *Smith* [86] is an exception, though it presents only one result related to the temperature influence on process stability.

4.1.3 Objective

In this chapter, a non-isothermal viscoelastic model describing the film casting process is considered. The model is one-dimensional in the sense that all unknown functions depend on one space variable. In the model, temperature is incorporated through forced and natural convection of heat. Heat diffusion, radiation, and heat dissipation are neglected. To model the polymer's rheological behavior, a number of constitutive equations are used, including Newtonian, upper convected Maxwell, Phan-Thien and Tanner, and the modified Giesekus constitutive equations. In the end, regardless of the constitutive equations used, the model of the film casting process is described by the same mathematical formulation that satisfies the conditions in Chapter 2. Thus, to solve the problem of stability/instability, we apply the mathematical and numerical routines that are based on the spectral analysis described in Chapter 2. We do not present or discuss the steady state re-

sults of our modeling. They are in full agreement with the results reported in [70] for the 1 – D model. We mention that 2 – D steady state models of film casting are also considered in literature; their results are reported in [71], [83]. These 2 – D models predict both, the neck-in effect in film width as well as the edge-bead effect in film thickness. Our objective is not focusing on steady state but on the investigation of the stability of the film casting process, especially with temperature taken into account. Therefore, we present stability results obtained under both, isothermal and non-isothermal conditions. We discuss the difference between the stability maps built for the same material if different constitutive equations are considered, and try to find which constitutive model is most efficient, if any, by comparison with some available experimental data.

4.2 Modeling

4.2.1 Configuration

Figure 4.2 shows the geometry of the polymer flow in the film casting process. The configuration is described in Cartesian coordinates. The x -direction is the length direction of the polymer flow, y - and z -directions are the width and the thickness directions, respectively. The process is assumed

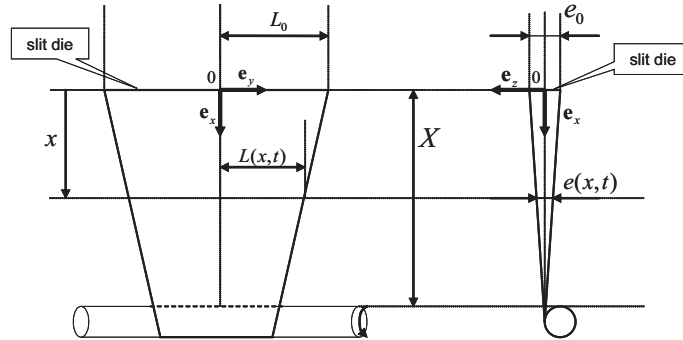


Figure 4.2: Modeling geometry of a film casting process.

to be symmetric with respect to the x -axis and with respect to the y axis. This assumption allows us to consider from now on a polymer flow in the following space-and-time domain

$$\Omega = \{(x, y, z, t) \mid 0 \leq x \leq X, 0 \leq y \leq L(x, z, t), 0 \leq z \leq \frac{1}{2}e(x, y, t), t \geq 0\}, \quad (4.1)$$

where X is the stretching distance, i.e. the distance between the die exit and the chill roll; $L(x, z, t)$ is half the width, and $e(x, y, t)$ is the thickness of the film. The initial values of $L(x, z, t)$ and $e(x, y, t)$ are given by the dimensions of the die, L_0 and e_0 . On the flow domain Ω we introduce a general velocity field $\mathbf{u} = (u_x, u_y, u_z)$, the stresses in the film σ_{ij} , and the temperature $T = T(\mathbf{x}, t)$ of the film. Variables $\mathbf{x} = (x, y, z)$ and t are independent.

The mean extrusion velocity of the polymer is denoted by u_0 , and the chill roll velocity is u_{roll} . The temperature of the polymer melt at the die exit is T_0 . Main cooling of the film takes place at the chill roll. Yet, the casting process cannot be considered as isothermal. The polymer fluid loses

heat because of natural and forced heat convection. The forced heat convection is induced by the motion of the hot polymer in a low temperature environment. If necessary, additional cooling can be applied by means of quench air blown around the polymer flow.

4.2.2 Assumptions

In our mathematical modeling the following assumptions are made:

1. The thickness e_0 is small compared to the other dimensions L_0 and X , while L_0 and X have the same order of magnitude: $X \sim L_0$, $e_0 \ll L_0$ and $e_0 \ll X$. Thus, we apply the membrane hypothesis in our further derivations, [70].
2. Effects such as gravity, surface stress, and inertia are neglected.
3. The polymer fluid is mechanically and thermally incompressible, i.e. $\text{div}\mathbf{v} = 0$ and the density of the polymer does not change with temperature.
4. The influence of extrudate swell on the process is negligible.
5. The velocity component $u_x(\mathbf{x}, t)$ is independent of y and z ($u_x = u(x, t)$), $u_y(\mathbf{x}, t)$ is independent of z , and $v_z(\mathbf{x}, t)$ is independent of y . Consequently, also taking into account incompressibility, $v_y(\mathbf{x}, t)$ and $u_z(\mathbf{x}, t)$ vary linearly with their respective coordinates, [70],

$$\mathbf{u}(\mathbf{x}, t) = u(x, t)\mathbf{e}_x + yf(x, t)\mathbf{e}_y + zg(x, t)\mathbf{e}_z. \quad (4.2)$$

6. The width and the thickness of the film are independent of y and z , respectively:

$$L = L(x, t), \quad \text{and} \quad e = e(x, t). \quad (4.3)$$

7. The polymeric fluid is in nearly equilibrium state after it exits the die, i.e. all extra stresses are relaxed.
8. Variation of the temperature over the cross-section is small compared to the variation in draw direction.
9. Heat transport in the film is only due to convection, diffusion is neglected. Viscous heat dissipation and radiation are neglected.

4.2.3 The Model Equations

In this section we present all equations involved in our mathematical model of non-isothermal film casting. Our assumptions imply that the fundamental unknowns of our problem are: $u(x, t)$, $f(x, t)$, $g(x, t)$, $L(x, t)$, $e(x, t)$, the normal stresses $\sigma_{xx}(x, t)$, $\sigma_{yy}(x, t)$, $\sigma_{zz}(x, t)$, and the temperature $T(x, t)$. For these unknowns we have the following general relations:

- Conservation of mass (cf Assumption 3)

$$\frac{\partial}{\partial t}(eL) + \frac{\partial}{\partial x}(eLv) = 0. \quad (4.4)$$

- The equation of motion (cf Assumption 2)

$$\frac{\partial}{\partial x}(\sigma_{xx}eL) = 0. \quad (4.5)$$

- By Assumption 2, the edges $y = L(x, t)$ and $z = e(x, t)$ of the film are stress free and kinematic free material surfaces.

a) From the stress free surface condition, $\sigma \mathbf{n} = \mathbf{0}$, with $\mathbf{n} = \sin \alpha \mathbf{e}_x + \cos \alpha \mathbf{e}_y$ (see Figure 4.3), we get

$$\sigma_{xx} \sin \alpha + \sigma_{xy} \cos \alpha = 0, \quad (4.6)$$

$$\sigma_{xy} \sin \alpha + \sigma_{yy} \cos \alpha = 0, \quad (4.7)$$

$$\sigma_{zz} = 0. \quad (4.8)$$

After elimination of σ_{xy} in (4.6) and (4.7), and with use of $\tan \alpha = -\frac{\partial L}{\partial x}$, we obtain

$$\sigma_{yy} = \left(\frac{\partial L}{\partial x} \right)^2 \sigma_{xx}. \quad (4.9)$$

Assumption 1 (the membrane hypothesis) implies that (4.8) and (4.9) hold everywhere in Ω .

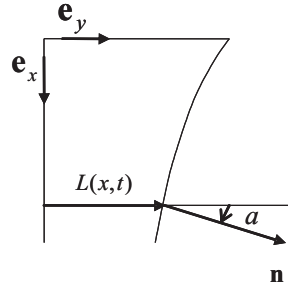


Figure 4.3: The 2 – D geometry expressing the boundary conditions at the edges of the film.

b) From the kinematic free material surface condition, $\mathbf{v} \mathbf{n} = 0$, we obtain the velocity components yf and zg , see (4.2), with

$$f = \frac{1}{L} \frac{\partial L}{\partial t} + \frac{v}{L} \frac{\partial L}{\partial x}, \quad (4.10)$$

and

$$g = \frac{1}{e} \frac{\partial e}{\partial t} + \frac{v}{e} \frac{\partial e}{\partial x}. \quad (4.11)$$

- We consider the temperature averaged over the cross-section (Assumption 8). The temperature change is a quasi-static process¹ driven by convection only (Assumption 9),

$$\rho C_p v \frac{\partial T}{\partial x} = -\frac{2h}{e}(T - T_a), \quad (4.12)$$

where T_a is an ambient air temperature, in K . The heat capacity of the polymer C_p is assumed to depend linearly on the temperature

$$C_p = a + bT, \quad \text{where } a = 969.9, \quad b = 3.7. \quad (4.13)$$

The heat transfer coefficient h accounts for a heat transfer due to forced and natural convection, $h = h_{\text{force}} + h_{\text{nat}}$. Representation of h_f and h_{nat} that are used in the modeling are given by [91]:

$$h_{\text{force}} = \frac{0.66k_a}{x} \left(\frac{C_a \eta_a}{k_a} \right)^{1/3} \left(\frac{xv_t}{\mu_a} \right)^{1/2}, \quad (4.14)$$

$$h_{\text{nat}} = \frac{0.56k_a}{x} \left(\frac{gx^3 C_a \rho_a (T - T_a)}{\mu_a k_a T_a} \right)^{1/4}. \quad (4.15)$$

In (4.14) and (4.15) quantities k_a , C_a , η_a , μ_a denote conductivity, heat capacity, dynamic viscosity, and kinematic viscosity of air, respectively; their values are given in Appendix C1. Quantity g is the magnitude of gravitational acceleration. The total velocity term v_t in (4.14) is composed of two: $v_t = v_a + u$, with v_a being the cooling air velocity.

- Constitutive equations are used to describe polymer rheological behavior. Depending on the constitutive model chosen the extra-stress tensor \mathcal{T} (components τ_{ij}) takes a different form. Thus, the total stress tensor σ (components σ_{ij}) also depends on the model selected, as it is expressed via the extra-stress tensor with addition of the isostatic pressure $p = p(x, t)$,

$$\sigma = -p\mathcal{I} + \mathcal{T}. \quad (4.16)$$

In further derivations the upper convected derivative is employed that in its general form is defined as

$$\frac{D}{Dt} * = \frac{\partial}{\partial t} * + (\mathbf{v}, \frac{\partial}{\partial \mathbf{x}}) * - \mathcal{L} * - * \mathcal{L}^T, \quad (4.17)$$

with \mathcal{L} the gradient of the velocity field, $\mathcal{L} = \text{grad} \mathbf{v}$. Because the polymer flow is strongly elongational, the diagonal terms of \mathcal{L} dominate the off-diagonal ones. Thus, we ignore off-diagonal terms,

$$\mathcal{L} = \begin{pmatrix} \frac{\partial u}{\partial x} & 0 & 0 \\ y \frac{\partial f}{\partial x} & f & 0 \\ z \frac{\partial g}{\partial x} & 0 & g \end{pmatrix} \simeq \begin{pmatrix} \frac{\partial u}{\partial x} & 0 & 0 \\ 0 & f & 0 \\ 0 & 0 & g \end{pmatrix}. \quad (4.18)$$

¹The proof that we can neglect the time derivatives is presented in Appendix C1

By ignoring off-diagonal terms we keep the model one-dimensional (in the sense that all unknowns depend only on the one variable x).

Also everywhere further λ denotes the characteristic relaxation time of the polymer (as we consider only one mode models); η denotes the viscosity of a polymer. The temperature dependence of both, λ and η , is assumed to be covered by the Arrhenius law,

$$\lambda(T) = \lambda_0 \exp \left[\frac{E_a}{RT_0} \left(\frac{T_0}{T} - 1 \right) \right], \quad (4.19)$$

$$\eta(T) = \eta_0 \exp \left[\frac{E_a}{RT_0} \left(\frac{T_0}{T} - 1 \right) \right], \quad (4.20)$$

where E_a is the activation energy of the polymer, T_0 - reference temperature that we take as the extrusion temperature, R - the universal gas constant, λ_0 and η_0 are the values of the relaxation time and the viscosity at the die temperature T_0 : $\lambda_0 = \lambda(T_0)$, $\eta_0 = \eta(T_0)$.

a) For Newtonian, upper convected Maxwell (UCM), and Phan-Thien and Tanner (PTT) fluids the extra-stress tensor is governed by the constitutive equation expressed by the same general form,

$$H(\mathcal{T})\mathcal{T} + \lambda \frac{D\mathcal{T}}{Dt} = 2\eta\mathcal{D}. \quad (4.21)$$

Here \mathcal{D} is the rate of deformation tensor, $\mathcal{D} = \frac{1}{2}(\mathcal{L} + \mathcal{L}^T)$. The relaxation time λ for the Newtonian model is zero. The tensor $H(\mathcal{T})$ satisfies the following relation

$$H(\mathcal{T}) = \begin{cases} \mathcal{I}, & \text{Maxwell, Newton;} \\ \exp\left(\frac{\varepsilon\lambda}{\eta} \text{tr}(\mathcal{T})\right)\mathcal{I}, & \text{PTT, [88],} \end{cases} \quad (4.22)$$

where ε is a PTT model parameter. In this work we consider the one-parameter PTT model.

By use of the stress free surface condition (4.8), relation (4.16) yields $p = \tau_{zz}$ and the following expression for the components of the stress tensor

$$\sigma_{xx} = \tau_{xx} - \tau_{zz}, \quad \sigma_{yy} = \tau_{yy} - \tau_{zz}. \quad (4.23)$$

With the velocity gradient given by (4.18) and the upper convective derivative defined by (4.17), the constitutive equations for τ_{xx} , τ_{yy} , and τ_{zz} are fully defined by (4.21). Using relation (4.23) thereafter, we get the following three constitutive equations for τ_{xx} , σ_{xx} and σ_{yy} :

$$H\tau_{xx} + \lambda \left(\frac{\partial \tau_{xx}}{\partial t} + u \frac{\partial \tau_{xx}}{\partial x} - 2\tau_{xx} \frac{\partial u}{\partial x} \right) = 2\eta \frac{\partial u}{\partial x}, \quad (4.24)$$

$$H\sigma_{xx} + \lambda \left(\frac{\partial \sigma_{xx}}{\partial t} + u \frac{\partial \sigma_{xx}}{\partial x} - 2\tau_{xx} \left(\frac{\partial u}{\partial x} - g \right) - 2\sigma_{xx}g \right) = 2\eta \left(\frac{\partial u}{\partial x} - g \right), \quad (4.25)$$

$$H\sigma_{yy} + \lambda \left(\frac{\partial \sigma_{yy}}{\partial t} + u \frac{\partial \sigma_{yy}}{\partial x} + 2(\sigma_{xx} - \tau_{xx})(f - g) - 2\sigma_{yy}f \right) = 2\eta(f - g), \quad (4.26)$$

where the functions f and g are given by (4.10) and (4.11), function H is given by

$$H = \begin{cases} 1, & \text{Maxwell, Newton;} \\ \exp\left(\frac{\varepsilon\lambda_0}{\eta_0} (3\tau_{xx} + \sigma_{yy} - 2\sigma_{xx})\right), & \text{PTT,} \end{cases} \quad (4.27)$$

and $\lambda = 0$ in case of Newtonian fluid.

b) Developing the modified Giesekus model, we follow the method that was introduced by *Doufas et al.* [20] in their modeling of the fiber spinning process. We consider the stress tensor σ in terms of the conformation tensor \mathcal{C} (components c_{ij}) instead of the extra stress. Thus, in (4.16) the extra-stress tensor \mathcal{T} is replaced by the conformation tensor \mathcal{C} , using the following relation

$$\mathcal{T} = nk_b T \left(\frac{3}{N_0 l^2} E \mathcal{C} - \mathcal{I} \right). \quad (4.28)$$

The conformation tensor \mathcal{C} is proposed to characterize the microstructure, i.e. the orientation and stretching of the molecules in a melt. The polymer melt exiting the die is modeled as a concentrated suspension of non-linear elastic dumbbell molecules. Each molecular chain is assumed to contain N_0 flexible statistical links of length l . In (4.28), n is the number of molecules per unit volume, and k_b is the Boltzmann constant. The quantity E , the non-linear spring force factor, accounts for a finite chain extensibility and is approximated by *Cohen* [62] with the following expression

$$E = \frac{3N_0^2 l^2 - \text{tr} \mathcal{C}}{3N_0^2 l^2 - 3\text{tr} \mathcal{C}}. \quad (4.29)$$

By substitution of (4.28) into (4.16) and use of the condition (4.8), the stress tensor components σ_{xx} and σ_{yy} are expressed via the conformation tensor. They are then used to modify equations (4.5) and (4.9) that in terms of conformation tensor components become

$$\frac{\partial}{\partial x} (E(c_{xx} - c_{zz})eL) = 0, \quad (4.30)$$

$$(c_{xx} - c_{zz}) \left(\frac{\partial L}{\partial x} \right)^2 = (c_{yy} - c_{zz}). \quad (4.31)$$

The evolution equation for the conformation tensor \mathcal{C} is given by

$$\frac{D}{Dt} \mathcal{C} = -\frac{1}{\lambda} \frac{N_0 l^2}{3} \left((1 - \alpha) \mathcal{I} + \alpha \frac{3}{N_0 l^2} E \mathcal{C} \right) \left(\frac{3}{N_0 l^2} E \mathcal{C} - \mathcal{I} \right). \quad (4.32)$$

Here α is a modified Giesekus model parameter representing molecular mobility. With (4.17) and (4.18), the evolution equation of conformation tensor (4.32) in components reads

$$\lambda \left(\frac{\partial c_{xx}}{\partial t} + u \frac{\partial c_{xx}}{\partial x} - 2c_{xx} \frac{\partial u}{\partial x} \right) = \frac{N_0 l^2}{3} \left((1 - \alpha) + \alpha \frac{3}{N_0 l^2} E c_{xx} \right) \left(1 - \frac{3}{N_0 l^2} E c_{xx} \right), \quad (4.33)$$

$$\lambda \left(\frac{\partial c_{yy}}{\partial t} + u \frac{\partial c_{yy}}{\partial x} - 2c_{xx} f \right) = \frac{N_0 l^2}{3} \left((1 - \alpha) + \alpha \frac{3}{N_0 l^2} E c_{yy} \right) \left(1 - \frac{3}{N_0 l^2} E c_{yy} \right), \quad (4.34)$$

$$\lambda \left(\frac{\partial c_{zz}}{\partial t} + u \frac{\partial c_{zz}}{\partial x} - 2c_{zz} g \right) = \frac{N_0 l^2}{3} \left((1 - \alpha) + \alpha \frac{3}{N_0 l^2} E c_{zz} \right) \left(1 - \frac{3}{N_0 l^2} E c_{zz} \right). \quad (4.35)$$

The functions f and g are given by (4.10) and (4.11).

With this, for every model considered, except for the Newtonian case, we derive a system of 7 first order non-linear differential equations for 7 unknowns. The Newtonian model results in 5 equations for 5 unknowns.

4.2.4 Boundary Conditions

To have a consistent model, we need to introduce boundary conditions. Since we have a one-dimensional problem with respect to variable x , the boundaries are $x = 0$ and $x = X$. From the process conditions, we introduce the following obvious boundary conditions:

$$u(0, t) = u_0, \quad L(0, t) = L_0, \quad e(0, t) = e_0, \quad T(0, t) = T_0, \quad u(X, t) = u_{roll}. \quad (4.36)$$

For the Newtonian case these boundary conditions suffice. For the Maxwell and for the PTT fluid model we need two more conditions, namely one for τ_{xx} and one for σ_{yy} . The boundary condition for τ_{xx} is less obvious. We assume that polymer exiting the die is nearly at equilibrium, the extra stresses are relaxed or close to, thus we put

$$\tau_{xx}(0, t) = k_0, \quad (4.37)$$

where k_0 is positive and small, close to zero. This is in agreement with the previous research [70], [89]. For the component σ_{yy} , we solve the Newtonian steady state problem and then use the obtained value $\sigma_{yy}(0)^{Newtonian}$ as the boundary value for the Maxwell and PTT case,

$$\sigma_{yy}(0, t) = \sigma_{yy}(0)^{Newtonian}. \quad (4.38)$$

In case of the modified Giesekus model, boundary conditions for the conformation tensor components are needed. According to Assumption 7, boundary values of c_{yy} and c_{zz} at the die exit, $x = 0$, are taken at equilibrium:

$$c_{yy}(0, t) = c_{yy}^{eq}, \quad c_{zz}(0, t) = c_{zz}^{eq}. \quad (4.39)$$

As at equilibrium all extra-stresses are relaxed, we get c_{yy}^{eq} and c_{zz}^{eq} from (4.28):

$$c_{ii}^{eq} = \frac{N_0 l^2}{3E_{eq}}. \quad (4.40)$$

To find $E_{eq} = E(C^{eq})$, we substitute (4.40) in (4.29) and solve the resulting second order equation with respect to E_{eq} ,

$$E_{eq} = \frac{1 + N_0}{2N_0} + \frac{\sqrt{9 + 6N_0 + 9N_0^2}}{6N_0}. \quad (4.41)$$

4.2.5 Scaling

To have a concise form of governing equations, and also to see better which parameters have influence on the solution stability, we use a dimensionless form of the system. For that, the following dimensionless variables are used:

$$\hat{u} = \frac{u}{u_0}; \quad \hat{e} = \frac{e}{e_0}; \quad \hat{L} = \frac{L}{L_0}; \quad \hat{x} = \frac{x}{X}; \quad \hat{T} = \frac{T}{T_0}; \quad \hat{t} = \frac{X}{u_0} t. \quad (4.42)$$

For the consideration of the Newtonian, UCM, and PTT models, the stress tensor and extra-stress tensor components are scaled according to

$$\hat{\sigma}_{ii} = \frac{\sigma_{ii}e_0L_0}{F_0}; \quad \hat{\tau}_{ii} = \frac{\tau_{ii}e_0L_0}{F_0}, \quad (4.43)$$

where the value F_0 represents the force in x -direction at $x = 0$. In case of the modified Giesekus model, the conformation tensor components become dimensionless by

$$\hat{c}_{ii} = \frac{c_{ii}}{N_0l^2/3}. \quad (4.44)$$

The important dimensionless processing parameters are the Draw ratio (Dr), and the Aspect ratio (A)

$$Dr = \frac{u_{roll}}{u_0}; \quad A = \frac{X}{L_0};$$

and the Deborah number (De), representing ratios of relaxation time and a process time,

$$De(T) = De_0 \exp \left[\frac{E_a}{RT_0} \left(\frac{1}{T} - 1 \right) \right]. \quad (4.45)$$

Here De_0 is the value at initial temperature T_0 , $De_0 = \frac{\lambda_0 u_0}{L}$.

4.2.6 Dimensionless System

In representation of the scaled systems, for convenience, the hats over scaled variables are omitted and the following dimensionless groups are introduced

$$V_1(T_a, u, e; x) = \frac{1.32k_a}{\rho u_0 e_0} \left(\frac{C_{pa}\eta_a}{k_a} \right)^{1/3} \left(\frac{X(u_0u + v_a)}{\nu_a} \right)^{1/2} \frac{1}{ue\sqrt{x}}, \quad (4.46)$$

$$V_2(T_a, u, e; x) = \frac{2Bk_a}{\rho u_0 e_0} \left(\frac{gX^3 C_{pa}\rho_a T_0}{\nu_a k_a T_a} \right)^p \frac{x^{3p-1}}{ue}, \quad (4.47)$$

$$W(T) = \frac{\eta_0 e_0 L_0 u_0}{F_0 X} \exp \left[\frac{E_a}{RT_0} \left(\frac{1}{T} - 1 \right) \right], \quad (4.48)$$

$$K_x(x, t) = ((1 - \alpha) + \alpha Ec_{xx}) (1 - Ec_{xx}), \quad (4.49)$$

$$K_y(x, t) = ((1 - \alpha) + \alpha Ec_{yy}) (1 - Ec_{yy}), \quad (4.50)$$

$$K_z(x, t) = ((1 - \alpha) + \alpha Ec_{zz}) (1 - Ec_{zz}). \quad (4.51)$$

The non-linear force factor E , see (4.29), and its derivative in scaled variables take the form

$$E = \frac{9N_0 - trC}{9N_0 - 3trC}, \quad (4.52)$$

$$\frac{\partial E}{\partial x} = \frac{2N_0}{(3N_0 - trC)^2} \frac{\partial(trC)}{\partial x}. \quad (4.53)$$

Further also, to make system look simpler, the total time derivative is used,

$$\frac{\delta}{\delta t} = \frac{\partial}{\partial t} + u \frac{\partial}{\partial x}. \quad (4.54)$$

With such grouping and notations, the system characterizing the non-isothermal film casting of a viscoelastic polymer takes the form

- for the Newtonian, UCM, and PTT cases

$$H\tau_{xx} + De \left(\frac{\delta\tau_{xx}}{\delta t} - 2\tau_{xx} \frac{\partial u}{\partial x} \right) = 2W \frac{\partial u}{\partial x}, \quad (4.55)$$

$$H\sigma_{xx} + De \left(\frac{\delta\sigma_{xx}}{\delta t} - 2\tau_{xx} \left(\frac{\partial u}{\partial x} - \frac{1}{e} \frac{\delta e}{\delta t} \right) - 2 \frac{\sigma_{xx}}{e} \frac{\delta e}{\delta t} \right) = 2W \left(\frac{\partial u}{\partial x} - \frac{1}{e} \frac{\delta e}{\delta t} \right), \quad (4.56)$$

$$H\sigma_{yy} + De \left(\frac{\delta\sigma_{yy}}{\delta t} + 2(\sigma_{xx} - \tau_{xx}) \left(\frac{1}{L} \frac{\delta L}{\delta t} - \frac{1}{e} \frac{\delta e}{\delta t} \right) - 2\sigma_{yy} \frac{1}{L} \frac{\delta L}{\delta t} \right) = 2W \left(\frac{1}{L} \frac{\delta L}{\delta t} - \frac{1}{e} \frac{\delta e}{\delta t} \right), \quad (4.57)$$

$$A^2 \sigma_{yy} = \sigma_{xx} \left(\frac{\partial L}{\partial x} \right)^2, \quad (4.58)$$

$$\frac{\partial}{\partial t} (eL) + \frac{\partial}{\partial x} (eLu) = 0, \quad (4.59)$$

$$\frac{\partial}{\partial x} (\sigma_{xx} eL) = 0, \quad (4.60)$$

$$\frac{\partial T}{\partial x} = -\frac{V_1}{a+bT} \left(T - \frac{T_a}{T_0} \right) - \frac{V_2}{a+bT} \left(T - \frac{T_a}{T_0} \right)^{1+p}. \quad (4.61)$$

In this system the function H equals

$$H = \begin{cases} 1, & \text{Maxwell, Newton;} \\ \exp \left(\frac{\varepsilon \lambda_0 F_0}{\eta_0 e_0 L_0} (3\tau_{xx} + \sigma_{yy} - 2\sigma_{xx}) \right), & \text{PTT,} \end{cases} \quad (4.62)$$

with ε the PTT model parameter. The system of equations (4.55)-(4.60) is valid in case of three mentioned constitutive models, namely Newtonian, Maxwell, and PTT. Just have to keep in mind that H is different in these three models, and that $De = 0$ for a Newtonian fluid.

The scaled boundary conditions are

$$u(0, t) = 1, \quad L(0, t) = 1, \quad e(0, t) = 1, \quad T(0, t) = 1, \quad u(X, t) = Dr. \quad (4.63)$$

Those four conditions completely specify the Newtonian model. For the Maxwell and PTT in addition we demand

$$\tau_{xx}(0, t) = k = \frac{k_0 e_0 L_0}{F_0}, \quad \sigma_{yy}(0, t) = \sigma_{yy}(0)^{Newtonian}. \quad (4.64)$$

- for the modified Giesekus the scaled equations are

$$De \left(\frac{\delta c_{xx}}{\delta t} - 2c_{xx} \frac{\partial u}{\partial x} \right) = K_x, \quad (4.65)$$

$$De \left(\frac{\delta c_{yy}}{\delta t} - 2 \frac{c_{xx}}{L} \frac{\delta L}{\delta t} \right) = K_y, \quad (4.66)$$

$$De \left(\frac{\delta c_{zz}}{\delta t} - 2c_{zz} \frac{1}{e} \frac{\delta e}{\delta t} \right) = K_z, \quad (4.67)$$

$$(c_{xx} - c_{zz}) \left(\frac{\partial L}{\partial x} \right)^2 = A^2 (c_{yy} - c_{zz}), \quad (4.68)$$

$$\frac{\partial}{\partial t} (eL) + \frac{\partial}{\partial x} (eLu) = 0, \quad (4.69)$$

$$\frac{\partial}{\partial x} (TE(c_{xx} - c_{zz})eL) = 0, \quad (4.70)$$

$$\frac{\partial T}{\partial x} = -\frac{V_1}{a+bT} \left(T - \frac{T_a}{T_0} \right) - \frac{V_2}{a+bT} \left(T - \frac{T_a}{T_0} \right)^{1+p}. \quad (4.71)$$

and the scaled boundary conditions are:

$$\begin{aligned} u(0, t) = 1, \quad L(0, t) = 1, \quad e(0, t) = 1, \quad T(0, t) = 1, \quad u(1, t) = Dr, \\ c_{yy}(0, t) = 1/E_{eq}, \quad c_{zz}(0, t) = 1/E_{eq}, \end{aligned} \quad (4.72)$$

with the equilibrium value of the non-linear force factor E_{eq} given by (4.41).

4.2.7 General Formulation

After scaling, the model of film casting, regardless of the constitutive equations chosen, Newtonian, UCM, PTT, or modified Giesekus, results in the quasi-linear system of differential equations with two points boundary conditions, as mathematically described in Chapter 2,

$$\mathcal{C}(\mathbf{y}) \frac{\partial \mathbf{y}}{\partial t} = \mathcal{A}(\mathbf{y}) \frac{\partial \mathbf{y}}{\partial x} + \mathbf{b}(\mathbf{y}), \quad 0 < x < 1, \quad t > 0. \quad (4.73)$$

$$P(\mathbf{y}(0, t)) = \xi, \quad Q(\mathbf{y}(1, t)) = \zeta \quad (4.74)$$

In this general formulation x and t are the independent variables; $\mathbf{y}(x, t)$ is the vector function consisting of the state variables,

- $\mathbf{y} = (L, e, u, T, \sigma_{yy})$ for the Newtonian model.
- $\mathbf{y} = (L, e, u, T, \tau_{xx}, \sigma_{xx}, \sigma_{yy})$ for the UCM, and PTT models.
- $\mathbf{y} = (L, e, u, T, c_{xx}, c_{yy}, c_{zz})$ for the modified Giesekus model.

4.3 Stability Recognition

To answer on stability/instability issues in film casting, we apply the analysis as described in Chapter 2: first we determine a steady state solution $\mathbf{y}_{steady}(x)$ from the quasi-linear system of first order differential equations with inhomogeneous boundary conditions, then we define stability as the asymptotical stability of the steady state. We linearize the initial system about the steady solution by introducing $\mathbf{y}(x, t) = \mathbf{y}_{steady}(x) + \tilde{\mathbf{y}}(x) \exp \gamma t$. The generalized eigenvalue problem that results from the linearization yields a set of characteristic values $\{\gamma\}$, which we call the spectrum. Once the spectrum is known, the stability/instability of the process is determined according to:

$$\begin{aligned} \text{if } \forall \gamma \quad Re(\gamma) < 0 & \Rightarrow \text{the solution is stable,} \\ \text{if } \exists \gamma \quad Re(\gamma) > 0 & \Rightarrow \text{the solution is unstable.} \end{aligned}$$

To calculate the spectrum $\{\gamma\}$ we use a numerical scheme, which allows to calculate a full spectrum in a matter of seconds (see Section 2.3). Here we proceed with the results of our stability analysis obtained by using different constitutive models. We discuss the numerical precision and present the spectra that reveal stability/instability in the example of the Newtonian model. The Newtonian and Maxwell models are used for validation purposes and discussed only in Section 4.3.4. In Sections 4.3.4, 4.3.5, 4.3.5 stability/instability maps are built by simulating the process using the PTT and modified Giesekus constitutive equations. Finally, in Section 4.3.6 we compare the prediction of draw resonance given by PTT and modified Giesekus models by simulating real experimental conditions with the real draw resonance onset measured in the experiments.

4.3.1 Model Parameters

In order to make a comparison between the predicted stability maps given by two constitutive models, PTT and modified Giesekus, we decide to build those maps for two types of materials, a low- and a linear low density polyethylene. More specifically, we do not talk about the particular materials but rather about their general type. To simulate the behavior of each material type, we have to choose the values of the constitutive model parameters that are representative for the type.

- Choosing of Phan-Thien and Tanner model parameters.

For LDPE, it is suggested in [90] to take $\varepsilon = 0.015$. This suggestion is confirmed at Dow, [65]; fitting the steady state Rheotens, they found ε to be in a range from 0.01 to 0.02. For LLDPE, a similar numerical experiment resulted in the values of ε ranging from 0.09 to 0.1. In this thesis we rely on these results, as we did not carry out our parameter estimation procedure for PTT model.

- Choosing the modified Giesekus model parameters.

The parameters for 3 different LLDPE materials are reported by *Doufas* in [61]. These three materials have a value for α between 0.2 and 0.3, and the value for N_0 between 20 and 35. In this thesis we determined parameters for only one LLDPE material (see Section 3.5.2).

According to our findings, the value of α varies, depending on the process temperature, from 0.15 to 0.3, which is in agreement with findings reported in [61]. The value of N_0 that we found is lower, between 4 and 9. We conclude about the values of model parameters for the material of LDPE type by analyzing the results of three different LDPE materials. Two of those LDPE's are considered in this thesis (see Section 3.5.2 and Appendix C2) and one is considered by *Doufas*, [61]. For the three LDPE materials, the value of α is found to be 0.05, 0.06 and 0.1, while the value of N_0 varies more significantly, i.e. $N_0 = 3, 7, \text{ and } 90$. Analyzing this information, we conclude that α -values for all considered LDPE's are lower than 0.1; and they are lower than the α -values for the 4 LLDPE materials considered. We cannot conclude much about the behavior of N_0 depending on the material, the variation in the values of N_0 is quite large, and thus, more investigation is needed. The sensitivity analysis, presented in Section 3.5.1, shows that N_0 does not have much influence on the prediction of draw resonance, especially when it reaches values higher than 10. We do realize that this sensitivity analysis is based on the simulations of the Rheotens experiment. However, because essentially fiber spinning and film casting are very similar processes by nature, there is reason to believe that the results in film casting depend on parameters in similar manner as the results of fiber spinning.

Having said all above, we choose the parameters for LLDPE and LDPE in the simulations of the mathematical model of film casting as given in Table 4.1.

Table 4.1: Materials and related model parameters that are used for simulations

Material	α	N_0	ε
M1 (LDPE type)	0.01	100	0.01
M2 (LLDPE type)	0.2	35	0.1

4.3.2 Numerical Precision

In our numerical approach we have to choose the number of space grid points N . The choice of N defines the precision of calculations and depends on the specifics of the problem at hand. As the complexity of model increases, the numerical results converge if a higher number of grid points N are taken in the calculations. For a Newtonian fluid, $N = 100$ yields accurate results, see Figure 4.4. For the upper convected Maxwell model and the PTT model the number of grid points should be at least 200, and for the modified Giesekus model, the number of the grid points should be at least 300.

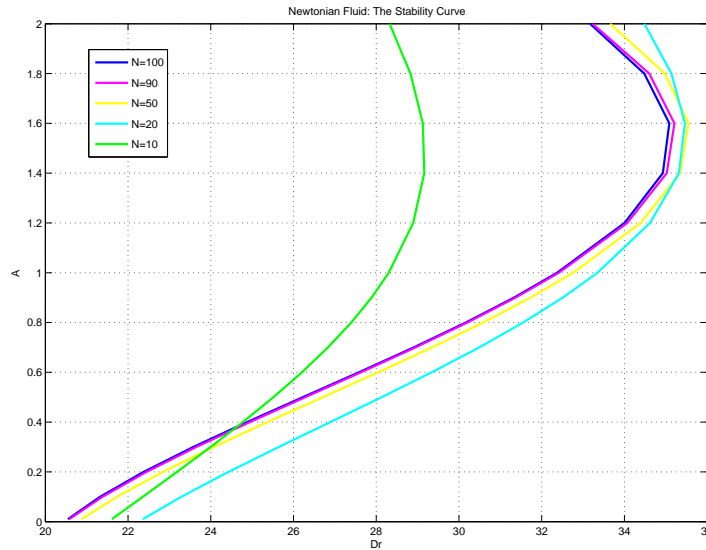


Figure 4.4: *Newtonian fluid: numerical stability curves. Each pair of input parameters Aspect ratio A and Draw ratio Dr at the left hand side of curves gives a stable film casting process, oppositely it gives instability. The curves are obtained for the number of grid points $N = \{10, 20, 50, 90, 100\}$. The curve tends to converge numerically at $N = 100$.*

4.3.3 Spectrum

The process is set stable/unstable for each given set of parameters (A, Dr) by the results of analysis of the spectrum $\{\gamma\}$ of (4.73). In this section, in Figures 4.5 and 4.6 we present the inverse of that spectrum, namely $\{\frac{1}{\gamma}\}$, which does not change the outcome of the stability analysis but gives a better visualization, i.e., without zooming one can see a complete set of $\{\frac{1}{\gamma}\}$ and the behavior of the critical points.

We consider here the examples of the spectrum for the PTT model. The analysis does not change for any other model at hand. Figure 4.5 shows the evolution of the spectrum for $(A, De) = (0.2, 0.01)$, and the number of grid points $N = 200$, when Dr is irregularly increased: $Dr = \{20, 24, 40, 50, 60, 70\}$. The investigation is made for M1 (LDPE, $\varepsilon = 0.01$) under the non-isothermal conditions but without additional cooling, i.e. $v_a = 0$ m/s.

The spectrum has a typical point that has the largest imaginary part, indicated by a circle. As Dr is increasing, this point is "moving" in the direction of the positive part of the real axis and back, thus it is critical for stability/instability. Therefore, in this case (low resolution), the system is unstable for $23 < Dr < 70$. Thus, we have two critical values of the Draw ratio Dr : $Dr = 24$ is the value when system changes from being stable to being unstable, and $Dr = 70$ is the value that indicates when system is stable again.

Next, we change the PTT model parameter ε from 0.01 to 0.1, which means we now deal with M2 (LLDPE type of material). Figure 4.6 shows the change of the spectrum for this type of resin.

Parameters and conditions are kept the same: $(A, De) = (0.2, 0.01)$, $N = 200$, $v_a = 0$ m/s. Values of the Draw ratio chosen to visualize the spectrum are $Dr = \{20, 21, 40, 60\}$. Again, we observe the presence in the spectra of a leading characteristic value that indicates stability/instability of the system. As Dr increases, the real part of this value also increases. For $Dr = 21$ the real part of the leading value becomes positive, while for $Dr = 20$ it is still negative. The critical value of Dr in this case is taken to be $D = 20.5$. In contrast to M1 (LDPE) example, the leading characteristic value is not "moving" back to the negative real half-plane as we increase Dr . On the contrary, its real part continues to grow. Moreover, new modes are coming to the positive real half-plane.

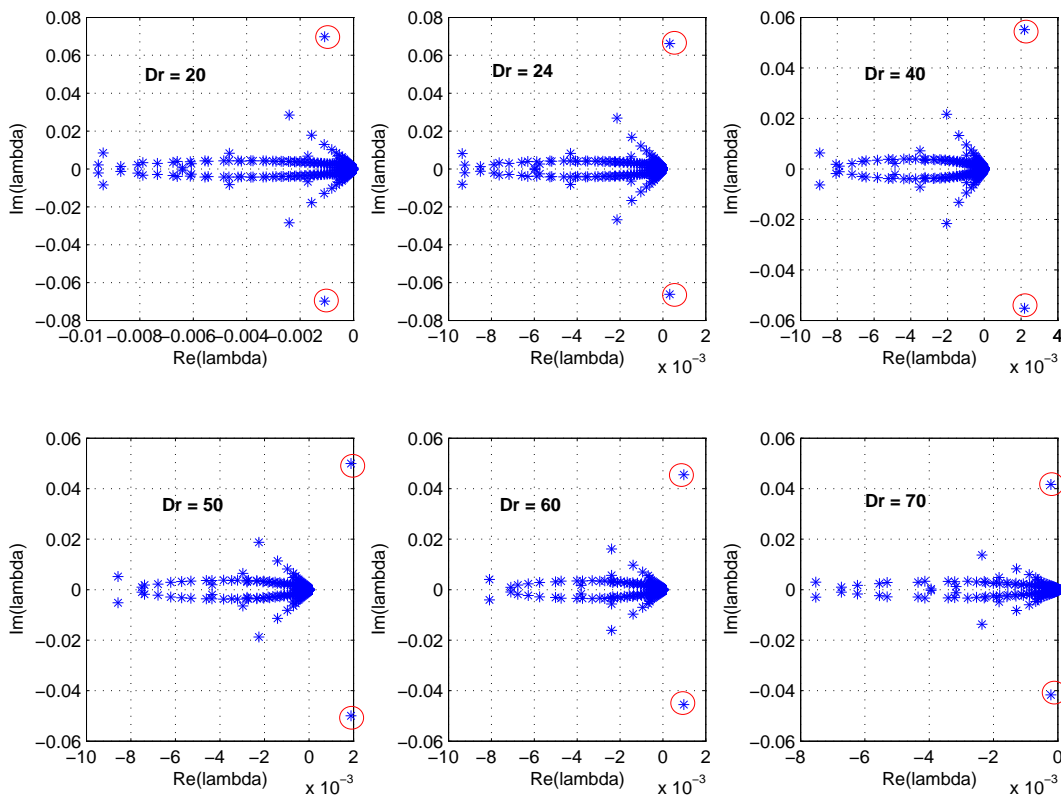


Figure 4.5: LDPE: set of $\frac{1}{\gamma}$ for $(A, De) = (0.2, 0.01)$ with $N = 200$. From left-up to right-down: $Dr = 20, 24, 40, 50, 60, 70$.

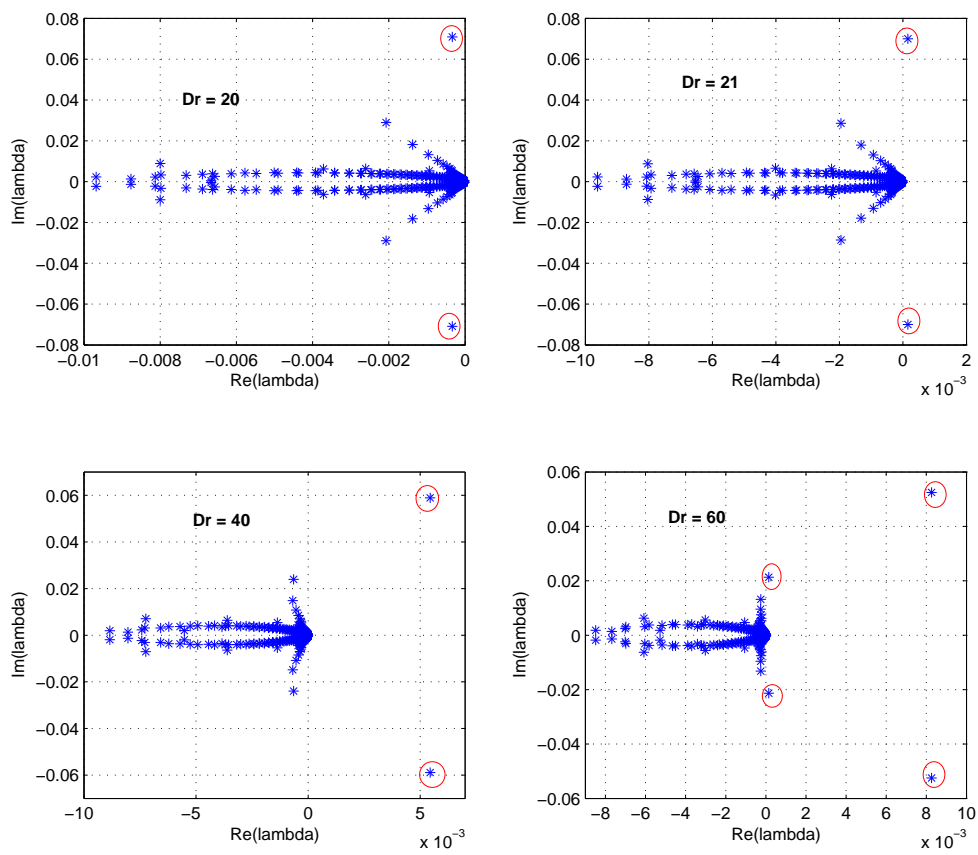


Figure 4.6: $M2$ (LLDPE): Set of $\frac{1}{\gamma}$ for $(A, De) = (0.2, 0.01)$ with $N = 200$. From left-up to right-down: $Dr = 20, 21, 40, 60$.

4.3.4 Stability Solution: Isothermal

Newton and UCM: Comparison with Literature

In this section we show that the results on stability as we obtain them are consistent and in agreement with the results presented in literature, [8; 70; 71]. While *Silagy et al.* [70; 71] consider a film casting process and present stability curves for an isothermal Newtonian and isothermal upper convected Maxwell (UCM) models, *Fisher and Denn* [8] describe a fiber spinning process. The stability curve obtained by *Silagy et al.* for a UCM model with a value of Aspect ratio close to zero coincides with the curve obtained by *Fisher and Denn*. The diagrams in Figure 4.7 show that the stability curves obtained by our method and the ones given in the references mentioned above are in complete agreement.

PTT

In this section we give the results of the isothermal PTT model. This model is obtained from the model given in Section 4.2.6 if we drop the temperature equation and temperature dependence of the variables and parameters. In Figure 4.8 we show the stability curves for the material M1 (LDPE type, $\varepsilon = 0.01$) obtained for a number of values of the Deborah number, namely $De \in \{0.008, 0.009, 0.01, 0.011, 0.012, 0.0125\}$. The stability region for each De is at the left hand side of or otherwise above its corresponding curve. As De increases, the stability region is getting larger. Moreover, for some De , playing with Dr and A we can even overcome the unstable zone. As De tends to zero, the curves tend to behave like a Newtonian stability curve ($De = 0$).

Figure 4.9 shows the stability curves of M2 (LLDPE, $\varepsilon = 0.1$) for the same values of the Deborah number as in the previous example. A stability region of each case is at the left-hand side of its corresponding curve. We see that M2 (LLDPE) shows less stability than M1 (LDPE), i.e. we meet the instability zone for smaller values of Dr than for M1 (LDPE) case. Also, in contrast to M1 (LDPE), the stability zone for M2 (LLDPE) becomes smaller as De increases. Besides, as Figure 4.9 shows, for M2 (LLDPE) we cannot overcome the unstable zone by increasing the operating velocity or geometry of the process, i.e. Dr and A .

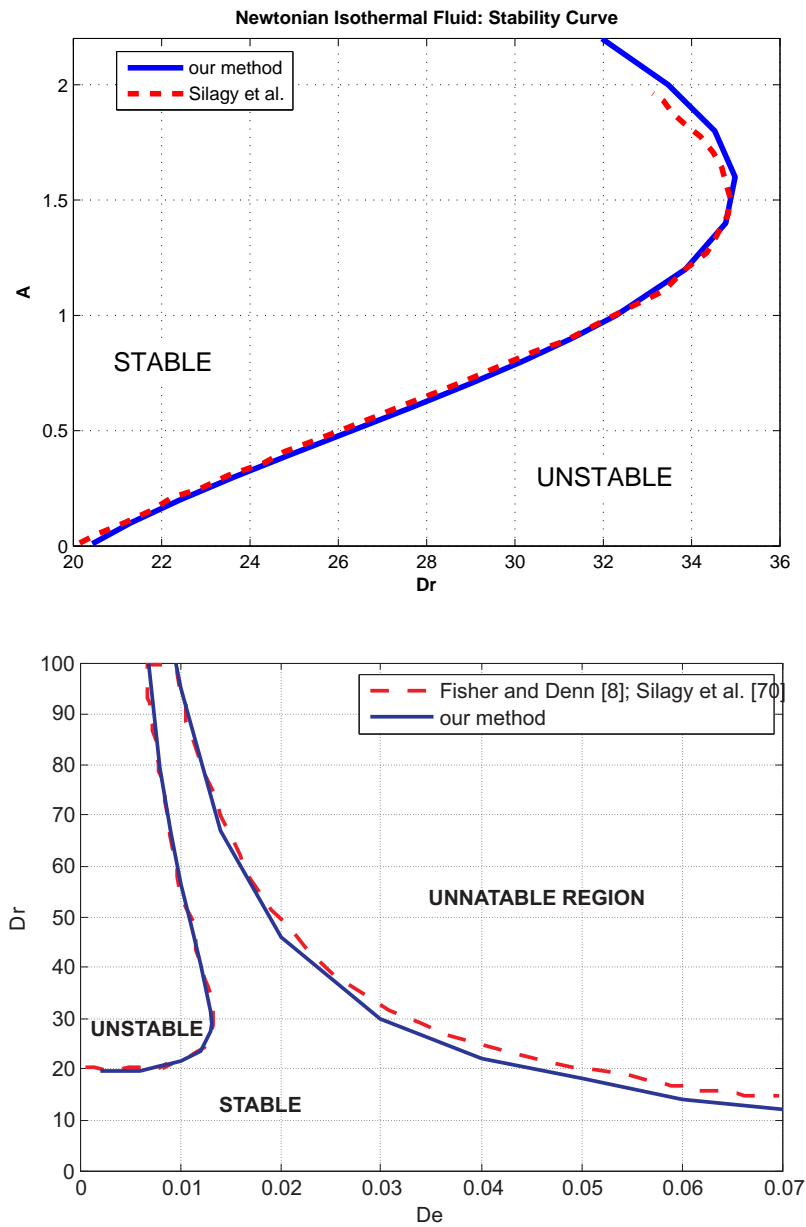


Figure 4.7: Comparison of stability diagrams resulting from an isothermal Newtonian model (up diagram) and an isothermal UCM model (bottom diagram) of the film casting process. Smooth lines are the result produced by application of our technique; dash lines are the result obtained by Fisher and Denn, Silagy et al. and presented in [8] and [70].

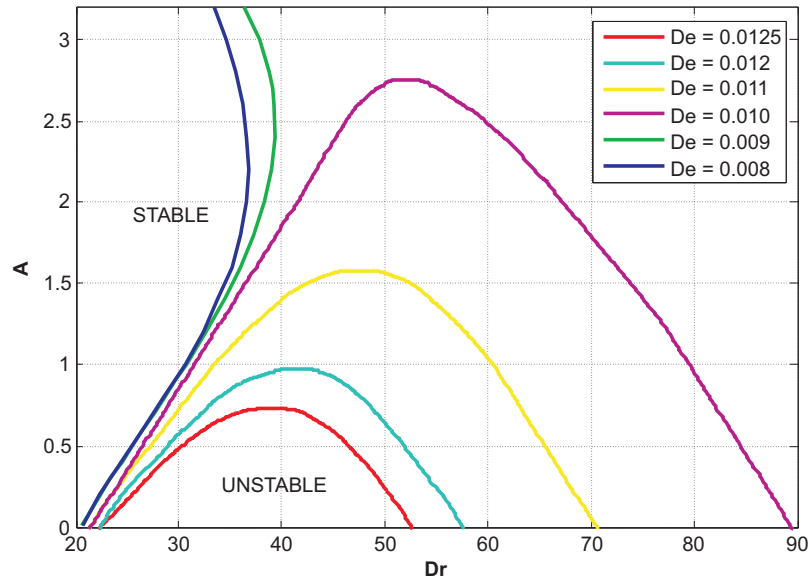


Figure 4.8: *M1 (LDPE): stability curves for different values of Deborah number, $De \in \{0.008, 0.009, 0.01, 0.011, 0.012, 0.0125\}$. A stability region of each case is at the LHS of or otherwise above its corresponding curve.*

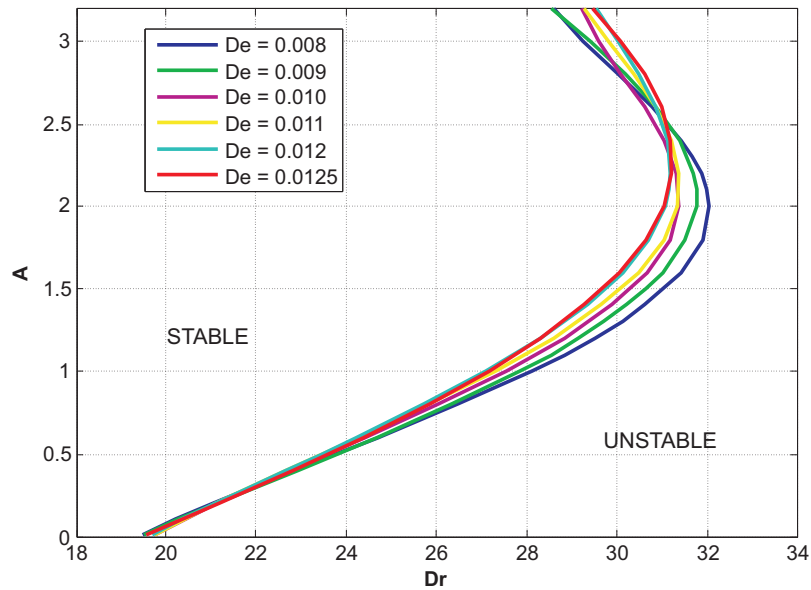


Figure 4.9: *M2 (LLDPE): stability curves for different values of parameter $De \in \{0.008, 0.009, 0.01, 0.011, 0.012, 0.0125\}$. A stability region of each case is at the LHS of its corresponding curve.*

4.3.5 Stability Solution: Non-isothermal

In this section we proceed with simulations of the behavior of M1 (LDPE) and M2 (LLDPE) resins in film casting with PTT and modified Giesekus models. Input model parameters for the resins considered are given in Table 4.1, Section 4.3.1. In the pictures below, we show general stability plots built with respect to the three main dimensionless process parameters: Aspect Ratio (A), Draw Ratio (Dr), and Deborah number (De). The curves presented indicate the critical points where the process changes from stable to unstable or vice versa. In all pictures the blue curve is built based on the results of the isothermal model. The black curve corresponds to a non-isothermal process with no cooling air, i.e., air velocity $v_a = 0$ m/s; and the red curve corresponds to a non-isothermal process with additional cooling, $v_a = 15$ m/s. Our objective is to evaluate impact of non-isothermality on the model predictions.

PTT

In this section we present two types of figures: A vs Dr for a fixed $De = 0.01$ (Figures 4.10 and 4.12); Dr vs De for a fixed $A = 0.6$ (Figures 4.11 and 4.13). In Figure 4.10, the region under the respective curve is instability region, i.e., it contains those values of the parameters, A and Dr , that make the process unstable; the complementary region is therefore a stability region. In Figure 4.11 the instability region is above and on the left hand side of the presented curve. In Figures 4.12 and 4.13 stability and instability regions are on the left hand and right hand side of the curve, respectively. This being said, we analyze the Figures 4.10 to 4.13 one by one.

The stability curves for M1 (LDPE) are depicted in Figures 4.10 and 4.11. The results show that the influence of the temperature increases if we increase the air velocity, which means increased cooling. Already natural cooling ($v_a = 0$ m/s) improves the stability for M1 (LDPE). If $v_a = 15$ m/s, the instability region becomes significantly smaller compared to the instability region for the isothermal case.

From Figure 4.10, we conclude that for relatively small Draw ratios Dr , $20 < Dr < 30$, cooling shifts the stability curve a bit to the left, i.e., the instability region starts at lower Dr . We do not consider this change as being significant, especially when compared to the shift of the curve for the higher Dr -values. Higher Dr -values are more important for the process because the higher Dr , the higher the operation speed we can access. And for those high operation speed values, a drop of the temperature diminishes the instability region. These results are confirmed by Figure 4.11, where the situation is considered for wider range of Deborah numbers. For very small Deborah numbers, $De < 0.0072$, the instability region is wide, the critical values of Dr are low, and cooling does not seem to help. With increase of De , the temperature influence becomes significant. According to the prediction of our temperature-dependent model with $v_a = 15$ m/s: for De changing from 0.0072 to 0.012, the stable region can be reached for low and then again for high values of Dr ; for $De > 0.012$, the process is stable for all Dr .

The results for M2 (LLDPE) are presented in Figures 4.12 and 4.13. In contrast to M1 (LDPE), cooling does not improve stability. It does just the opposite, it makes the instability region wider,

as can be seen in Figure 4.12. Results presented in Figure 4.13 additionally indicate two ranges Deborah numbers: $De < 0.02$ with a visible negative effect of cooling; $De > 0.02$ with no effect of cooling.

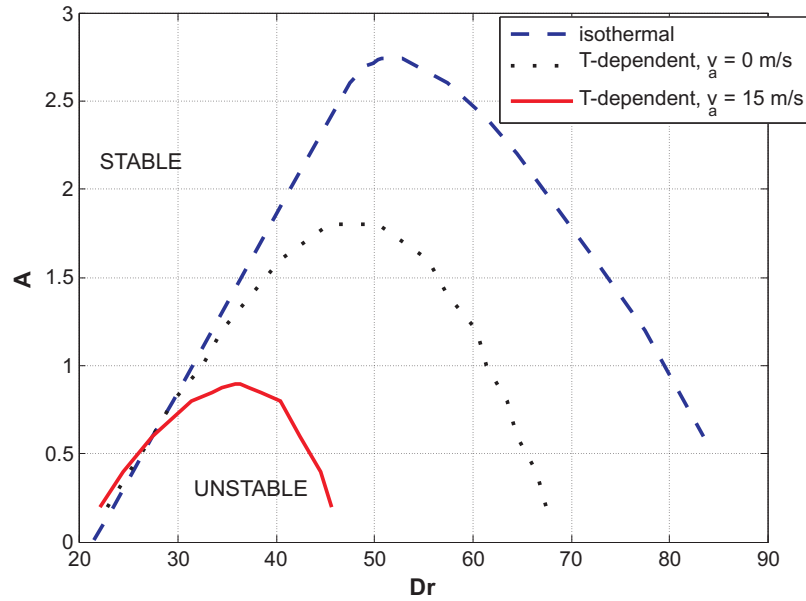


Figure 4.10: Temperature influence on the stability curve resulted from PTT model simulations for the material M1 (LDPE), $\varepsilon = 0.01$, $De = 0.01$.

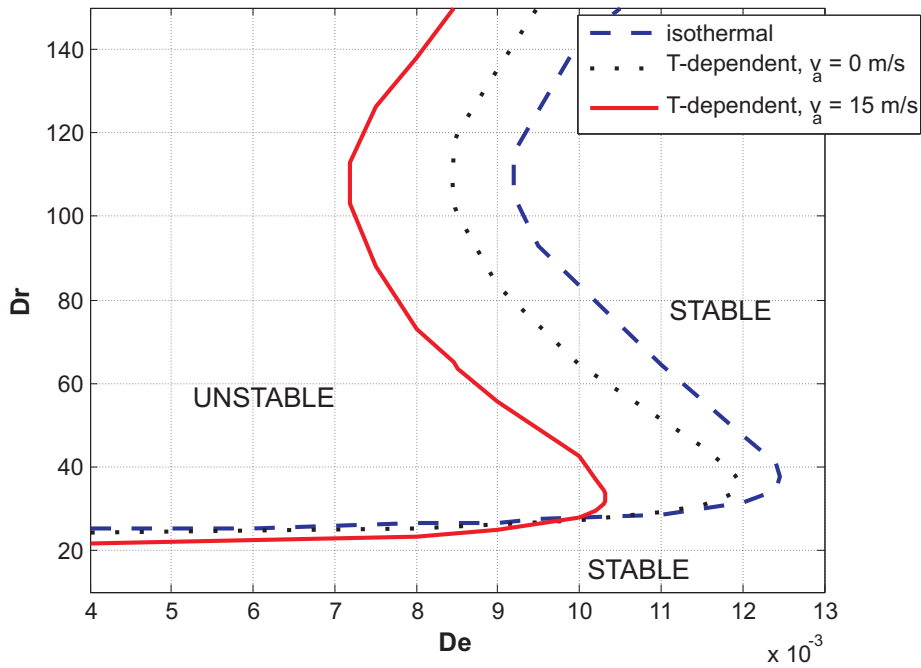


Figure 4.11: Temperature influence on the stability curve resulted from PTT model for M1 (LDPE), $\varepsilon = 0.01$, $A = 0.6$.

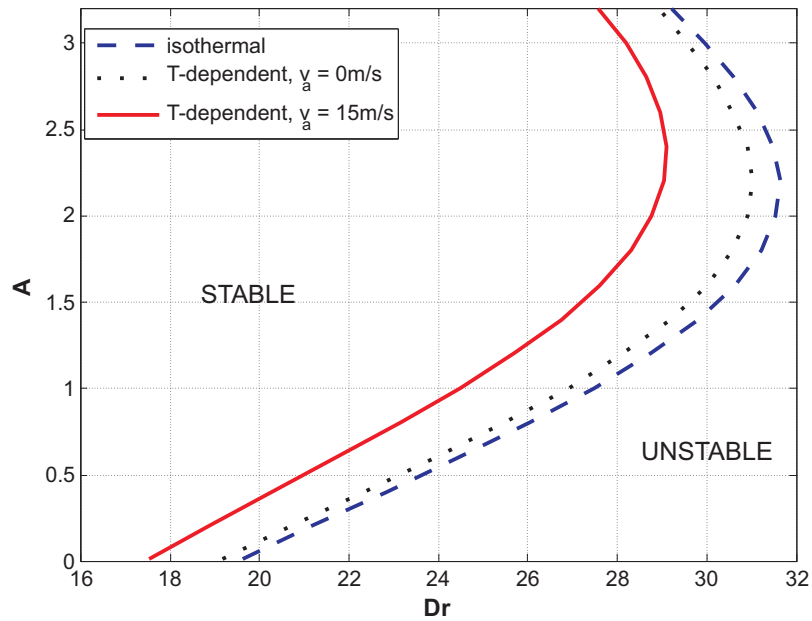


Figure 4.12: Temperature influence on the stability curve resulted from PTT model simulations for the material M2 (LLDPE), $\varepsilon = 0.1$, $D_e = 0.01$.

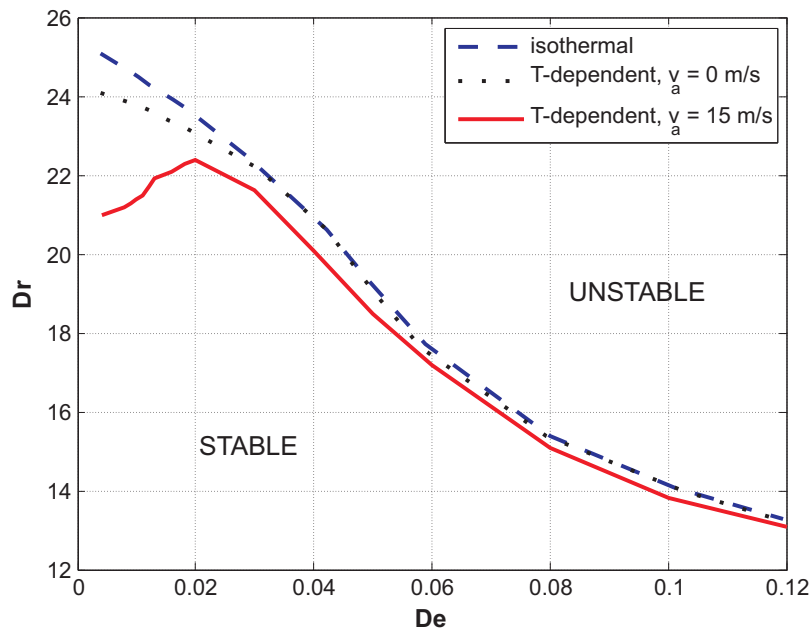


Figure 4.13: Temperature influence on the stability curve resulted from PTT model for M2 (LLDPE), $\varepsilon = 0.1$, $A = 0.6$.

Modified Giesekus

In this section we present the results of simulations of non-isothermal film casting with the modified Giesekus model. The materials and conditions are the same as in the previous section. For each of the materials, M1 (LDPE) and M2 (LLDPE), we build two diagrams picturing their stability behavior, i.e., one of Aspect ratio *versus* Draw ratio, A *vs* Dr , for a fixed Deborah number $De = 0.01$ (Figures 4.14 and 4.16), and one of Draw ratio *versus* Deborah number, Dr *vs* De , for a fixed $A = 0.6$ (Figures 4.15 and 4.17). Each diagram contains three critical stability curves obtained under isothermal conditions, non-isothermal conditions with natural cooling ($v_a = 0$ m/s), and non-isothermal conditions with additional cooling ($v_a = 15$ m/s).

We first consider the results for the material M1 (LDPE). As in the case of the PTT model, the resulting critical curves plotted in Figure 4.14 and 4.15 clearly indicate a temperature influence on the stability outcome. Next, by comparing PTT and Giesekus results for M1 (LDPE), we notice similarities and differences. The " A *vs* Dr " diagram, in Figure 4.14, is comparable to the one obtained from the PTT model, see Figure 4.10. The shape of the curves is similar for both models. The stability curves of both models show that for some fixed A , increased drawing leads to change of the stable zone into an unstable and then to a stable one again. In case of the modified Giesekus simulations of M1 (LDPE), the unstable zone is narrower than the one obtained from PTT. Also cooling shifts the unstable zone to the left and makes it even more narrow. In contrast to PTT, the top of the stability curve does not become lower. To our opinion, the results of the modified Giesekus model are more consistent than the ones of PTT. For instance, all three stability curves show more or less the same values of the critical Draw ratio for A close to zero. That seems logical in relation to film casting, as $A \sim 0$ means a small drawing distance and thus little influence of cooling. This is not reflected by the results of the PTT model.

In Figure 4.15, we show the " Dr *vs* De " diagram build for M1 (LDPE). It is quite different from the one based on the PTT model results, see Figure 4.11. The unstable zone predicted by the modified Giesekus model is much smaller than the one predicted by PTT. According to the PTT model results, for $De \leq 0.007$ the unstable zone starts at about $Dr = 20$ and cannot be overcome. The results of the modified Giesekus model indicate that much higher values of Dr than 20 can be reached.

We look now at the stability maps for material M2 (LLDPE), see Figures 4.16 and 4.17. Analyzing both plots, we conclude that cooling has a big impact on the resulting prediction of the critical Draw ratio. Generally, one assumes that additional cooling systematically postpones draw resonance. Yet, our numerical results show the opposite for a certain range of Deborah numbers De . Indeed, the plot of " Dr *vs* De ", given in Figure 4.17, shows the existence of three different regimes depending on the value of the Deborah number. In the first regime, $De < 0.035$, cooling has a negative impact on the stability; in the second regime, $0.035 < De < 0.07$, where the cooling has a positive effect and stability zone becomes wider; in the third regime, $De > 0.07$, cooling makes no difference. The difference between the critical curves obtained under isothermal and non-isothermal condition for $De < 0.035$ may seem insignificant at first. But all these three

curves are steeply descending. Thus, the small shift of the curve to the left or to the right yields big difference in the results.

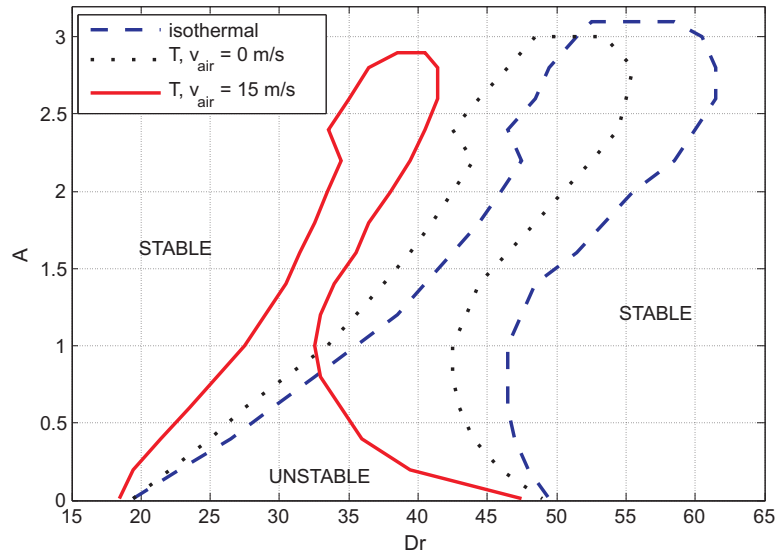


Figure 4.14: LDPE (Giesekus with $a = 0.01$, $N_0 = 100$ $De = 0.01$): Temperature influence on the stability curve.

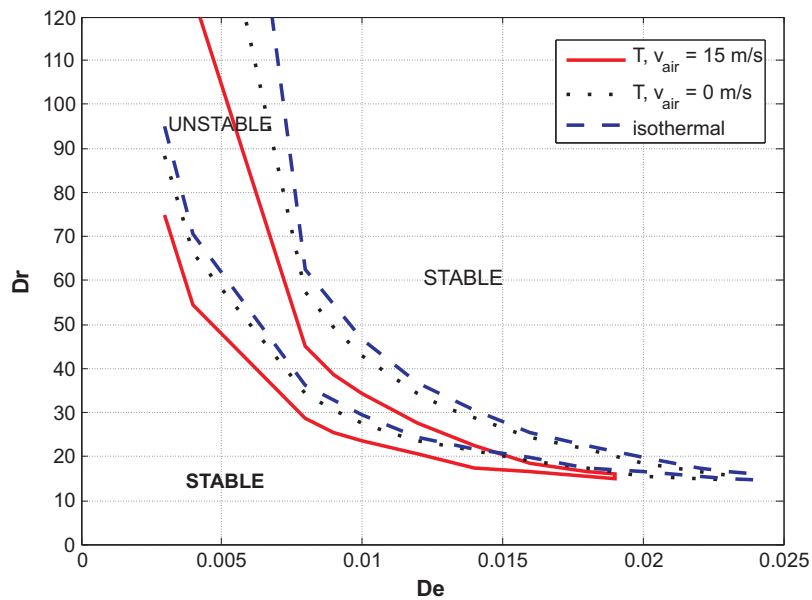


Figure 4.15: LDPE (Giesekus with $a = 0.01$, $N_0 = 100$ $A = 0.6$): Temperature influence on the stability curve.

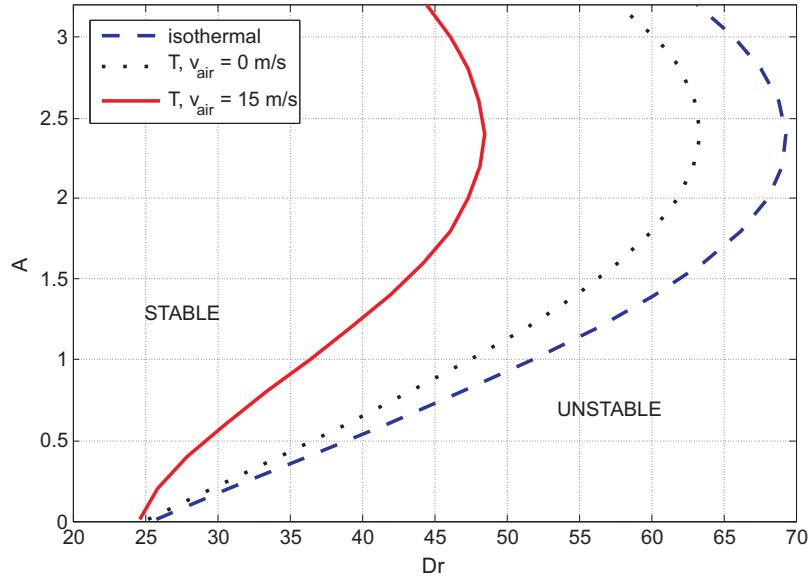


Figure 4.16: LLDPE (Giesekus with $a = 0.2$, $N_0 = 32$ $De = 0.01$): Temperature influence on the stability curve.

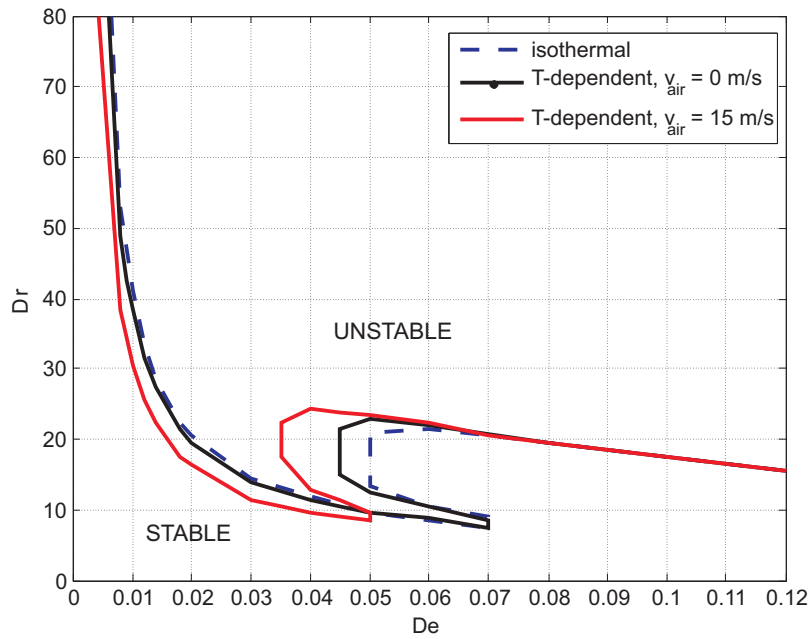


Figure 4.17: LLDPE (Giesekus with $a = 0.2$, $N_0 = 35$, $A = 0.6$): Temperature influence on the stability curve.

4.3.6 Comparison with the Experimental Data

Material

The material used for the film casting experiments is a Dow polyolefin plastomer AFFINITY™ EG 8200. The various material properties of this resin are reported in [61]. We briefly summarize the information about the material properties of this resin in Table 4.2. The melt index (MI) is determined according to the ASTM D1238 method (190 C, 2.16 kg) and the solid density according to the ASTM D792 method. The molecular mass distribution data are obtained using a Waters 150C instrument via both conventional and triple detector gel permeation chromatography (GPC). The Mn data are accurate within 8%, the Mw data within 4%, and the Mz data within 10%.

Table 4.2: Material properties of AFFINITY™ EG8200.

Resin	Molecular structure	Melt index (g/10 min)	Mw (g/mol)	Mn (g/mol)	Mz (g/mol)	Mw/Mn	Solid density
AFFINITY™ EG 8200	Substantially linear, homogeneously branched ethylene polymer	5	70860	34030	111100	2.08	0.87

Experimental Conditions

The film casting experiments are run on a Black Clawson 8.9-cm film coater fitted with a 30 L/D extruder with a 150 Hp drive. The die is a 76.2-cm Cloeren with a 0.635 mm die gap and a Cloeren 3-layer feedblock. The melt temperature is controlled in the range from 226 to 245°C. The air gaps from 14.5 to 38 cm are applied. Cooling is achieved by using quenched air with the velocity of 15m/s. The extrusion output is taken such that the initial velocity is 0.1 m/s. At a start of the measurements the take-up speed is such that the film is stable. The drawdown is measured as the speed where the polymer rips off the die. In order to determine the onset of draw resonance, the line speed is increased with increments of 6 m/min from the starting speed until the width of the film begins to oscillate with the amplitude larger than ± 1.3 cm. The line speed at which the oscillations occur is refined by lowering the line speed until the film stabilizes again and increasing line speed again with smaller increments.

Input Conditions

To simulate experimental data with our model, values for three parameters are needed, namely, value for one characteristic time λ , and the values for the modified Giesekus coefficients: the molecular mobility parameter α and finite chain extensibility parameter N_0 . The complete method

to obtain the modified Giesekus model parameters (as well as parameters of any other constitutive model) is discussed in Chapter 3. However, the parameters of the modified Giesekus model for AFFINITY EG8200 have been found and justified by *Doufas* [61]. Therefore, for our simulations we take the values given in [61]: $\alpha = 0.195$, and $N_0 = 35$. To find an appropriate value for the relaxation time, we recalculated the discrete relaxation spectrum from the complex shear modulus, extrapolated at the extrusion temperature by the time-temperature superposition principle. For that we used the NLREG routine based on the method of *Honerkamp and Weese*, [92]. Then, an average relaxation time is deduced from the spectrum using the following equation:

$$\lambda_0 = \frac{\sum_{i=1}^n G_i \lambda_i^2}{\sum_{i=1}^n G_i \lambda_i}. \quad (4.75)$$

The resulting input conditions used in numerical simulations as well as both values for the critical Draw Ratio, experimental and predicted, are collected in Table 4.3.

Table 4.3: Experimentally measured and numerically predicted critical Draw Ratios. Input parameters for simulations deduced from experimental conditions.

	Run 1	Run 2	Run 3	Run 4	Run 5	Run 6	Run 7
Extrusion Temperature, °C	245	231	231	226	245	229	231
Aspect Ratio (A)	0.47	0.475	0.58	0.75	0.75	0.92	1.25
Relaxation time (λ_0)	0.0185	0.0230	0.0247	0.0251	0.0182	0.0224	0.0228
Deborah Number (De)	0.013	0.016	0.014	0.011	0.008	0.008	0.006
Critical DR (experiments)	21.6	17.9	19.7	25.8	33.6	44.7	58.6
Critical DR (Giesekus with T)	22	17.5	22	30.5	39	44.5	61
Critical DR (Giesekus iso)	28.5	23.1	28.5	41.5	55	60.5	93.5
Critical DR (PTT with T)	21.2	21.5	22.7	22.2	21.5	22.5	23.5
Critical DR (PTT iso)	23.2	22.5	23.5	24.5	25.5	26.3	29

Results

The visualization of the results is given in Figure 4.18, where the critical Draw ratio predicted by the modified Giesekus and the PTT models is plotted versus experimentally measured critical Draw ratios. We conclude that the modified Giesekus model proves to be suitable for modeling the flow behavior of the resin studied here. The experiments confirm the strength of our model, since we did not tune model parameters in our simulations, but we took values from an independent source. Another important conclusion is that the modified Giesekus model with the non-isothermal condition gives much better prediction than with the isothermal one. The isothermal modified Giesekus model overestimates reality by 50 %. Thus, cooling effects cannot be neglected in the stability studies. The PTT model is not capable of grasping the experimental results neither with the isothermal, nor with non-isothermal condition; the simulation results of the PTT model are far from reality. In Figure 4.19, we show the exact experimentally detected draw resonance data (Table 4.3) on the "Dr vs De" stability maps. The left plot describes the modified Giesekus model results,

and the right plot describes the PTT model results. The values of critical Draw ratio (Dr) that were measured experimentally are depicted by dots. The experimental values were obtained with different values of the Aspect ratio (A). The stability maps are built for the single value of Aspect ratio, $A = 0.6$. Thus, we should be careful with a direct quantitative comparison between the simulated results given in the maps and the experiments. However, even a qualitative comparison shows that the modified Giesekus model is far better capable of predicting the sharp increase of the critical Draw ratio as the Deborah number decreases than the PTT model. Such effect is not captured by the neither by the PTT model, nor by the upper convected Maxwell model, see Figure 4.7.

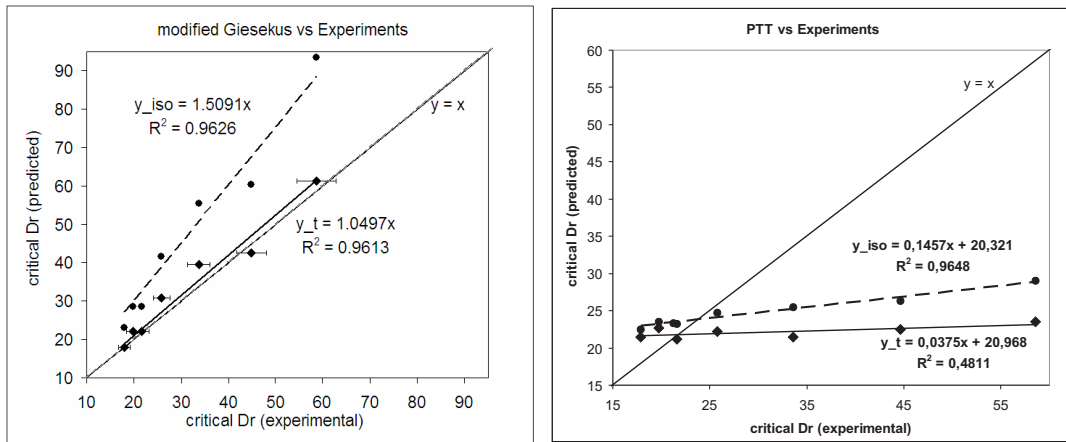


Figure 4.18: Prediction given by the modified Giesekus model (left) and PTT model (right) versus experimental data: the x-coordinate of every data point in a scatter indicates the measured value of the critical Dr (draw ratio) and the y-coordinate indicates the predicted value of the critical Dr for the same experiment. The filled dark circles denote results of the correspondent isothermal model and the filled dark diamonds are the ones of temperature dependent model. The regression lines indicate quality of the prediction. The closer the line is to $y = x$, the better the prediction.

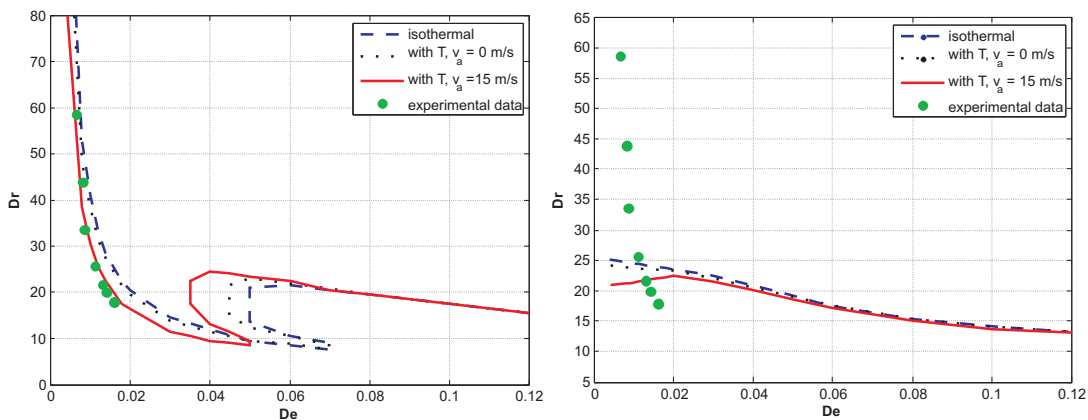


Figure 4.19: Relating the stability maps given by the modified Giesekus (left) and PTT (right) models to the experimental data. Experimental data are obtained for the values of A ranging from 0.47 to 1.25, while the simulations are performed for $A = 0.6$. Therefore, the presented comparison is only qualitative.

4.4 Conclusions

We validated our method against literature results for the isothermal Newtonian and isothermal UCM constitutive models and observed perfect agreement. Results of our numerical simulations show that the temperature influence on the stability is significant and cannot be excluded from analysis. Moreover, the validation against available experimental data for casting LLDPE resin shows that the non-isothermal modified Giesekus model gives good prediction, both qualitative and quantitative, without adjusting model parameters.

Appendix C

C1 Temperature Analysis

The temperature evolution is given by the convection equation

$$\frac{\partial T}{\partial t} + u \frac{\partial T}{\partial x} = -\frac{2h_t}{\rho C_p e} (T - T_a), \quad (\text{C-1})$$

where T is the absolute temperature of a polymer flow ($[T] = [K]$); T_a is the temperature of the surrounding air around a polymer flow ($[T_a] = [K]$). In (C-1) ρ is the density of the polymer ($[\rho] = \left[\frac{kg}{m^3}\right]$), which is taken independent of temperature; C_p is the heat capacity of the polymer ($[C_p] = \left[\frac{J}{kgK}\right]$); h_t is the heat transfer coefficient that consists of two terms:

$$h_t = h_f + h_{nat}. \quad (\text{C-2})$$

The term h_f is due to forced convection and h_{nat} is due to natural convection of heat ($[h_t] = \left[\frac{kg}{s^3K}\right]$). Heat transfer due to radiation and heat dissipation are assumed negligible. For h_f and h_{nat} , we use the following relations

$$h_f = \frac{0.66k_a}{x} \left(\frac{C_{pa}\eta_a}{k_a} \right)^{1/3} \left(\frac{xv}{\nu_a} \right)^{1/2}, \quad (\text{C-3})$$

$$h_{nat} = \frac{Bk_a}{x} \left(\frac{gx^3 C_{pa}\rho_a (T - T_a)}{\nu_a k_a T_a} \right)^p. \quad (\text{C-4})$$

The heat capacity C_p depends linearly on the temperature of the polymer

$$C_p = 969.9 + 3.7T. \quad (\text{C-5})$$

In the expressions for h_f and h_{nat} :

- $B = 0.56$ and $p = 0.25$.
- $k_a = 1.5207 \cdot 10^{-11} T_a^3 - 4.8574 \cdot 10^{-8} T_a^2 + 1.0184 \cdot 10^{-4} T_a - 3.9333 \cdot 10^{-4}$, $[k_a] = \left[\frac{W}{mK}\right] = \left[\frac{kgm}{s^3K}\right]$.

- $C_{pa} = -5 \cdot 10^{-7} T_a^3 + 10^{-3} T_a^2 - 0.4139 T_a + 1052$, $[C_{pa}] = \left[\frac{J}{kgK} \right]$.
- $\rho_a = \frac{360.77819}{T_a}$, $[\rho_a] = \left[\frac{kg}{m^3} \right]$.
- $\nu_a = -1.1555 \cdot 10^{-14} T_a^3 + 9.5728 \cdot 10^{-11} T_a^2 + 3.7604 \cdot 10^{-8} T_a - 3.4484 \cdot 10^{-6}$,
 $[\nu_a] = \left[\frac{m^2}{s} \right]$.
- $\eta_a = \nu_a \rho_a$, $[\eta_a] = \left[\frac{kg}{ms} \right]$.
- $v = v_a + u$, with v_a being the local air velocity. As a first approximation we take $v_a = 0$, and, thus, v is equal to u , the local velocity of the flow.

By substituting (C-3) and (C-4) into (C-1) and dividing by u , we get

$$\begin{aligned} \frac{1}{u} \frac{\partial T}{\partial t} + \frac{\partial T}{\partial x} = & - \frac{1.32k_a}{\rho u e x} \left(\frac{C_{pa} \eta_a}{k_a} \right)^{1/3} \left(\frac{xv}{\nu_a} \right)^{1/2} \frac{T - T_a}{C_p(T)} \\ & - \frac{2Bk_a}{\rho u e x} \left(\frac{g x^3 C_{pa} \rho_a}{\nu_a k_a T_a} \right)^p \frac{(T - T_a)^{1+p}}{C_p(T)}. \end{aligned} \quad (C-6)$$

We scale the variables as follows

$$\bar{T} = \frac{T}{T_0}, \quad \bar{x} = \frac{x}{X}, \quad \bar{u} = \frac{u}{u_0}, \quad \bar{e} = \frac{e}{e_0}. \quad (C-7)$$

For $C_p(T)$ this leads to a linear relation

$$C_p = a + b\bar{T}, \quad (C-8)$$

with $a = 969.9$ and $b = 3.7T_0$. After scaling and omitting bars, temperature equation (??) takes the form

$$\frac{1}{u} \frac{\partial T}{\partial t} + \frac{\partial T}{\partial x} = - \frac{V_1}{a + bT} \left(T - \frac{T_a}{T_0} \right) - \frac{V_2}{a + bT} \left(T - \frac{T_a}{T_0} \right)^{1+p}, \quad (C-9)$$

where

$$V_1(T_a, u, e; x) = \frac{1.32k_a}{\rho u_0 e_0 u e x} \left(\frac{C_{pa} \eta_a}{k_a} \right)^{1/3} \left(\frac{Xx(u_0 u + v_a)}{\nu_a} \right)^{1/2} \quad (C-10)$$

$$V_2(T_a, u, e; x) = \frac{2Bk_a}{\rho u_0 e_0 u e x} \left(\frac{g X^3 x^3 C_{pa} \rho_a}{\nu_a k_a T_r} \right)^p. \quad (C-11)$$

C1.1 Coefficients Analysis

The dimensionless equation (C-9) represents the temperature evolution in the film casting process. Before using it further in our model, however, we provide some analysis, to prove that we can neglect the time derivative in this equation.

Let us look first at the behavior of the dimensionless coefficients V_1 and V_2 in equation (C-9) under the condition that the air velocity is equal to zero ($v_a = 0$).

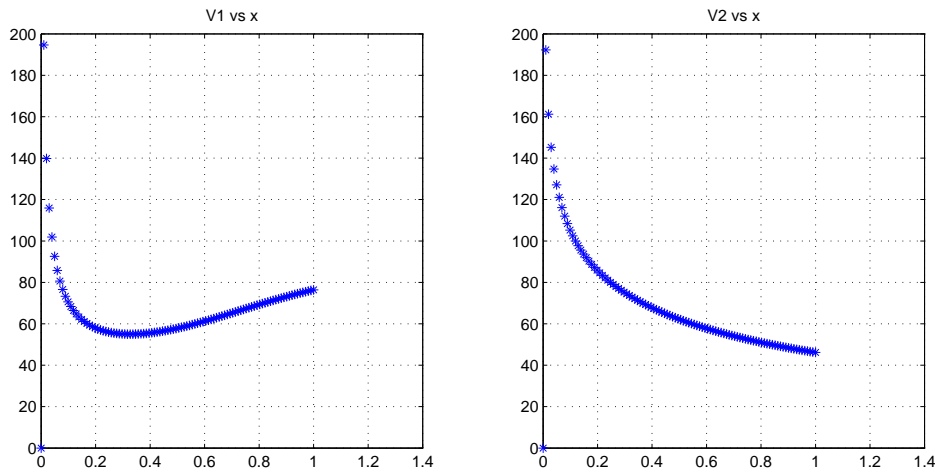


Figure C.1: Behavior of the coefficient functions V_1 and V_2 . Air velocity is taken to be zero.

In Figure C.1, the left hand side represents V_1 , and right hand side represents V_2 . The values of V_1 and V_2 are at the vertical axis, and the horizontal axis represents x . Almost on the whole interval $(0, 1)$ both functions are of the order 10, except for a small intervals $(0, 0.04)$ for V_1 and $(0, 0.1)$ for V_2 , where these coefficients become even of the order 10^2 .

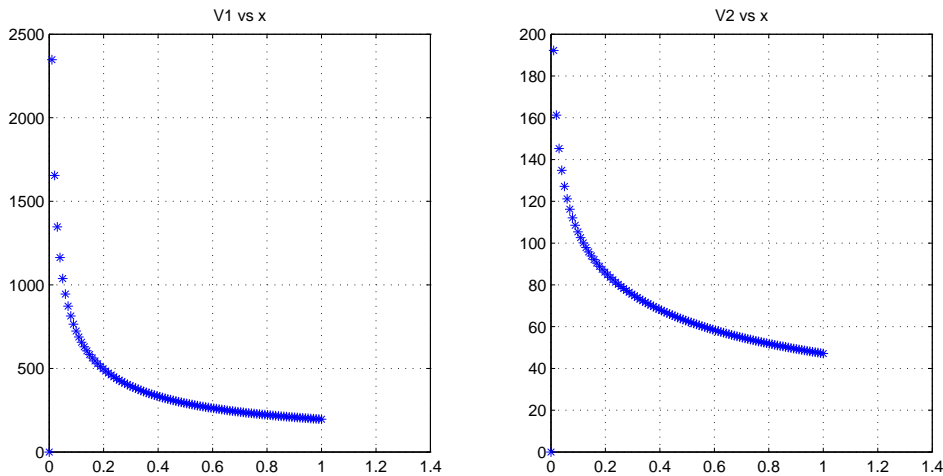


Figure C.2: Behavior of the coefficient functions V_1 and V_2 . Air velocity is taken to be 15m/s.

Correspondingly, Figure C.2 shows the behavior of V_1 and V_2 for the case if air velocity is taken to be 15m/s. Now, the behavior of V_2 remains the same because V_2 is derived from the natural convection term that is not influenced by v_a . In contrast, the forced convection related coefficient V_1 changes significantly and becomes of the order 10^2 for almost all $x \in (0, 1)$ (the minimal value is equal $2 \cdot 10^2$), except for a small interval $(0, 0.05)$, where V_1 is even of the order 10^3 .

Figure C.4 presents the coefficient $\frac{1}{u}$ of the time-derivative of the temperature. The values of this function were calculated for the same input Dr , as for which V_1 and V_2 were calculated. Figure

C.4 clearly shows that $\frac{1}{u}$ drops very rapidly; it is nearly 1 on the small interval $(0, 0.1)$, then, on the interval $(0.1, 0.6)$ is of the order 10^{-1} , and on $(0.6, 1)$ it is of the order 10^{-2} .

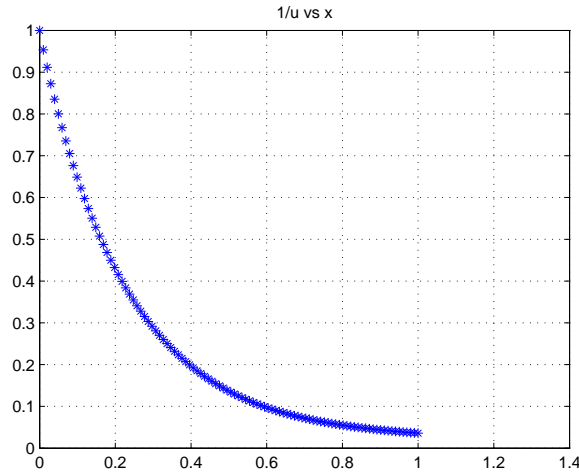


Figure C.3: Behavior of the coefficient function $\frac{1}{u}$.

C1.2 Conclusion

Coming back now to the temperature equation (C-9), we notice that

- coefficients V_1 and V_2 are of order 10 or 100, depending on the specified input conditions.
- coefficient of the space-derivative of temperature is equal to 1.
- coefficient of the time-derivative of temperature is of order $10^{-1} - 10^{-2}$.

On the base of this analysis we conclude that time-derivative of the temperature $\frac{\partial T}{\partial t}$ in Eq.(C-9) vanishes very quickly with respect to the other temperature terms. Thus, we decided to neglect it. That means that final temperature equation, we are going to consider further, does not contain time derivative of temperature

$$\frac{\partial T}{\partial x} = -V_1 \frac{T - T_r}{a + bT} - V_2 \frac{(T - T_r)^{1+p}}{a + bT}. \quad (\text{C-12})$$

Relation for the coefficients V_1 and V_2 are given by (C-10) and (C-11).

C2 An example of the modified Giesekus constitutive model parameters for LDPE material

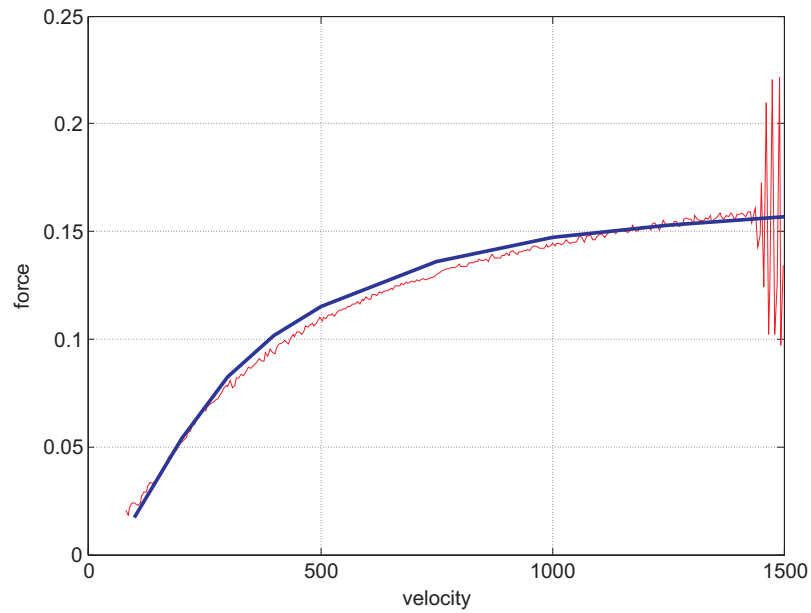


Figure C.4: The steady state Rheotens curve of LDPE material fitted with the numerical data obtained by simulating the modified Giesekus model. The fitting parameters are found to be $\alpha = 0.05$ and $N_0 = 90$.

CHAPTER FIVE

Conclusions

Draw resonance instability, which occurs in industrial polymer elongation processes, influences the quality of the end-product and narrows the process operating conditions. This instability is highly unwanted; therefore, knowledge gained from studies that can help to understand, predict, and avoid (or reduce) draw resonance is of great importance. A lot was done in this field already, which is reflected in the bibliography mentioned at the end of this thesis. Yet, still there are many open issues remaining. In this thesis, we try to cover some of them.

First of all, we consider a generic mathematical description applicable for polymer elongation process. This description results in a hyperbolic system of quasi-linear differential equations with two-point boundary conditions. We do not concentrate on a proof of the solvability of the steady state system, a boundary value problems for ordinary differential equations. Although such problems are not covered by general theory on existence and uniqueness, there exists a vast amount of mathematical proofs and numerical approaches for particular cases. Instead, we put efforts on analyzing the linearized system. We prove, without involving complex arguments, the invertibility of the differential operator that drives the linear system. Moreover, we prove that the inverse operator is compact, which in turn yields that the spectrum of the linearized hyperbolic system is discrete. In terms of the spectrum a criterium of stability/instability is derived. We also point at some difficulties that may arise when the spectrum is empty, so no relevant information on the stability can be obtained. The main conclusion from the task that we put on ourself for this part is that the approach adopted to treat draw resonance instabilities has a sound mathematical basis.

The second issue, addressed in this thesis, is a design of an implementation that yields fast and robust calculations of the spectrum and corresponding modes. Thus far, to our knowledge, implementations being both fast and robust are not achieved, nor presented in literature. We base our numerical routine on a modified Galerkin approach, using local basis functions and a novel way to incorporate the homogeneous boundary conditions. Validation on a couple of benchmark problems shows excellent performance of the proposed routine. We also conclude that the routine

developed yields a spectrum without spurious modes, in contrast to other methods used to determine spectra of hyperbolic systems. Furthermore, the calculation time of the complete spectrum with eigenmodes on a standard PC with one processor and 256 Mb of operational memory takes only a few seconds.

The next issue that we address is recognized in simulations of general polymer processes, not necessarily elongational. Namely, the constitutive and rheological parameters describing polymer characteristics are not known and hard to estimate. In this thesis we propose a measurement design to quantitatively estimate parameters in a constitutive model. We use the well-known Rheotens experiment that we operate at fixed velocities of the drawing wheels; the velocities are specified such that onset of draw resonance is observed. The recorded data of force-*versus*-time are analyzed by means of the Discrete Fourier Transformation resulting into peak process frequencies. From Fourier analysis of the experiments conducted for various resins, we conclude that: there is always a main peak frequency of force oscillations at draw resonance; this frequency is material dependent; thus, the main frequency value can be used for characterization.

In order to use the experimentally observed frequencies for parameter estimation, we need a model that describes the Rheotens experiment as we operate it. From this model, for given parameters, we determine the spectrum, and from the spectrum we determine the frequencies. From a sensitivity analysis we conclude that there are straightforward relations between the calculated frequencies and model parameters. Matching data from the simulations to data from the experiments, we determine the parameters of the constitutive model considered. We conclude that the procedure developed to find parameters is very effective and can be used on an operational level. We also conclude that draw resonance, induced in a controlled way, can be used in our favor.

Having a procedure to determine parameters, we can make a final step and apply these parameters in simulations of polymer elongation processes. In this thesis, as an example of application, we consider the process of casting of polymer films. The aim is to determine the process conditions that lead to draw resonance. In particular, we are interested in the effect of cooling on draw resonance and whether it can be reflected by the simulations. We present a number of stability maps obtained with and without temperature taken into account. Our conclusion is that the temperature essentially influences the predicted stability. Non-isothermality of the process can and must be taken into account in the modeling. In particular, the simulation tests with the modified Giesekus constitutive relations for linear low density polyethylene show a perfect match between the experimentally measured and the numerically predicted draw resonance.

Bibliography

- [1] Cristensen, R.E., *Extrusion Coating of Polypropylene*, SPEJ, **18**, 751, 1962.
- [2] Miller, J.C., *Swelling behavior in extrusion*, S.P.E. Trans. **3**, 134, 1963.
- [3] Petrie, C.J.S., Denn, M.M., *Instabilities in Polymer Processing*, AIChE J., **22**, 209, 1976.
- [4] Ishihara, H., Kase, S., *Studies on melt spinning. VI. Simulation of draw resonance using Newtonian and power law viscosities*, J. Appl. Polymer Sci. **20**, 169, 1976.
- [5] Denn, M.M., *Continuous Drawings of Liquids to form Fibers*, Ann. Rev. Fluid Mech., **12**, 365, 1980.
- [6] Kase, S., Matsuo, T., Yoshimoto, Y., *Theoretical Analysis of Melt Spinning. Part2: Surging Phenomena in Extrusion Casting of Plastic Films*, Seni Kikai Gakkaishi, **19**, 1966.
- [7] Pearson, J.R.A., Matovich, M.A., *Spinning a Molten Threadline: Stability*, Ind. Eng. Chem. Fundam. **8**, 605, 1969.
- [8] Fisher, R.J., Denn, M.M., *Finite-Amplitude Stability and Draw Resonance in Isothermal Melt Spinning*, Chem. Eng. Sci., **30**, 1129, 1975.
- [9] Ishihara, H., Kase, S., *Studies on melt spinning. V. Draw Resonance as a Limit Cycle*, J. Appl. Polymer Sci. **19**, 557, 1975.
- [10] Fisher, R.J., Denn, M.M., *A theory of isothermal melt spinning and draw resonance*, AIChE J. **22**, 236, 1976.
- [11] Hyun, J.C., *Theory of draw resonance: I. Newtonian fluids*, AIChE J. **24**, 418, 1978.
- [12] Hyun, J.C., *Theory of draw resonance: II. Power-law and Maxwell fluids*, AIChE J., **24**, 423, 1978.
- [13] Kase, S., Araki, M., *Studies on melt spinning. VIII. Transfer function approach*, J. Appl. Polym. Sci. **27**, 4439, 1982.
- [14] Beris, A.N., Liu, B., *Time Dependent Fiber Spinning Equations. 1. Analysis of the Mathematical Behaviour*, J. Non-Newtonian Fluid Mechanics, **26**, 341, 1988.

- [15] Liu, B., Beris, A.N., *Time Dependent Fiber Spinning Equations. 2. Analysis of the Stability of Numerical Approximations*, J. Non-Newtonian Fluid Mechanics, **26**, 363, 1988.
- [16] Bechtel, S.E., Cao, J.Z., Forest, M.G., *Practical application of a higher order perturbation theory for slender viscoelastic jets and fibers*, J. Non-Newt. Fluid Mech. **41**, 201, 1992.
- [17] Kim, B.M., Hyun, J.C., Oh, J.S., Lee, S.J., *Kinematic waves in the isothermal melt spinning of Newtonian fluids*, AIChE J. **42**, 3164, 1996.
- [79] Jung, H.W., Hyun, J.C., *Stability of isothermal spinning of viscoelastic fluids*, Korean J. Chem. Eng. **16**, 325, 1999.
- [19] Doufas, A.K., McHugh, A.J., *Two-dimensional Simulation of Melt Spinning with a Microstructural Model for Flow-induced Crystallization*, J.Rheology, **45**(4), 855, 2001.
- [20] Doufas, A.K., McHugh, A.J., Miller, C., *Simulation of Melt Spinning Including Flow-induced Crystallization. Part I. Model Development and Predictions*, J. Non-Newtonian Fluid Mech. **92**, 27, 2000.
- [21] Doufas, A.K., McHugh, A.J., Miller, C., Immaneni, A., *Simulation of Melt Spinning Including Flow-induced Crystallization. Part II. Quantitative comparisons with industrial spinline data*, J. Non-Newtonian Fluid Mech. **92**, 81, 2000.
- [22] Hagen, T., Renardy, M., *Eigenvalue Asymptotics in Non-isothermal Elongational Flow*, J. Mathematical Analysis and Applications, **252**, 431, 2000.
- [23] Hagen, T., *On the Semigroup of Linearized Forced Elongation*, Applied Mathematics Letters, **18**, 667, 2005.
- [24] Hagen, T., Renardy, M., *Eigenvalue Asymptotics in Non-isothermal Elongational Flow*, J. Mathematical Analysis and Applications, **252**, 431, 2000.
- [25] Agassant, J.-F., Avenas, P., Sergent, J.-Ph., Carreau, P.J., *Polymer Processing. Principles and Modelling*, Hanser Publishers, Munich, 1991.
- [26] Denn, M.M., *Polymer Melt Processing. Foundations in Fluid Mechanics and Heat Transfer*, Cambridge University Press, New York, 2008.
- [27] Courant, R., Hilbert, D., *Methods of Mathematical Physics. Volume II: Partial Differential Equations*, Interscience Publishers, New York - London, 1962.
- [28] Tayler, A.B., *Mathematical Models in Applied Mechanics*, Clarendon Press, Oxford, 1986.
- [29] Forest, M.G., Wang, Q., *Change-of-Type Behaviour in Viscoelastic Slender Jet Models*, Theoretical and Computational Fluid Dynamics, **2**, 1, 1990.
- [30] Betchel, S.E., Forest, M.G., Wang, Q., Zhou, H., *Free Surface Viscoelastic and Liquid Crystalline Polymer Fibers and Jets*, Advances in the Flow and Rheology of Non-Newtonian Fluids, Parts A and B, Elsevier Science, 1069, 1999.

- [31] Hagen, T., *Elongational Flows in Polymer Processing*, Thesis, Virginia Polytechnic Institute and State University, 1998.
- [32] Bernfeld, S.R., Lakshmikantham, V., *An Introduction to Nonlinear Boundary Value Problems*, Mathematics in Science and Engineering 109, Academic Press, New York, 1974.
- [33] Ringrose, J.R., *Compact Non-Self-Adjoint Operators*, Van Nostrand Reinhold Company, London, 1971.
- [34] Keller, H.B., *Numerical Methods for Two-Point Boundary-Value Problems*, Dover, New York, 1992.
- [35] Kramer, M.E., *Aspects of Solving Non-linear Boundary Value Problems Numerically*, Thesis, Eindhoven University of Technology, 1992.
- [36] Ascher, U.M., Mattheij, R.M.M., Russell, R.D., *Numerical Solution of Boundary Value Problems for Ordinary Differential Equations*, Classics in Applied Mathematics 13, SIAM, Philadelphia, 1995.
- [37] Ascher, U.M., Petzold, L.R., *Computer Methods for Ordinary Differential Equations and Differential Algebraic Equations*, SIAM, Philadelphia, 1998.
- [38] Quarteroni, A., Sacco, R., Saleri, F., *Numerical Mathematics*, Texts in applied Mathematics 37, Springer, New York, 2000.
- [39] Mattheij, R.M.M., Molenaar, J., *Ordinary Differential Equations in Theory and Practice*, Classics in Applied Mathematics 43, SIAM, Philadelphia, 2002.
- [40] Hagen, T., Langwallner, B., *A Numerical Study on the Suppression of Draw Resonance by Inertia*, *Z. Angew. Math. Mech.*, **86** (1), 63, 2006 / DOI 10.1002/zamm.200410225.
- [41] Meissner, J., *Anordnung zum Bestimmen des deformationsmechanischen Verhaltens von teigigen Stoffen, Pasten und Schmelzen*, Deutsche Offenlegungsschrift DOS 1904079, 1969.
- [42] Meissner, J., *Dehnungsverhalten von Polyathylen-Schmelzen*, *Rheol. Acta* **10**, 230, 1971.
- [43] Meissner, J., *Basic parameters, melt rheology, processing and end-use properties of three similar low density polyethylene samples*, *Pure Appl. Chem.* **42**, 553, 1975.
- [44] White, J. L., Yamane, H., *A collaborative study of the stability of extrusion, melt spinning and tubular film extrusion of some high-, low-, and linear-low density polyethylene samples*, *Pure Appl. Chem.* **59**, 193, 1987.
- [45] Field, G. J., Mimic, P., Bhattacharya, S. N., *Melt strength and film bubble instability of LLDPE/LDPE blends*, *Polym. Int.* **48**, 461, 1998.
- [46] La Mantia, F. P., Acierno, D., *Influence of molecular structure on the melt strength and extensibility of polyethylenes*, *Polym. Eng. Sci.* **25**, 279, 1985.

- [47] Ghijsels, A., Ente, J. J. S. M., Raadsen, J. *Melt strength behavior of PE and its relation to bubble stability in film blowing*, IPP **5**, 284, 1990.
- [48] Ghijsels, A., Ente, J. J. S. M., Raadsen, J., *Melt strength behavior of polyethylene blends*, IPP **7**, 44, 1992.
- [49] Ghijsels, A., De Clippeleir, J., *Melt strength behaviour of polypropylenes*, IPP **9**, 252, 1994.
- [50] Sampers, J., Leblanc, P. J. R., *An experimental and theoretical study of the effect of the elongational history on the dynamics of isothermal melt spinning*, J. Non-Newtonian Fluid Mech. **30**, 325, 1988.
- [51] Wagner, M. H., Schulze, V., Goettfert, A., *Rheotens-mastercurves and drawability of polymer melts*, Polym. Eng. Sci. **36**, 925, 1996.
- [52] Bernnat, A., Wagner, M. H., Chai, C.K., *Assesment of LDPE melt strength by use of Rheotens Mastercurves*, Intern. Polymer Processing, XV, **3**, 268, 2000.
- [53] Bernnat, A., *Polymer Melt Rheology and the Rheotens Test*, Ph.D. thesis, Institut für Kunststofftechnologie, Universität Stuttgart, 2001.
- [54] Laun, H. M., Schuch, H., *Transient elongational viscosities and drawability of polymer melts*, J. Rheol. **33**, 119, 1989.
- [55] Rauschenberger, V., Laun, H. M., *A recursive model for the Rheotens tests*, J. Rheol. **41**, 719, 1997.
- [56] Fulchiron, R., Revenu, P., Kim, B. S., Carrot, C., Guillet, J., *Extrudate swell and isothermal melt spinning analysis of linear low density polyethylene using the Wagner constitutive equation*, J. Non-Newtonian Fluid Mech. **69**, 113, 1997.
- [57] Wagner, M. H., Bernnat, A., Schulze, V., *The rheology of the rheotens test*, J. Rheol. **42**, 917, 1998.
- [58] Wagner, M. H., Bastian, H., Bernnat, A., Kurzbeck, S., Chai, C. K., *Determination of elongational viscosity of polymer melts by RME and rheotens experiments*, Rheol. Acta **41**, 316, 2002.
- [59] Matsui, T., *Air drag on a continuous filament in melt spinning*, Trans. Soc. Rheol. **20**, 465, 1976.
- [60] Gould, J., Smith, F.S., , J. Text. Inst., **1**, 38, 1980.
- [61] Doufas, A. K., *Analysis of the rheotens experiment with viscoelastic constitutive equations for probing extensional rheology of polymer melts*, J. Rheol. **50** (5), 749, 2006.
- [62] Cohen, A., *A Pade Approximation to the Inverse Langevine Function*, Rheol. Acta, **30**, 270, 1991.

- [63] Kennedy, J., Eberhart, R.C., *Particle Swarm Optimization*, Proc. IEEE Int. Conf. on Neural Networks, Vol.IV, 1942, Piscataway, NJ, 1995.
- [64] Kennedy, J., Eberhart, R.C., *Swarm Intelligence*, Morgan Kaufmann, 2001.
- [65] Claracq, J., *Private communication*.
- [66] Marsden, J., McCracken, M., *Hopf Bifurcation and Its Applications*, Springer, 1976.
- [67] Strogatz, S.H., *Nonlinear Dynamics and Chaos*, Perseus, Cambridge, 1994.
- [68] Kuznetsov, Y.A., *Elements of Applied Bifurcation Theory*, Springer-Verlag, New York, 2004.
- [69] Demay, Y., *Instabilités D'étirage et Bifurcation de Hopf*, Thesis, Universite de Nice, France, 1983.
- [70] Silagy, D., Demay, Y., and Agassant, J-F., *Study of the Stability of the Film Casting Process*, Polymer Engineering and Science, **36** (21), 2614, 1996.
- [71] Silagy, D., Demay, Y., and Agassant, J-F., *Stationary and Stability Analysis of the Film Casting Process*, J. Non-Newtonian Fluid Mech., **79**, 563, 1998.
- [72] Anturkar, N.R., Co, A., *Draw Resonance in Film Casting of Viscoelastic Fluids: A linear Stability Analysis*, J. Non-Newtonian Fluid Mech., **28**, 287, 1988.
- [73] Lee, J.S., and Hyun, J.C., *Nonlinear Dynamics and Stability of Film Casting Process*, Korea-Australia Rheology Journal, **13** (4), 179, 2001.
- [74] Lee, J.S., Jung, H.W., and Hyun J.C., *Stabilization of Film Casting by an Encapsulation Extrusion Method*, J. Non-Newtonian Fluid Mech., **117**, 109, 2003.
- [75] Iyengar, V.R., Co, A., *Film Casting of a Modified Giesekus fluid: a Steady-State Analysis*, J. Non-Newtonian Fluid Mech., **48**, 1, 1993.
- [76] Iyengar, V.R., Co, A., *Film Casting of a Modified Giesekus fluid: Stability Analysis*, Chemical Engineering Science, **51** (9), 1417, 1996.
- [77] Pis-Lopez, M.E., Co, A., *Multilayer Film Casting of modifyied Giesekus fluids. Part1. Steady-State Analysis*, Journal of Non-Newtonian Fluid Mechanics, **66**, 71, 1996.
- [78] Pis-Lopez, M.E., Co, A., *Multilayer Film Casting of modifyied Giesekus fluids. Part2. Linear Stability Analysis*, Journal of Non-Newtonian Fluid Mechanics, **66**, 95, 1996.
- [79] Jung, H.W., Choi, S.M., and Hyun, J.C., *Approximate Method for Determining the Stability of the Film Casting Process*, AIChE Journal, **45** (5), 1157, 1996.
- [80] Lee, J.S., Jung, H.W., Hyun J.C., *Frequency Responce of Film Casting Process*, Korea-Australia Rheology Journal, **15** (2), 91, 2003.

- [81] Sologoub, C., Demay, Y., Agassant, J.F., *Cast Film problem: A Non Isothermal Investigation*, Intern. Polymer Processing XVIII, **1**, 80, Hanser Publishers, Munich, 2003.
- [82] Agassant, J.F., Demay, Y., Sologoub, C., Silagy, D., *Cast Film Extrusion. An Overview of Experimental and Theoretical Approaches*, Intern. Polymer Processing XX, **2**, 136, Hanser Publishers, Munich, 2005.
- [83] Sologoub, C., Demay, Y., Agassant, J.F., *Non-isothermal Viscoelastic Numerical Model of the Cast-Film Process*, J. Non-Newtonian Fluid Mech., **138**, 76, 2006.
- [84] Lamberti, G., Titomanlio, G., Brucato, V., *Measurement and Modeling of the Film Casting Process. 1. Width Distribution along Draw Direction*, Chemical Engineering Science, **56**, 5749, 2001.
- [85] Lamberti, G., Titomanlio, G., Brucato, V., *Measurement and Modeling of the Film Casting Process. 1. Temperature Distribution along Draw Direction*, Chemical Engineering Science, **57**, 1993, 2002.
- [86] Smith, S.W., *Simulating the Cast Film Process Using an Updated Lagrangian Finite Element Algorithm*, Thesis, McMaster University, 2001.
- [87] Smith, S., Stolle, D., *Numerical Simulation of Film Casting Using an Updated Lagrangian Finite Element Algorithm*, Polymer Engineering and Science, **43** (5), 1105, 2003.
- [88] Phan-Thien, N., Tanner, R.I., *A New Constitutive Equation Derived From Network Theory*, J. Non-Newtonian Fluid Mech., **2**, 353, 1977.
- [89] Denn, M. M., Petrie, C. J. S., Avenas, P., *AIChEJ*, **21**, 791, 1975.
- [90] Phan-Thien, N., *A Non-linear Network Viscoelastic Model*, J. Rheol., **22**, 259, 1978.
- [91] Coulson, J.M., Richardson, J.F., *Chemical Engineering*, **Vol. 1** (3-rd edition), Pergamon Press, N.Y., 1977.
- [92] Honerkamp, J., Weese, J., *A Nonlinear Regularization Method for the Calculation of Relaxation Spectra*, Rheologica Acta, **32**, 65, 1993.

Acknowledgements

I am deeply indebted to Stef van Eijndhoven, my advisor, for without his patient guidance, rich scientific insight, creativity, and most importantly, his everlasting belief in me, the present work would not have been possible. I would also like to express my sincere gratitude to Prof. Han Meijer and Prof. Rudolf Koopmans, my promoters, for their time, encouragement, fruitful comments and constructive criticism.

I am grateful to Dow Benelux B.V. for providing me with an interesting and challenging project and supporting me throughout my work. In particular, I thank Jerome and Jaap for sharing their knowledge, experience and for their genuine enthusiasm in my work. To Elsa, Lizzy, Jolanda, Katya, Michael, Guido and many others a special "thank you" for making me feel at Dow like at home during the last couple of years. Additional thanks to Marc Mangnus and Marc Dees for their help in performing Rheotens experiments.

I owe much to my family, for it was my mother who always wanted me and my brother to have a degree, who encouraged us for high achievements in whatever we did and supported all our wishes and dreams. This work is devoted as much to her, as to my dear brother, the memory of whom kept my spirits high even at times I was ready to give up.

I cordially thank all my friends for providing help, refuge, or just being there on the other side of the phone line, when I needed them. I appreciate and love all of you.

Last, but not least, I wish to thank my dear husband. His love, friendship, and support mean a great deal to me.

Curriculum Vitae

Olena Zavinska was born on August, 28, 1978 in Chernihiv, Ukraine. In September 1995 she started her studies of Mathematics at the faculty of Mechanics and Mathematics of the Ivan Franko National University in Lviv, Ukraine. In July 2000 she received a Diploma with Honor and was awarded her M.Sc. degree on the master thesis entitled "Spectral Properties of Contrasting Structures". From July 2000 until June 2001 she taught Mathematics at the Lviv Institute of Management; from June 2001 until February 2004 she worked as an engineer in the Information Systems Department of Lvivoblenergo, a power supply company in the Western region of Ukraine.

In 2004, Olena returned to the academic world. After a successful application, she became an Assistant in Technological Design at the post-master program Mathematics for Industry of the Eindhoven University of Technology. In May 2006, she finished the post-master program with a graduation project that formed the basis for the follow up PhD, which was funded by Dow Benelux B.V., Terneuzen. The result of this PhD-project is the underlying thesis.